

# Hot Electron Bolometer Mixers for THz Arrays



Inaugural - Dissertation

zur

Erlangung des Doktorgrades

der Mathematisch-Naturwissenschaftlichen Fakultät

der Universität zu Köln

vorgelegt von

**Denis Fabian Büchel**

aus Köln

Köln, 2017

Gutachter:

Prof. Dr. Jürgen Stutzki  
Prof. Dr. Andreas Zilges

Tag der mündlichen Prüfung: 27.06.2017

---

## Abstract

The focus of this thesis is the development of superconducting Hot Electron Bolometer (HEB) waveguide mixers for heterodyne array (multi-pixel) receivers in the frequency range of 2 to 5 Terahertz (THz). These mixers are developed for the 2 x 7 pixel Low Frequency Array (LFA) channel (1.9 THz) and the single pixel H-channel (4.7 THz) of the German REceiver for Astronomy at Terahertz frequencies (GREAT). GREAT operates on the Stratospheric Observatory for Infrared Astronomy (SOFIA) on board of an airplane and is a very high spectral resolution ( $\sim 10^7$ ) receiver which allows the observations of the interstellar medium by detection of atomic and molecular line transitions in the range of 1.2 - 4.7 THz. For the LFA at 1.9 THz, in total 34 mixers are manufactured and characterized. 14 of them are currently in operation as a part of the upGREAT receiver channels for GREAT. For the H channel, a single mixer and a spare one are developed and characterized.

Previously developed HEB mixers for GREAT, were based on NbTiN as microbridge film material, which resulted in an instantaneous intermediate frequency (IF) noise bandwidth limit of about 2 GHz. The HEB mixer is the component of a heterodyne receiver that limits the instantaneous bandwidth for observations. A minimum bandwidth is required to cover the full Doppler-broadened spectra of e.g. extragalactic sources.

Based on the success of previous studies from other groups, NbN was selected for the new generation of upGREAT mixers. The HEB mixers based on a NbN film, with a volume of 4.0 nm x 400 nm x 3100 nm showed a significantly higher LO power requirement compared to the NbTiN mixers. Due to the limited available LO power at GREAT, new wafers with a reduced HEB volume (3.5 nm x 200 nm x 3050 nm) were processed. The LO power requirement was indeed reduced to an average value of 3 times the power needed for NbTiN mixer. In total 20 of these mixers were fabricated and characterized for the commissioning of LFA and the 14 best performing mixers were delivered to GREAT.

Another wafer was processed which had the same HEB volume as the previous one but with a slightly thinner film NbN. The LO power requirement for HEB mixers made of this film reduced the averaged value to 0.3  $\mu$ W, which is comparable to the NbTiN HEB mixers. A further 14 mixers were fabricated and characterized, which now populate 7 mixers of the LFA. For all wafers, the measured noise temperature of the mixers made of NbN and NbTiN, is surprisingly similar. The average measured mixer noise temperature is  $(430 \pm 20)$  K and the gain is of  $(-5.9 \pm 0.2)$  dB with an averaged IF noise bandwidth of  $(3.9 \pm 0.1)$  GHz for mixers from the last two production wafers. The NbTiN mixer had an averaged measured mixer noise temperature of about  $(500 \pm 50)$  K and a gain of about  $(-10 \pm 1)$  dB with an IF noise bandwidth of  $(2.1 \pm 0.2)$  GHz. The measured results show that the

---

NbN HEB mixers are generally superior to NbTiN HEB because the bandwidth is higher and noise temperature is lower.

A heterodyne characterization setup has been developed to enable repeatable and well-calibrated measurements of the mixer sensitivity and bandwidth. The IF output chain was optimized to cover the noise bandwidth of the mixer between 0.5 - 5 GHz. Furthermore, the fabrication and assembly of mixer blocks and horn clamps went through a rigorous specification and verification procedure that was set-up together with the in-house mechanical workshop and the group's technician.

An empirical investigation of the extended collected data set is performed for the 1.9 THz measurements. The required local oscillator power ( $P_{LO}$ ) depends in first order linearly on the critical current ( $I_c$ ) for devices of the same wafer. The slope of  $P_{LO}$  ( $I_c$ ) is wafer dependent. The heat balance equation of the lumped element model is used to calculate theoretically the  $P_{LO}$  as a function of  $I_c$ . This simple theoretical model does not provide sufficient accuracy for calculation of the  $P_{LO}$ . Furthermore, the noise temperature is about a factor of 5 higher than the theoretical value and the mixer gain is about 1 to 3 dB higher.

The single mixer for the GREAT 4.7 THz channel is based on the thicker NbN film of the early wafers because sufficient LO power is available for this single mixer from a Quantum Cascade Laser (QCL) LO. The measured receiver noise temperature in GREAT at an IF of 0.5 GHz is about 900 K. This receiver sensitivity is comparable to the measured receiver noise temperature of the 1.9 THz mixers for LFA of 800 K. Both receiver channels have a state of the art performance. Based on the experience with the new mixers we can conclude that the reduction of the LO power consumption of a NbN HEB mixer by a factor of 10 by adapting the film parameters and the bolometer dimensions does not change the sensitivity. Both receiver channels of GREAT, the H-channel and the LFA are successfully commissioned in 2014 and 2015 and provided a wealth of astronomical data.

---

## Zusammenfassung

Der Schwerpunkt dieser Arbeit liegt in der Entwicklung von supraleitenden Hot Electron Bolometern (HEB), welche als Waveguide-Mischer für Heterodyne-Array (Multi-Pixel) Empfänger im Frequenzbereich von 2 bis 5 Terahertz (THz) eingesetzt werden. Diese Mischer werden für den 2 x 7 Pixel Low Frequency Array (LFA) Kanal (1,9 THz) und den Singlepixel H-Kanal (4,7 THz) des German REceiver for Astronomy at Terahertz frequencies (GREAT) entwickelt. GREAT ist am Stratospheric Observatory for Infrared Astronomy (SOFIA) an Bord eines Flugzeugs im Einsatz. GREAT hat eine sehr hohe spektrale Auflösung ( $\sim 10^7$ ), die es ermöglicht, Beobachtungen des interstellaren Mediums durchzuführen und Linienemission atomarer und molekularer Übergänge im Bereich von 1,2 - 4,7 THz zu vermessen.

Für den LFA Kanal bei 1,9 THz wurden insgesamt 34 Mischer hergestellt und charakterisiert, davon sind 14 derzeit in Betrieb. Für den H-Kanal wurde ein Flug-Mischer und ein Backup-Mischer entwickelt und charakterisiert.

Die bisher entwickelten HEB-Mischer für GREAT basierten auf NbTiN als Filmmaterial für die Micro-Brücken, was zu einer Zwischenfrequenz (ZF) Rauschbandbreite von etwa 2 GHz führte. Der HEB Mischer ist die Komponente eines heterodyne Empfängers, welche die instantane Bandbreite für die Beobachtungen limitiert. Ein Minimum der Bandbreite wird benötigt um die vollen Doppler-verbreiterten Spektren von z.B. extragalaktischen Quellen beobachten zu können.

Basierend auf früheren erfolgreichen Studien von anderen Gruppen wurde NbN ausgewählt um die upGREAT Mischer mit neuen Mixern auszustatten.

Allerdings benötigen die HEB-Mischer auf Basis eines NbN-Films mit einem Volumen von 4,0 nm x 400 nm x 3100 nm im Vergleich zu den NbTiN-Mixern eine deutlich höhere LO-Leistung. Aufgrund der begrenzten LO-Leistung bei GREAT wurden daher neue Wafer mit einem reduzierten HEB-Volumen (3,5 nm x 200 nm x 3050 nm) hergestellt. Der Bedarf an LO-Leistung konnte dadurch um einen Faktor 3 im Vergleich zu dem NbTiN-Mischer benötigten Leistung reduziert werden. Insgesamt wurden 20 dieser Mischer hergestellt und für die Inbetriebnahme von LFA charakterisiert. Die 14 leistungsstärksten Mischer wurden an GREAT geliefert.

Ein weiterer Wafer wurde hergestellt, welcher das gleiche HEB-Volumen wie die vorherige hatte, aber mit einem etwas dünneren NbN Film. Der LO-Leistungsbedarf für HEB-Mischer aus diesem Film ist auf durchschnittlich 0,3  $\mu$ W reduziert worden, ähnlich dem der bisherigen NbTiN HEB-Mischer. Es wurden weitere 14 Mischer hergestellt und charakterisiert, von denen nun 7 Mischer im LFA verwendet werden.

Für alle gemessenen NbTiN und NbN Mischer sind die Empfindlichkeiten, basierend auf

---

den gemessenen Rauschtemperatur, überraschend ähnlich. Die durchschnittliche gemessene Mischer-Rauschtemperatur beträgt  $(430 \pm 20)$  K und die Verstärkung  $(-5.9 \pm 0.2)$  dB mit einer gemittelten IF-Rauschbandbreite von  $(3.9 \pm 0.1)$  GHz für Mischer der beiden letzten Produktions-Wafern. Der NbTiN-Mischer hat eine gemittelte gemessene Mischer-Rauschtemperatur von etwa  $(500 \pm 50)$  K und eine Verstärkung von etwa  $(-10 \pm 1)$  dB mit einer IF-Rauschbandbreite von  $(2.1 \pm 0.2)$  GHz. Die gemessenen Ergebnisse zeigen, dass die NbN-HEBs im Vergleich zu den NbTiN HEB Mischer bevorzugt wurden, da die Bandbreite größer und die Rauschtemperatur niedriger ist.

Außerdem wurde ein Heterodyne-Charakterisierungs-Setup entwickelt, um wiederholbare und gut kalibrierte Messungen der Mischer Empfindlichkeit und Bandbreite zu ermöglichen. Die ZF-Ausgangskette wurde optimiert, um die Rauschbandbreite des Mixers zwischen 0,5 - 5 GHz abzudecken. Darüber hinaus führte die Fertigung und Montage von Mischerblöcken und Hornklemmen durch ein genaues Spezifikations- und Verifizierungsverfahren, das zusammen mit der hauseigenen mechanischen Werkstatt und dem Techniker der Gruppe entwickelt wurde.

Für die 1,9 THz-Messungen wurde eine empirische Untersuchung der erweiterten gesammelten Datensatzes durchgeführt. Die erforderliche Leistung des lokale Oszillatorleistung ( $P_{LO}$ ) hängt in der ersten Ordnung linear von dem kritischen Strom ( $I_c$ ) des Mixers vom gleichen Wafers ab. Die Steigung von  $P_{LO}$  ( $I_c$ ) ist vom Wafer abhängig. Die Wärmebilanzgleichung des Lumped Element Modell wurde verwendet, um die theoretisch  $P_{LO}$  als Funktion von  $I_c$  zu berechnen. Dieses einfache theoretische Modell liefert keine ausreichende Genauigkeit für die Berechnung des  $P_{LO}$ . Die Rauschtemperatur ist um einen Faktor 5 höher als der theoretische Wert und die Mischer Verstärkung ist um etwa 1 bis 3 dB erhöht.

Der Mischer für den GREAT 4.7 THz Kanal basiert auf dem dickeren NbN-Film der frühen Wafer, da für diesen Mischer von einem Quantenkaskadenlaser (QCL) LO genügend Leistung zur Verfügung steht. Die gemessene Empfängerrauschtemperatur in GREAT bei einem ZF von 0,5 GHz beträgt etwa 900 K. Diese Empfangsempfindlichkeit ist vergleichbar mit der gemessenen Empfängersrauschentemperatur der 1,9 THz Mischer für LFA von 800 K. Beide Empfängerkanäle sind auf dem aktuellsten Stand der Technik.

Basierend auf den Erfahrung mit den neuen Mixern, können wir feststellen, dass die Verringerung des LO-Leistungsverbrauchs eines NbN HEB-Mixers um den Faktor 10 durch Anpassung der Filmparameter und der Bolometer Abmessungen, die Empfindlichkeit nicht verändert. Beide Empfängerkanäle von GREAT, H-Kanal und LFA, wurden in den Jahren 2014 und 2015 erfolgreich in Betrieb genommen und lieferten eine Fülle astronomischer Daten.

# Contents

<b>1</b>	<b>Introduction</b>	<b>2</b>
1.1	Astronomical Observations at Terahertz Frequencies . . . . .	2
1.2	Observation Platforms . . . . .	3
1.3	Detection of Terahertz Signals . . . . .	5
1.4	German REceiver for Astronomy at Terahertz Frequencies . . . . .	7
<b>2</b>	<b>Superconducting Hot Electron Bolometer as Mixers</b>	<b>10</b>
2.1	Bolometers . . . . .	10
2.2	Hot Electron Bolometers . . . . .	11
2.3	Superconducting Hot Electron Bolometer Mixer . . . . .	12
2.3.1	Diffusion-cooled HEB Mixer . . . . .	13
2.3.2	Phonon-cooled HEB Mixer . . . . .	14
2.3.3	Critical Temperature and Current of a Superconducting HEB . . . . .	15
2.3.4	The Standard Model . . . . .	17
2.3.5	Broken-Line Transition Model . . . . .	18
2.3.6	Hot-Spot Model . . . . .	22
2.4	Detection Principle . . . . .	24
2.4.1	Direct Detection . . . . .	25
2.5	Receiver Sensitivity . . . . .	27
<b>3</b>	<b>Mixer Design and Fabrication</b>	<b>30</b>
3.1	Mixer Design . . . . .	30
3.1.1	1.9 THz Circuit Design . . . . .	31
3.1.2	IF Impedance Mismatch . . . . .	32
3.1.3	4.7 THz Circuit Design . . . . .	34
3.2	Fabrication and Assembly . . . . .	36
3.2.1	Devices . . . . .	36
3.2.2	Mixer Blocks . . . . .	38
3.2.3	Horn-Clamp . . . . .	41
3.2.4	Mixer Assembly . . . . .	42
<b>4</b>	<b>Heterodyne Measurement Setup at 1.9 to 4.7 THz</b>	<b>44</b>
4.1	Radio Frequency Setup for the Operation at 1.9 THz . . . . .	45
4.2	IF Setup at 0.2 to 5 GHz for the 1.9 THz Measurements . . . . .	47
4.2.1	Intermediate Frequency-Box . . . . .	47

## CONTENTS

---

4.2.2	The Mixing Path . . . . .	49
4.3	4.7 THz Single Pixel Receiver . . . . .	50
4.4	Differences to the GREAT Receiver Channels . . . . .	50
<b>5</b>	<b>Measurement Methods for HEB Mixer Characterization</b>	<b>52</b>
5.1	DC Characterization . . . . .	52
5.2	Broadband RF Characterization . . . . .	53
5.3	Local Oscillator Power Requirement . . . . .	53
5.4	Heterodyne Measurements Methods . . . . .	57
5.4.1	Voltage Sweep . . . . .	57
5.4.2	Local Oscillator Power Sweep . . . . .	57
5.4.3	Spectral Intermediate Frequency Response . . . . .	58
<b>6</b>	<b>Characterization of the HEB Mixers</b>	<b>60</b>
6.1	HEB Mixers Based NbN . . . . .	60
6.1.1	DC Properties . . . . .	61
6.1.2	Analysis of the Resistance Change . . . . .	67
6.1.3	THz Broadband Response of the Mixers . . . . .	69
6.1.4	Heterodyne Response . . . . .	71
6.1.5	Local Oscillator Power Sweep . . . . .	72
6.1.6	Voltage Sweep . . . . .	73
6.1.7	Mixer Gain and Noise Temperature . . . . .	76
6.1.8	Spectrometer Measurements . . . . .	81
6.1.9	Noise Bandwidth . . . . .	82
6.1.10	HEB Mixer Gain Bandwidth . . . . .	85
6.1.11	Local Oscillator Power Requirement . . . . .	89
6.2	Silicon Inlay Waveguides . . . . .	91
6.3	A 1.9 THz NbTiN HEB Mixer . . . . .	93
6.4	4.7 THz GREAT H-Channel Mixer . . . . .	96
6.4.1	DC Properties . . . . .	96
6.4.2	FTS Response . . . . .	98
6.4.3	Mixer Sensitivity . . . . .	99
6.4.4	IF Noise Bandwidth . . . . .	101
6.4.5	4.7 THz Mixers Conclusions . . . . .	101
6.5	HEB as a Characterization Tool for Local Oscillators . . . . .	102
6.5.1	Characterization of the QCL . . . . .	103

---

<b>7</b>	<b>Discussion of the 1.9 THz Measurement Results</b>	<b>106</b>
7.1	HEB Mixers Based on NbN . . . . .	106
7.1.1	DC Characterization of NbN HEB Mixers . . . . .	106
7.1.2	THz Response . . . . .	108
7.1.3	Estimate of the Optimum Local Oscillator Pump Power . . . . .	108
7.1.4	Mixer Sensitivity . . . . .	120
7.1.5	IF Noise and Gain Bandwidth . . . . .	123
7.1.6	Silicon Inlay Technology . . . . .	124
7.2	Comparison of NbN and NbTiN Based HEB Mixers . . . . .	124
<b>8</b>	<b>Summary and Outlook</b>	<b>128</b>
	<b>Bibliography</b>	<b>132</b>
	<b>Danksagung</b>	<b>144</b>
	<b>Finacial support</b>	<b>146</b>
	<b>Publicationen</b>	<b>148</b>
	<b>Eidesamtlich Erklärung</b>	<b>150</b>
	<b>Lebenslauf</b>	<b>152</b>



# 1 Introduction

## 1.1 Astronomical Observations at Terahertz Frequencies

In astronomy, the formation of stars is so far not fully understood. The formation starts with interstellar medium and the formation of molecular clouds.

The THz range describes the frequency range between  $\sim 0.3 - 20$  THz which is also known as the far-infrared region between the wavelengths of about  $15 \mu\text{m}$  to  $1 \text{mm}$ . In this part of the electromagnetic spectrum, many important transitions of atoms, ions, molecules (by rotation and vibration spectroscopy) can be observed. The measured transitions can be used to describe a model of the physical properties of interstellar clouds which are the region of the formation of stars.

The universe consists of the two most abundant elements hydrogen (H) and helium (He). They represent 75% and 24% of the total mass fraction. He is a noble gas and due to the fact that it has no valence electrons, it is the most non-reactive element. It can be excited by ionization at high temperatures or by UV radiation. In interstellar clouds, the hydrogen is mainly found as the molecule  $\text{H}_2$ . At temperatures above 50 K, the  $\text{H}_2$  molecule can be excited and observed via rotation transitions at 10.6 THz ( $28 \mu\text{m}$ ) and 17.6 THz ( $17 \mu\text{m}$ ). At these frequencies, high-resolution spectroscopy receivers are not being developed so far. Below 50 K,  $\text{H}_2$  is predominated at the ground state because it is shielded from the high-energy radiation and can only be excited by collisions. Other elements or molecules must be used to trace the  $\text{H}_2$  gas in this cold environment. The next most common elements are oxygen (O) with 1% and carbon (C) with 0.5 % of the total mass fraction. A complex chemical network of C and O based molecules can be found in the interstellar clouds. The very stable and therefore highly abundant molecule CO ( $10^{-4}$  less frequently than  $\text{H}_2$ ) is often used to probe the  $\text{H}_2$  gas. The lowest transition frequency to the ground state at about 115 GHz can be observed at a temperature of the gas of about 10 K. CO has a rotational spectrum with transition about every 115 GHz which makes it possible to observe CO over a large frequency range. It is used as tracers for the  $\text{H}_2$  gas in the inner parts of interstellar clouds. Because the dissociation energy of CO (11.11 eV) is similar to the C ionization energy (11.26 eV) the C is often ionized when the CO is dissociated. The singular ionized carbon ( $\text{C}^+$ ) has a fine-structure transition line ( $J=3/2 - 1/2$ ) at 1.9005 THz ( $158 \mu\text{m}$ ) which is one of the strongest cooling lines in the interstellar medium (ISM) as long as most of the carbon exists as  $\text{C}^+$  [1]. This is true for photo-dissociation regions (PDR) at the outer regions of molecular clouds [1]. The fine-structure line ( $^3P_1 - ^3P_2$ ) of atomic oxygen (O) at 4.7448 THz ( $63 \mu\text{m}$ ) is also a main coolant of the PDRs [2]. Observations showed that

the cooling lines are important in external galaxies [3] and a tracer of star-formation rates in high red-shift galaxies [4].

In this thesis, I concentrate on the two transition lines at 1.9 THz and 4.7 THz. The detection devices thus have been developed operate at these frequencies (see Sec. 1.4). The observation platforms in the THz range between 1 - 5 THz are discussed in the next section.

## 1.2 Observation Platforms

Atmospheric transmission properties are a major issue for observations through the earth's atmosphere, especially at THz frequencies. Fig. 1 shows the calculated transmission of the earth's atmosphere between 1 - 5 THz for three different observation sites mainly based on water vapor and Ozon absorptions: The Cologne atmosphere at an altitude of 0 km, the NANTEN telescope site at an altitude of 4.8 km and Stratospheric Observatory for Far Infrared Astronomy (SOFIA) on board of an airplane, at an altitude of 13 km (observations between 12 - 14 km) [5]. An additional zoom at frequencies of 1.9 THz and 4.7 THz is shown in Fig. 2. The atmospheric transmission models show that it is impossible to observe the target lines from ground based telescopes. Observations of both transmission lines must be carried out from high altitudes, such as airplane-, balloon- or satellite-based telescopes which allow observations from the stratosphere or even outside the earth's atmosphere.

In the past, observations were made with the Kuiper Airborne Observatory (KAO) [6], the Herschel satellite [7], Infrared Space Observatory (ISO) [8] and Stratospheric Terahertz Observatory2 (STO2, a successor of STO [9]) balloon in the THz range. Currently, the Stratospheric Observatory for Infrared Astronomy (SOFIA) is the only platform which is in frequent operation. SOFIA is a 747 SP airplane with an integrated 2.7 m diameter main dish telescope. The development and operation are carried out in a cooperation between the National Aeronautics and Space Administration (NASA) and the Deutsche Zentrum für Luft- und Raumfahrt (DLR) (funded 80 % by NASA and 20% by DLR). It has been operating since 2010 with different instruments that are regularly exchanged. The observations start either from the northern hemisphere in Palmdale (California, USA) or from the southern hemisphere in Christchurch (New Zealand). A future project is the Chinese Dome A with the DATE5 telescope planned in the Antarctica at an altitude of 4.093 km [10]. Due to the atmospheric conditions, observations might be possible up to 2 THz. CCAT-Prime will be a 6 m telescope at an altitude of 5.6 km next to the Cerro Chajnantor mountain operating at a frequency range between 0.85 - 1.5 THz. It is carried out in a cooperation between the Cornell University, Universität zu Köln and other partners. In addition, another balloon based mission called GUSTO, a successor of STO and STO2, is proposed.

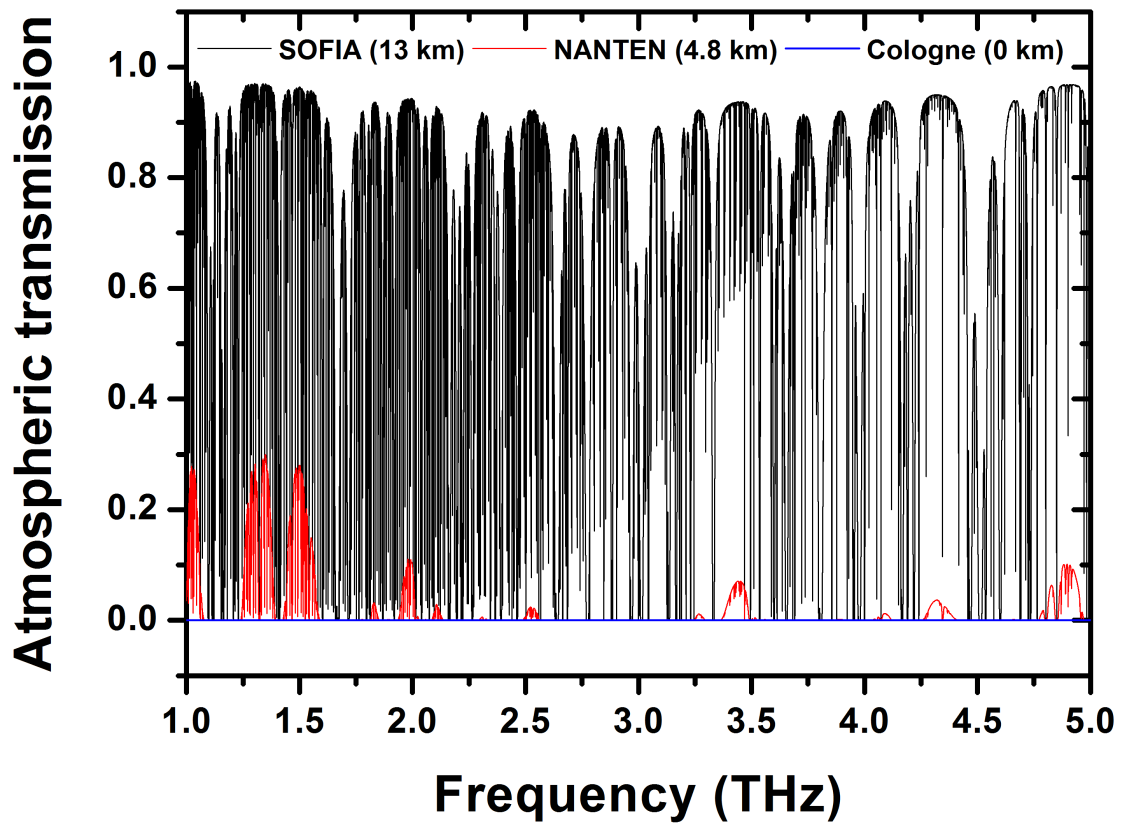


**Figure 1:** Calculated atmospheric transmission between 1 - 5 THz for three observation side: NANTEN (red), SOFIA (black) and Cologne (blue). [5]

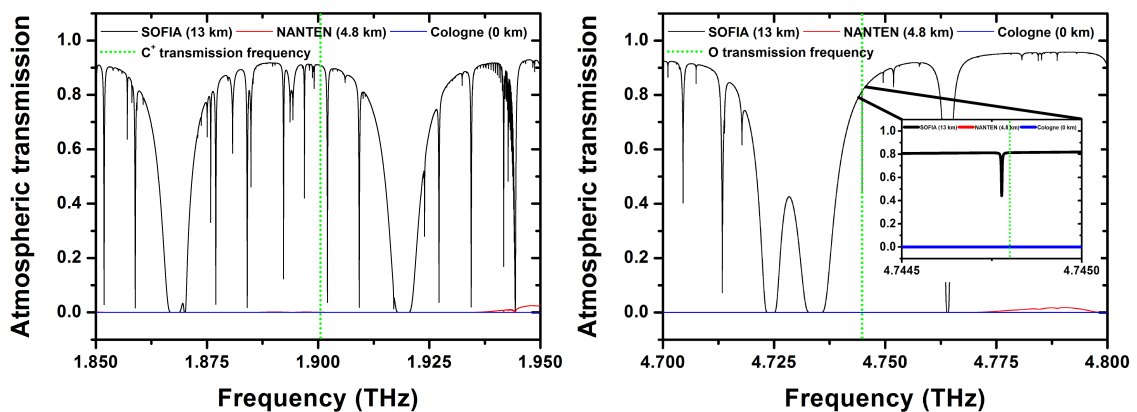


**Figure 2:** Calculated atmospheric transmission at 1.9 and 4.7 THz for three observation sites: NANTEN (red), SOFIA (black) and Cologne (blue) [5]. Green dotted line lines indicate the two transition frequencies at 1.9 and 4.7 THz

### 1.3 Detection of Terahertz Signals

The principles of the signal detection and the preferred method for spectral line observations are discussed in this section. The two fundamental methods for the detection of photons are the incoherent (direct) detection and the coherent (heterodyne) detection. Direct detectors generate a response (e.g. DC voltage, resonator frequency shift) which is proportional to the amount of coupled radiated power without preserving the phase and frequency information of the photons. Kinetic inductance detectors (KIDs) and transition edge sensors (TES) are two examples used as superconducting direct detectors in the THz range. In the case of a heterodyne measurement, the THz radiation is "mixed" with a stronger reference radiation (the local oscillator) and converted downwards to the GHz range. The local oscillator is preferably phase and frequency locked for stable operation. This converted frequency is called intermediate frequency (IF). The IF can be amplified with low noise amplifiers (LNA) and analyzed with a spectrometer. The amplitude and the phase information of the THz radiation are preserved. The devices used for the down conversion process are called mixers. The most commonly used THz mixers are Schottky-barrier diodes, Superconductor Isolator Superconductor (SIS) tunnel junctions and superconducting Hot Electron Bolometers (HEB).

Schottky diodes and SIS junctions have highly nonlinear I-V characteristics that work like a switch caused by a multiplication of the local oscillator and the THz signal which generates an intermediate frequency output. SIS and superconducting HEB mixers (see Sec. 2) are currently the devices with the highest mixer sensitivity ranging from the GHz to the THz frequency range. The maximum frequency at which SIS mixers can be used is determined by the sum of the frequencies of the superconducting gaps of the SIS junction electrode materials. Presently, this frequency is about 1.4 THz, which is two times the gap frequency of niobium ( $2\Delta/h \sim 700$  GHz). HEB mixers have a low-frequency limit set by the superconducting gap frequency of the material which depends on the critical temperature of the superconducting film. To produce the hot electrons, Cooper pairs need to be broken by the local oscillator radiation. The mechanism of the detection of HEB mixers has not been fully understood so far [11]. At the high-frequency end, HEB mixers are limited by the elastic scattering time in the HEB film of about  $10^{-15}$ s sets an upper limit for the HEB mixers at about 100 THz [12]. The fundamental limit of sensitivity of double sideband heterodyne detectors is the quantum limit expressed as the equivalent quantum noise temperature  $hf/2k_B$  ( $h$  Planck constant,  $f$  frequency,  $k_B$  Boltzmann constant) [13], [14], [15]. In contrast, direct detectors do not have a fundamental limit of sensitivity. In experiments, both direct and heterodyne detectors always produce noise which has to be

minimized. In addition, the sensitivity is reduced by input filters and the thermal fluctuation noise of background radiation.

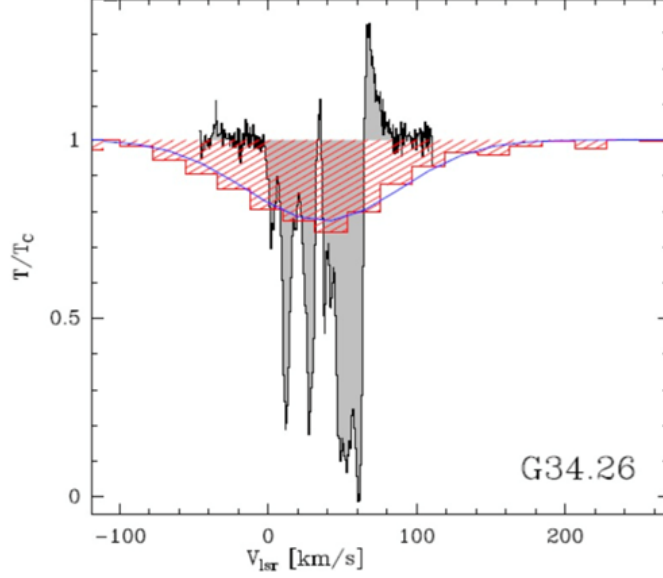


**Figure 3:** Comparison of a a GREAT spectrum with a PACS spectrum of observation of the oxygen line of a the astronomical source G34.26 [16]. W31C is located in the Sagittarius arm in a distance of 1.56 kpc away from the sun. The gray plot representing the heterodyne observation with GREAT and in red a histogram from the direct detection of PACS. The transition line is observed in absorption against a strong background source.

For a comparison of both types of detection methods with respect to sensitivity and frequency resolution at 4.7 THz two state of the art instruments, PACS (on the Herschel satellite) [17] and GREAT [18] (see Sec. 1.4), were used. The noise equivalent power (NEP) is a measure of the signal to noise ratio of a direct detector system. The NEP of PACS is about  $8.9 \times 10^{-18} \text{ W}/\sqrt{\text{Hz}}$ . To compare this value with the sensitivity of the GREAT H-channel ( $T_{rec} \sim 800 \text{ K}$ )  $T_{rec}$  is multiplied by the Boltzmann constant and by the square root of the detection bandwidth (4 GHz) resulting in a NEP of  $7 \times 10^{-16} \text{ W}/\sqrt{\text{Hz}}$ . The spectral frequency resolution of an instrument is defined as  $\Delta f/f$  where  $f$  is the target frequency and  $\Delta f$  the smallest difference frequency that can be distinguished ( $\Delta v = \Delta f \frac{c}{v_0}$  in km/s). A comparison of an observation using a PACS and GREAT on the same target source is shown in Fig. 3. The frequency resolution for these observations of PACS is about 25 km/s (or  $1/10^4$ ) (see Fig. 3) whereas the resolution of the GREAT H-channel is approximately 0.5 km/s (or  $1/(10^6)$ ). In the publication from Wiesemeyer et al. comparison of observations of astronomical source G34.26 from the O line at 4.7 THz with both PACS and GREAT is shown in Fig. 3 [16].

The GREAT spectrum resolves a complex structure with several different components which are not resolved with PACS. For this reason, heterodyne detection is used in the THz

range instead of the direct detection to study the composition of the multiple different red and blue shifted line components with respect to the averaged Doppler shifted transition line of the source. The line components are different parts of the clouds which move with different relative speeds.

## 1.4 German REceiver for Astronomy at Terahertz Frequencies

The instrument we have build for SOFIA is the German REceiver for Astronomy at Terahertz Frequencies (GREAT). GREAT is a heterodyne instrument which operates two receiver channels simultaneously with a diachronic filter to separate the input frequencies. It offers a spectral resolution up to  $R \sim 10^8$  at frequency windows from 1.4 - 4.7 THz. Each frequency channel consists of an individual dewar with a single mixer or an array of 7 or 14 mixers. The receiver channels were developed in collaboration with the Max Planck Insitut für Radioastronomy (MPIfR) in Bonn and the Deutsche Zentrum für Luft und Raumfahrt (DLR) in Berlin [18] [19] [20]. All mixers were developed in Cologne [21] [22] [23]. All receiver channels available so far are listed in Tab. 1.

receiver channel	frequency (THz)	pixel number
L1	1.25 - 1.52	1
L2	1.81 - 1.91	1
M	2.4 - 2.7	1
H	4.7	1
LFA	1.83 - 2.54	2x7
HFA	4.7	1x7

**Table 1:** A comparison of current GREAT receiver channels.

The single mixer receiver channels operate at band L1 (1.25 - 1.52 THz), band L2 (1.81 - 1.91 THz), band M (2.4 - 2.7 THz) and band H (4.7448 THz) [18]. In addition, the upGREAT receiver provides two additional channels: the Low Frequency Array (LFA) consisting of two times seven mixers for detection of both polarizations simultaneously at 1.83 - 2.52 THz and the High Frequency Array (HFA) operating seven pixels at 4.7448 THz [24], [19]. For the operation of the mixers, the single mixer channels and arrays were both cooled down to a temperature of about 4.2 K using a liquid helium cryostat and closed-cycled pulse tube refrigerators.

The LFA mixers were placed in a hexagonal configuration around a central pixel. A detailed description of the GREAT instrument and the LFA receiver channel can be found

in Heyminck et al. [18] and Risacher et al. [19]. An essential part of this thesis was the development of reliable test setup, measurement and integration of all mixers for the LFA and H channel, before the integration of the instrument. The mixers were installed at the MPIfR in Bonn for the LFA and H channel (see Fig. 4 and Fig. 5).

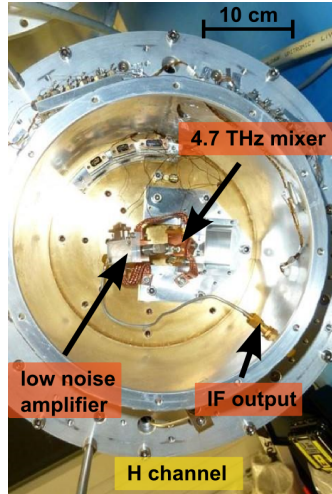


**Figure 4:** The installation of H-channel mixer in a GREAT dewar at the Max Planck institute for Radioastronomy in Bonn.

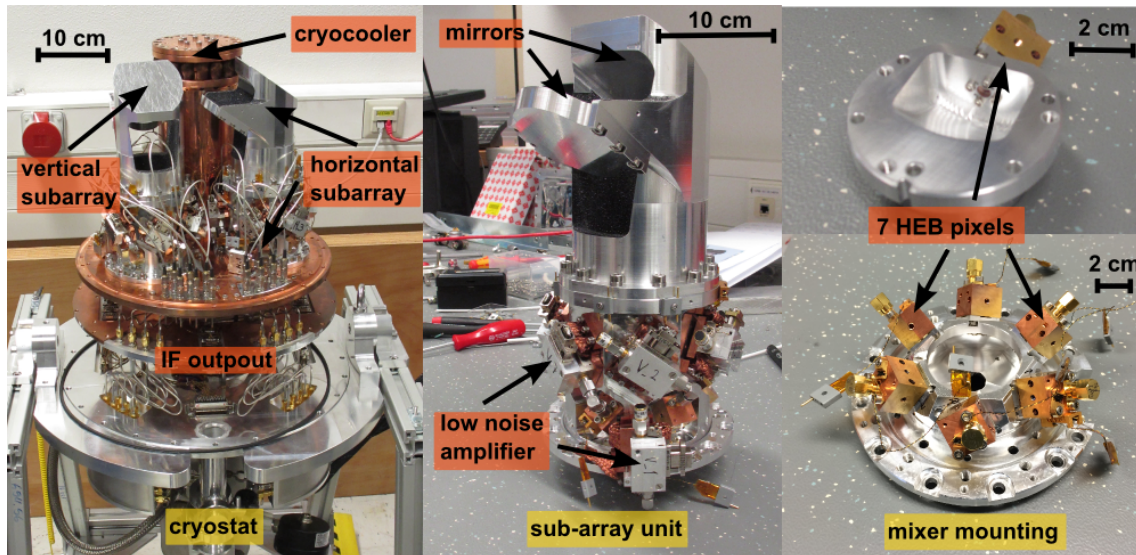


**Figure 5:** Installation of the mixers into the LFA dewar at the Max Planck institute for Radioastronomy in Bonn. Left: Inner part of the LFA cryostat. Center: A sub-array removed from the LFA cryostat. Right: The mounting of LFA mixer.

Overall, the performance of 34 mixers for the LFA, 3 mixers for the H channel and 3 mixers for the NbTiN based HEB were measured. 2/3 of the measured mixers fulfill the requirements for the operation at the telescope. Finally, I had the chance to be part of the

commissioning team for the LFA (in Palmdale, USA, CA) on board of the SOFIA airplane (see Fig. 6).



**Figure 6:** SOFIA airplane at Armstrong Flight Research Center in Palmdale (California, USA).

## 2 Superconducting Hot Electron Bolometer as Mixers

In this section the physical background of superconducting hot electron bolometer mixers (HEBs) which were used as detectors are described. As a basis to understand this type of device the concept of a bolometer and a hot electron bolometer will be discussed first. Followed by an introduction to superconducting HEB mixers. Furthermore the concept of the signal detection and the definition of the sensitivity of a receiver system will be discussed.

### 2.1 Bolometers

Bolometers are thermal detectors that absorb photons which in turn leads to a temperature change of the device [25]. This change can be read out in several ways. In the case of thermometer connecting to the bolometer the change electrical resistance with temperature can be read out. The temperature change of the bolometer is the same at different frequencies as long the total energy of the photons is identical. A schematic model of a bolometer is shown in Fig. 7.

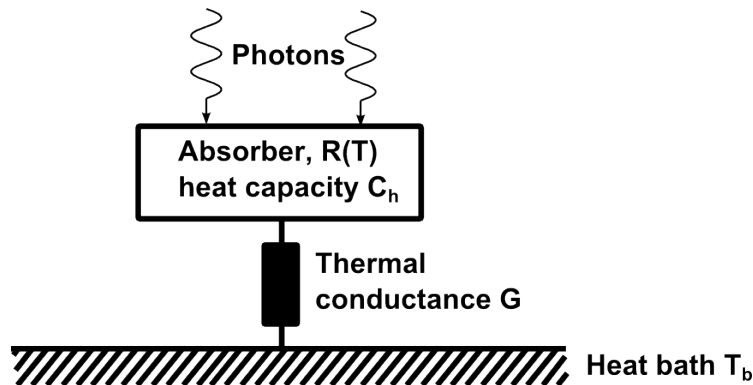


**Figure 7:** Schematic of the photons absorption by a bolometer which is connected to a heat bath via a heat sink.

The incoming photons are absorbed by the electrons which in turn increases the electron temperature. If the exchange of energy between the electrons and the phonons is fast enough, the phonons will heat up as well. The energy flow from the bolometer is given by the thermal conductance  $G$  to a heat sink at a bath temperature ( $T_b$ ). The sensitivity of the bolometer depends on the gradient of the resistance with temperature ( $dR/dT$ ). A strong temperature dependence on the resistance is given by semiconductors and especially by superconducting devices at the transition at their superconducting temperature.

A small change of the resistance leads to a voltage across the thermometer. The voltage response  $S$  of the thermometer measured as volts per watt of the absorbed signal power. The

bolometer is biased with a constant current ( $I$ ). The voltage responsivity of the bolometer is given by [25]:

$$S = \frac{I(dR/dT)}{G - I^2(dR/dT) + iwC_h}, \quad (1)$$

where  $C_h$  is the heat capacity and  $w$  is the angular frequency of the amplitude modulation. The thermal time constant  $\tau_\Theta$  is the time the bolometer required to react to a change in the input signal and is given by:

$$\tau_\Theta = \frac{C_h}{G - I^2(dR/dT)}. \quad (2)$$

$\tau_\Theta$  determines the maximum frequency corresponding to the receiver modulated power. This frequency bandwidth ( $f_{IF}$ ) is given by:

$$f_{IF} = (2\pi\tau_\Theta)^{-1}. \quad (3)$$

Bolometers with long time constants are mainly used as direct detectors. For heterodyne measurements a short time constant is required to measure a larger frequency band. For a short  $\tau_\Theta$  the conductance between the electron and phonon system has to be reduced. These systems can be distinguished by two temperature subsystems discussed in the next sections.

## 2.2 Hot Electron Bolometers

In a thin metal film on a substrate, the electron and phonons are assumed to be separated into two thermal subsystems (see Fig. 8).

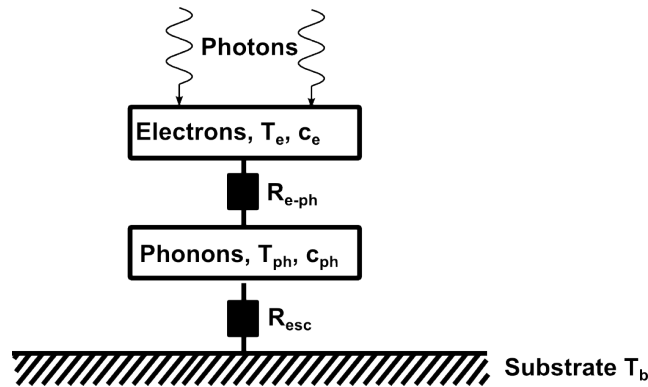


**Figure 8:** Subsystems of a thin metal film hot electron bolometer on a substrate. The separated subsystems are the electrons and phonons.

Both subsystems have different temperature  $T_e$  and  $T_{ph}$ . The interaction between those systems occurs via electron-phonon (eph) scattering ( $R_{eph}$  in the thermal model). In equilib-

rium  $T_e$ ,  $T_{ph}$  and the substrate temperature  $T_b$  are the same. By introducing radiation or DC current to the bolometer  $T_e$  is increased followed by an elevated  $T_{ph}$ . At room temperature the thermal resistance between the electrons and the phonons is negligible, which means a similar temperature for both subsystems. At cryogenic temperatures of a few degrees of Kelvin, the phonon density decreases rapidly, resulting in a longer interaction time between electrons and phonons. Under this condition, the temperature  $T_e$  of the "hot electrons" is significantly increased compared to  $T_{ph}$ . The bottleneck of the heat transfer is the weak electron-phonon interaction.

The effect of hot electrons does not only occur in thin metal films. In semi-conducting film this effect can be even more dominant. The reason for this is generally the smaller electron density compared to metals.

The first hot electron bolometer for heterodyne measurements was developed on the base of the semiconductor InSb [26]. In the experiment, the bolometer was cooled to the temperature of liquid helium (4.2 K) and used as a hot electron bolometer (HEB) mixer for observation in heterodyne receiver by Philips et al. [27]. The measured time constant of InSb was about 100 ps corresponding to an IF bandwidth of 1 MHz. A typical bandwidth of a several GHz is desired for observation in the THz range. To fulfill this requirement a bolometers with an even shorter time constant is required.

### 2.3 Superconducting Hot Electron Bolometer Mixer

A superconducting Hot Electron Bolometer (HEB) mixer consists of a thin superconducting film, also called bridge, which is in contact with two normal metal contacts on a substrate. The film thickness is just several nm (to reduce to thermal time constant), the length is a few hundreds of nm and the width a few  $\mu\text{m}$ . Fig. 9 shows one of our HEB devices. The picture was taken with a scanning electron microscope (SEM).

The HEB is embedded into a high frequency circuit. The incident radiation couples via an antenna to the HEB bridge. The circuit is designed to achieve maximum coupling to the HEB. The radiation is absorbed by the electrons (quasi particles) and Cooper-pairs in the superconductor. The hot electrons cause a variation of the resistance in the film. By introducing a constant DC bias voltage across the HEB a change in resistance causes a power output variation at the IF output of the mixer. It is important to have a sensitive and fast HEB to have a high signal to noise ratio and a large IF band for observations. The thermal time constant of a HEB is in the order of tens of ps, which results in an IF bandwidth of several GHz. The IF noise bandwidth of a HEB defined by the width where the noise temperature increased by a factor of 2 from the minimum value at 0 GHz (see Fig. 10). The time until

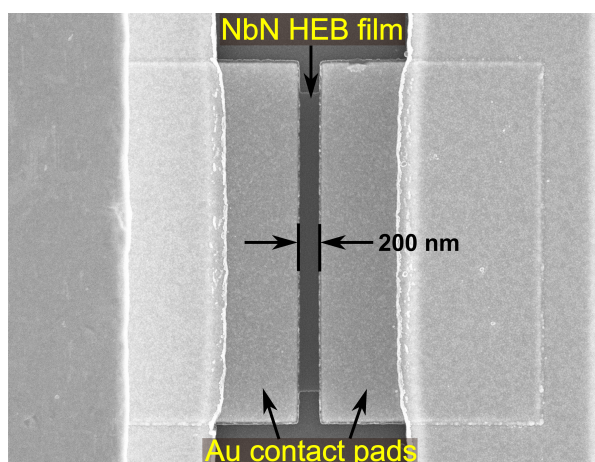


**Figure 9:** Scanning electron microscope (SEM) picture of a NbN HEB. [28]

the energy from the hot electrons is released to the substrate, defines the HEB mixer IF bandwidth.

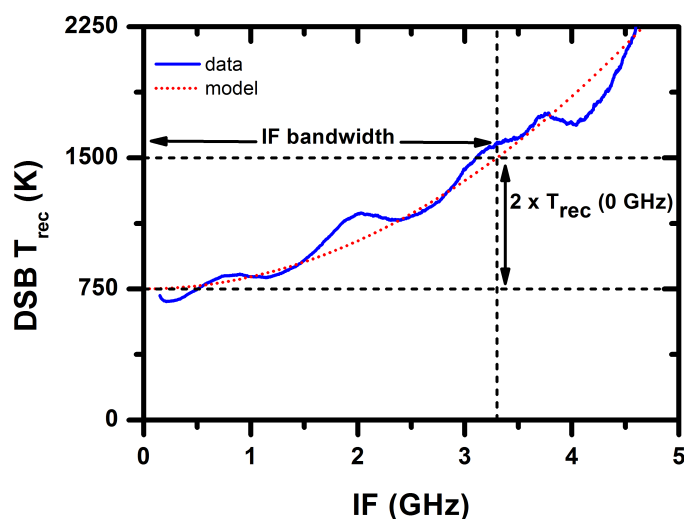


**Figure 10:** Schematic determination of the IF noise bandwidth.

### 2.3.1 Diffusion-cooled HEB Mixer

There are two types of cooling mechanism for HEB mixers depending on either the diffusion [12] or the phonon-cooling path [29] for the to relaxation the heat. The dominating cooling path depends on the choice of the superconductor, the substrate and the geometry of the bridge. The diffusion constant of the HEB bridge and the electron-phonon relaxation time determine the cooling path of the HEB. A HEB mixer is dominated by the diffusion cooling process if the length of the bridge is shorter than the thermal diffusion length  $L_{th}$  defined by:

$$L_{th} = \sqrt{D\tau_{ep}}. \quad (4)$$

$D$  is the diffusion constant of a material,  $\tau_{ep}$  is the electron-phonon relaxation time.  $\tau_{ep}$  describes the time the electrons need to release the heat to the phonons. In case of diffusion-cooled HEB, the electrons diffuse into the gold contact before they interact with the phonon bath. The first superconducting HEB mixer was based on a Nb film [30]. In this type of mixer, the diffusion cooling dominates because the thermal diffusion length of 320 nm ( $D(\text{Nb})$  is  $1 \text{ cm}^2/\text{s}$  and  $\tau_{ep}(\text{Nb})$  is 1 ns [12]) is larger than the film length which is in the order of 200 nm or less. The highest measured bandwidth from Wyss et al. [31] is ranging up to 9 GHz.

The issue of the diffusion in comparison phonon-cooled HEB mixers is that the devices are more vulnerable to electrostatic discharge damage due to small film volume [32]. This is crucial for building an array receiver.

### 2.3.2 Phonon-cooled HEB Mixer

The phonon-cooled mixers are cooled by the interaction of the electrons with the phonon bath of the superconducting film. This cooling path is only available in extremely thin films in the order 3 - 5 nm. The film has to be described in the dirty limit of a superconductor instead of a bulk material [33]. The interactions between the electrons, phonons and the bath phonons (substrate of the thin superconducting film) are shown in Fig. 11.

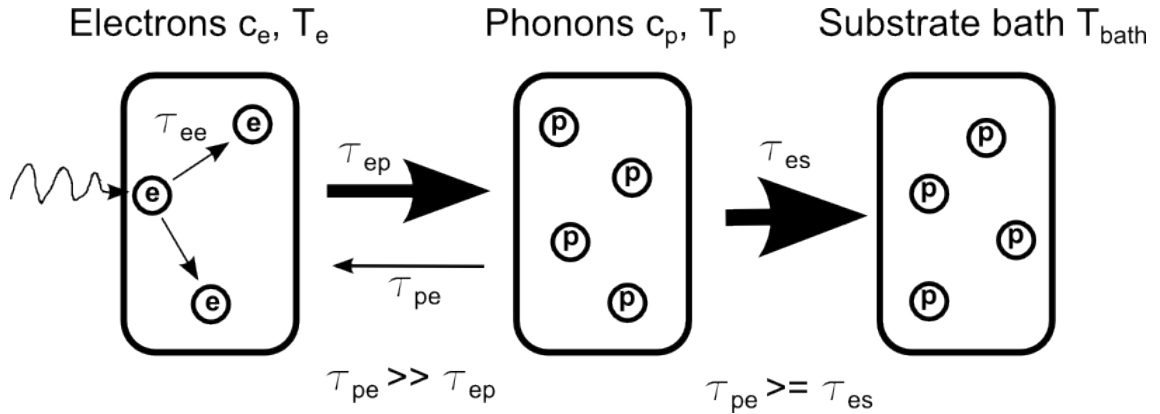


**Figure 11:** The phonon-cooled mechanism of a HEB device with the important interactions.

The interaction time between the electrons  $\tau_{ee}$  is much shorter than the electron-phonon, phonon-electron and phonon-escape times. The electron and phonon temperatures can be seen as a two separate temperature. The exchange of heat between the electrons and the

phonons can be described by two time constants  $\tau_{ep}$  and  $\tau_{pe}$  transferring heat from the hot electrons to the cold phonons and back. In equilibrium  $\tau_{ep}$  is given by:

$$\tau_{ep} = \tau_{pe} \frac{c_e}{c_p}, \quad (5)$$

where  $c_e$  and  $c_p$  describe the specific heat capacity of the electrons and phonons. For the cooling of the hot electrons  $\tau_{ep}$  should be shorter than  $\tau_{pe}$ . The electron-phonon interaction time can be approximated by  $T^{-1.6}$  [34]. The cooling of the phonons depends on  $\tau_{pe}$  and the escape time  $\tau_{esc}$  of the phonons from the superconductor into the substrate. The selection of substrate material plays an important role in phonon-cooled HEB mixers for the transport process. A poor material selection results in a high reflection at the interface between HEB layer and substrates.  $\tau_{esc}$  is given by:

$$\tau_{esc} = \frac{4d}{\beta u}, \quad (6)$$

$d$  is the thickness of the superconductor,  $u$  the speed of sound ( $\sim 4.7$  km/s [35]) and  $\beta$  the acoustic phonon transmission coefficient.  $u$  and  $\beta$  describe the interaction between the substrate and the superconductor. In Il'in et al. [36] the calculated  $\tau_{esc}$  is 38 ps for a 3.5 nm NbN film.

For efficient cooling  $\tau_{esc}$  should be smaller than  $\tau_{pe}$  to prevent heating of the phonons. In the low temperature limit the relaxation time constant  $\tau_{\Theta}$  can be described by:

$$\tau_{\Theta} = \tau_{ep} + \tau_{esc} \frac{c_e}{c_p}. \quad (7)$$

For a larger mixer bandwidth (see Eq. 3), this relaxation or thermal time constant has to be minimized. The phonon-cooled NbN HEBs on Silicon substrates have been shown experimentally to give a IF bandwidth around 4 GHz [34] [37]. This resulted from a thermal time constant of about 40 ps. The devices used in this thesis are phonon-cooled HEB mixers.

### 2.3.3 Critical Temperature and Current of a Superconducting HEB

The devices used for the mixers are based on superconducting materials. The critical temperature and current are important properties of superconductor which are used to describe the thin superconducting film. The temperature of the superconductor at which the resistance disappears is called critical temperature ( $T_c$ ). A measured resistance-temperature (R-T) dependency curve of a HEB is shown in Fig. 12.

Many materials and material combinations were found to become superconducting at a  $T_c$  from a few milli Kelvin to about 39 K for MgB<sub>2</sub> [38].

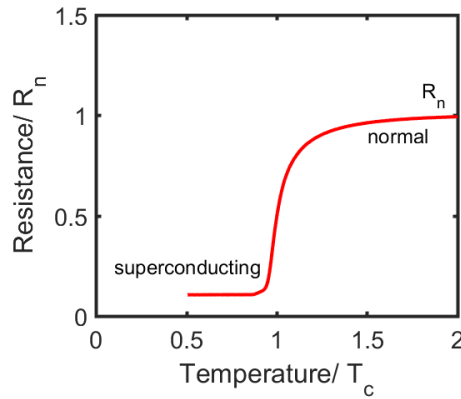


**Figure 12:** R-T curve of a superconductor. The Temperature is normalized by  $T_c$  and resistance by  $R_n$ .

The superconducting property allows a current flow through a superconducting wire without resistance. But this is only true below a certain maximum current called critical current ( $I_c$ ). By increasing bias current in the positive or negative direction the current through the superconductor. Above the critical current  $I_c$  the superconductor changes abruptly to a normal conducting state. The DC current-voltage (I-V) characteristic of a typical superconducting short, thin film are shown in Fig. 13.

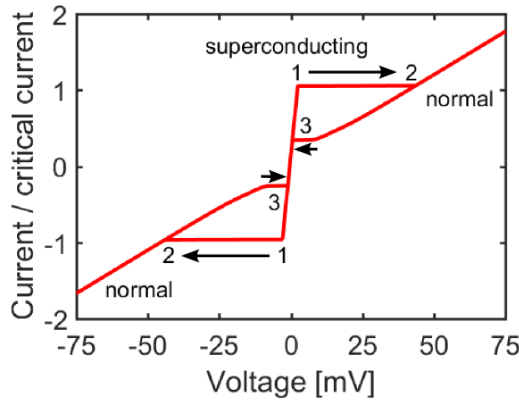


**Figure 13:** I-V curve of a superconductor measured in the current mode scaled to  $I_c$ . The residual resistance in the superconducting state is addressed to the normal conducting contact lines in the HEB circuit.

Starting from zero bias voltage, the current increases with increasing voltage up to the critical current ( $I_c$ ) (point 1). By further increasing the voltage the voltage jumps to point 2 and the superconductor behaves as a normal resistor. When the HEB is in the normal conducting state a decrease of DC voltage below the point 2 does not immediately return to the superconducting phase. At the "retrapping current"  $I_r$  the current jumps at a later point 3 back to the superconducting state [33].

To relate the properties of the interactions to the measurable properties of the film ( $T_c$ ,

$I_c$ ) a theoretical description is needed. There are some theoretical models that attempt to explain the mixing properties of HEB mixers based on a less or more detailed description of the physics of the HEB. There are two main models, the standard model and the hot spot model. The following sections present both models.

### 2.3.4 The Standard Model

The simplest approach to describe the HEB mixing element is by a lumped element model called the standard model. This model was introduced for the description of Nb and YBaCuO HEB films by Gershenson et al. [29]. Here Gershenson et al. assumed that the electron temperature in the film is equally influenced by the radio frequency (RF) and by the direct-current (DC) power. The model is based on a two temperature model by Perrin and Vanneste [39] for a quantitative analysis of the response. The electron temperature  $T_e$  is assumed to be well above the phonon temperature  $T_p$  which is assumed to be equal to the bath temperature  $T$ . The heat flow in the film from the electrons can be described by a heat balance equation:

$$c_e V \frac{\partial T_e}{\partial t} = -A(T_e^n - T^n) + P_{DC} + P_{RF}, \quad (8)$$

where  $c_e$  is the electron heat capacity,  $V$  is the volume of the film,  $\partial T_e / \partial t$  is the partial derivative of the electron temperature over time,  $A$  is a parameter which describes the interaction between electrons and phonons,  $P_{DC}$  is the DC power and  $P_{RF}$  is the RF radiation power coupled to the film. The parameter  $A = n\gamma / (\tau T_c^{n-2})$  depends on the  $T_c$  of the film,  $n$  and a more material parameters which is predominantly dependent on the type of material ( $n = 3.6$  for NbN) and  $\gamma$  is the Sommerfeld constant.

The gain of the of a heterodyne mixer is defined as the ratio of the IF power  $P_{IF}$  at the output and RF signal power  $P_S$  at the input. The mixer gain  $G_m(w_{IF})$  is equal to the ratio of the output power at the  $P_{IF}$  and RF signal power  $P_S$  at the input.  $G_m(w_{IF})$  is defined as:

$$G_m(w_{IF}) = |P_{IF}/P_S| = \frac{2S(w_{IF})^2 P_{LO}}{R_L}, \quad (9)$$

where  $P_{LO}$  is the LO power,  $R_L$  is the load resistance,  $w_{IF}$  the intermediate frequency ( $w_{IF} = 2\pi f_{IF}$ ) and  $S(w)$  the voltage responsivity.  $S(w)$  is given by Karasik et al. in the case for the lumped element model [40]:

$$S(w_{IF}) = \frac{\alpha}{I_0} \frac{C}{(1 - C \frac{R_0 - R_L}{R_0 + R_L})} \frac{R_L}{R_0 + R_L} \frac{1}{1 + iw_{IF} \tau}, \quad (10)$$

where  $R_0$  and  $I_0$  are the HEB DC resistance and current at the bias operation point,  $\alpha$  is

the optical coupling of the signal,  $C$  is the self-heating parameter and  $\tau$  is a modification of the electron temperature relaxation time  $\tau_{\Theta}$ .

The physical resistance  $R_0$  of the bridge at the mixing state is still discussed.  $R_0$  is equal to  $R_n/2$  in broken-line transition model [40]. It can also be described by the differential resistance at the operating point. In the hot spot model  $R_0$  is defined by an integral of resistivity as a function of the electron temperature over the length of the bridge [41]. It is still under discussion what the correct definition is. I will use the broken line transition definition for further analysis in this thesis.

By combining both equations Eq. 9 and 10 the mixer gain can be calculated as a function of IF. It can be divided into three parts:

$$G_m(w_{IF}) = \underbrace{\frac{2\alpha^2 C^2 P_{LO}}{I_0^2}}_{\text{zerogain}} \cdot \underbrace{\frac{R_L}{(R_0 + R_L)^2} \frac{1}{(1 + C \frac{R_0 - R_L}{R_0 + R_L})^2}}_{\text{impedance}} \cdot \underbrace{\frac{1}{1 + (w_{IF} \tau)^2}}_{\text{bandwidth}}. \quad (11)$$

The zero gain part in Eq. 11 is the gain at zero IF, the impedance part describes the mismatch of the IF output impedance of the mixer and the load impedance of the IF system. The bandwidth part characterizes the dependence on IF.

The modified thermal time constant  $\tau$  is defined by:

$$\tau = \frac{\tau_{\Theta}}{1 + c \frac{R_0 - R_L}{R_0 + R_L}}. \quad (12)$$

The self-heating parameter  $C$  depending on the change of the resistance with dissipated power is:

$$C = I_0^2 \frac{dR}{dT} / G_{th}, \quad (13)$$

where  $dR/dT$  is slope at  $T_c$  and  $G_{th}$  is the thermal conductance to the bath,  $V$  is the film volume and  $A$  is parameter from Eq. 8. The thermal conductance can be obtained by  $G_{th}(T_e) = nAVT_e^{n-1}$ .

The standard model can be further approximated with broken-line transition model in the next section.

### 2.3.5 Broken-Line Transition Model

Karasik et al. using a broken-line transition model to further simplify the model of the mixer gain [40]. In this model the electron temperature is assumed to be equal to  $T_c$ ,  $R_0$  is  $R_n/2$  and  $C = 1$ . For a low operation temperature  $T_c^n \gg T^n$  and a narrow transition width

( $\Delta T_c \ll T_c$ ) the gain as a function of the IF is giving by:

$$G_m(w_{if}) = \frac{\alpha}{n} \frac{T_c}{\Delta T_c} \frac{R_L}{R_0} \frac{1}{1 + (w_{IF} \tau)^2}. \quad (14)$$

$\tau$  can be expressed in this approximation as a function of  $T_c$ :

$$\tau = \underbrace{\frac{1}{2\pi\Delta f}}_{film} \cdot \sqrt{1 + \frac{T_c}{\Delta T_c}} \cdot \underbrace{\frac{1}{(1 + \frac{R_0 - R_L}{R_0 + R_L})}}_{impedance}, \quad (15)$$

where the influence of the impedance and the film are marked in the equation.  $\tau$  is a function of the noise bandwidth  $\Delta f$ . The bandwidth of a mixer can be determined either by the gain or by the noise bandwidth. The gain or noise bandwidth is defined as the bandwidth in which the gain or the noise is increased by a factor of 2 of its minimum value at 0 Hz. The mixer noise bandwidth for this model is given by:

$$\Delta f = \frac{1}{2\pi\tau_\Theta} \sqrt{1 + \frac{T_c}{\Delta T_c}}. \quad (16)$$

To estimated the noise bandwidth of the mixer, we calculated  $\tau_\Theta$  with the empirical formulas [34] [36] [42]:

$$\begin{aligned} \tau_{eph} &= 500 \cdot T_e^{-1.6} (ps K^{1.6}) \quad [34] \\ \tau_{esc} &= 10.9 \cdot d (ps nm^{-1}) \quad [36] \\ c_e &= 1.85 \cdot 10^{-4} \cdot T_e (Jcm^{-3} K^{-2}) \quad [42] \\ c_{ph} &= 9.7 \cdot 10^{-6} \cdot T_e^3 (Jcm^{-3} K^{-4}) \quad [42]. \end{aligned} \quad (17)$$

We assume that the electron temperature  $T_e$  is equal to  $T_c$ . The noise bandwidth as a function of  $T_c$  is calculated for two design film thicknesses of 3.5 and 4.5 nm with a measured  $\Delta T_c$  of 1.5 K shown in Fig. 15. The theoretical expected noise bandwidth calculated with Eq. 16 for a film with a thickness of 3.5 nm is between 10 and 18 GHz for a  $T_c$  between 7 and 9 K. The bandwidth of a thicker film for the same  $T_c$  is about 0.5 GHz smaller.

The gain at the typical IF operation frequency of  $f = 1.5$  GHz is results from the combination of Eq. 14 and 15:

$$G_m(f) = \underbrace{\frac{n}{\alpha} \frac{T_c}{\Delta T_c} \frac{1}{1 + (\frac{f}{\Delta f} \cdot \sqrt{1 + T_c/\Delta T_c})}}_{film} \cdot \underbrace{\frac{R_L}{R_0} \frac{1}{(1 + \frac{R_0 - R_L}{R_0 + R_L})^2}}_{impedance}. \quad (18)$$

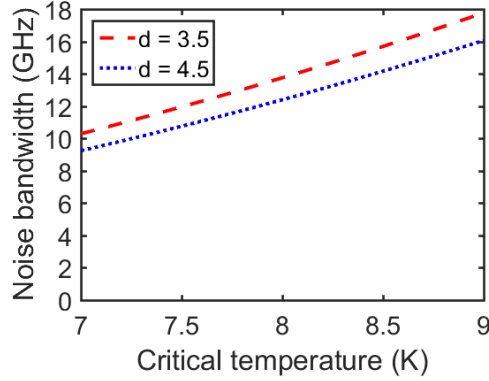


**Figure 14:** Theoretical noise bandwidth as a function of the critical temperature for two different thickness of the HEB based on a calculation from Eq. 16

The mixer gain dependency of  $T_c$  at a IF of 1.5 GHz for three  $\Delta T_c$  was shown in Fig. 15. The two subplots were calculated for typical values of the noise bandwidth of 3 and 4 GHz for NbN HEB mixers. The expected gain of the mixers was in the range of -2 to -7 dB.

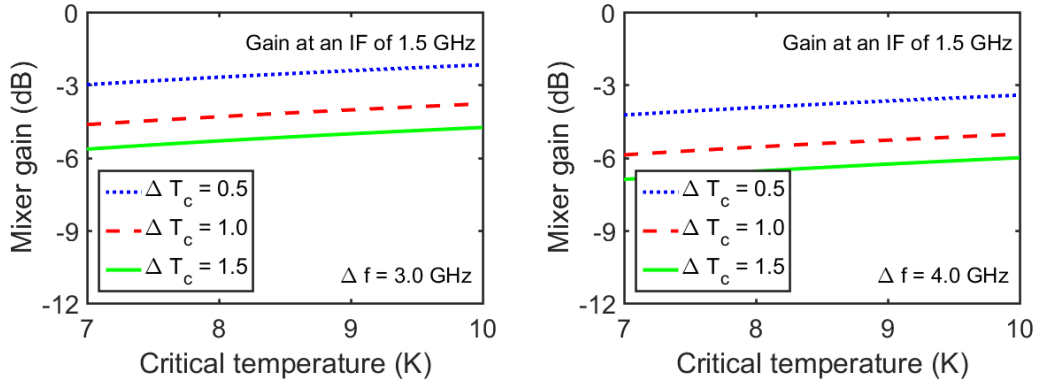


**Figure 15:** Theoretical mixer gain as a function of the critical current for three different transition widths. Assuming a noise bandwidth of 3.0 or 4.0 GHz.

According to this model the HEB mixer input noise temperature depends on the Johnson noise  $T_J$  (thermal noise), fluctuation noise  $T_{FL}$  and quantum noise  $T_{QN}$ . Johnson noise or thermal noise is generated in the HEB "resistor" by the electron temperature. The origin of the fluctuation noise  $T_{FL}$  is the thermal fluctuation of the electron temperature caused by a random energy exchange in the reservoir. The quantum noise contribution to the mixer noise appears even if a mixer is at the absolute zero temperature where the other contribution were zero. The quantum noise temperature at the output of a mixer  $\frac{hf}{2k_B}$  (K) is an unavoidable contribution caused by (a double side band (DSB)) the mixing process. It is considered as vacuum fluctuations (fluctuation-dissipation theorem) in the input signal. The fluctuation and Johnson noise temperature in the lumped element model were given by [40]:

$$\begin{aligned}
T_J &= \frac{2T_e P_{DC}}{\alpha^2 P_{LO}} [1 + (w \cdot \tau_{\Theta})^2] \\
T_{FL} &= \frac{2T_e^2 G}{\alpha^2 P_{LO}},
\end{aligned} \tag{19}$$

where  $T_e$  is the electron temperature,  $G$  the thermal conductance which is giving by  $c_e V / \tau_{\Theta}$ .

In the broken-line transmission model  $G$  is equal to  $nAVT_e^{n-1}$ ,  $T_e = T_c$  and  $R = R_n/2$ . In the case of  $T_c \gg T$  and  $\Delta T_c \ll T_c$  the input noise temperature at a frequency  $w$  is given by:

$$\begin{aligned}
T_J &= \frac{n\Delta T_c}{\alpha} [1 + (w \cdot \tau_{\Theta})^2] \\
T_{FL} &= \frac{nT_c}{\alpha} \\
T_{QN,DSB} &= \frac{hf}{2k_B}
\end{aligned} \tag{20}$$

The sum of the contributions is equal to the mixer noise temperature. The theoretical expected noise temperature is calculated and listed in Tab. 2.3. The theoretical expected mixer noise temperature for typical 1.89 THz mixer with listed properties is about 80 K.

noise contribution	noise temperature (K)
$T_J$	5
$T_{FL}$	31
$T_{QN}$	45
$T_{total}$	81

**Table 2:** The noise contribution is calculated with measured typical mixer properties. A  $T_c$  8.5 K,  $\Delta T_c$  of 1.5 K,  $n$  of 3.6 and a  $\alpha$  of 1 at 1.89 THz.

Another approach for the description of the HEB is the hot-spot model in which the electron temperature is a gradient over the length of the HEB. This model is discussed in the following section.

### 2.3.6 Hot-Spot Model

A further approach is the concept of a hot-spot model [43], [44]. Here one assumes that the temperature of the HEB is not uniform because the HEB has a temperature gradient over the device along the bridge length. In the hot spot model the typical temperature profile in one-dimensional gradient along the length of the bridge ( $L$ ) is shown in Fig. 16.

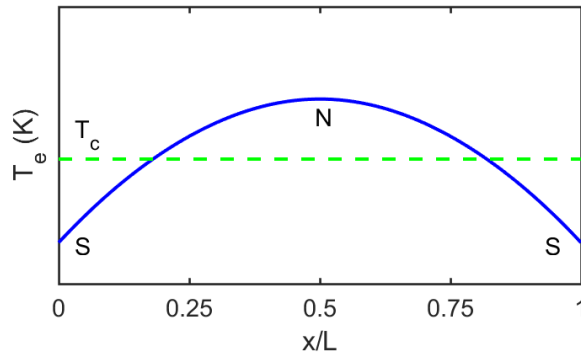


**Figure 16:** Schema of a 1D electron temperature in the HEB as a function of the length of the bridge. N is the normal conducting part in the center of the bridge and S the superconducting part at the contact pads.

Here only a small part of the film is in the operating region. The main part of the film is normal or superconducting (see Fig.16).

The electron temperature  $T_e$  can be expressed by a one-dimensional distributed heat balance instead of being constant in the lumped element model. Wilms Floet et al. [43] explain the hot-spot formation by a heating in the center of the bridge by absorption of LO and DC power.

By introducing a weak RF signal with a slightly different frequency than the LO results in a modulation of dissipated power. This modulation changes the length of the hot-spot. Merkel et al. [44] interpreted the hot-spot as different heating efficiency of the DC and the RF depending on the position of the bridge. The RF power is uniformly absorbed by the bridge and the DC power is absorbed only at the normal contacting parts of the bridge which is the hot-spot at the center of the bridge. Both models can evaluate the DC I-V characteristics only by introducing correction factors. Barends et al. used the measured R-T curve to calculate the theoretical DC I-V characteristics which were in fair agreement with the measurements [45].

The heat balance equations were given for the electrons and the phonons:

$$\begin{aligned}
\frac{dT}{dx}(\lambda_e \frac{d}{dx} T_e) + p - p_{ep} &= 0, \\
\frac{dT}{dx}(\lambda_e \frac{d}{dx} T_e) + p_{ep} - p_{ps} &= 0,
\end{aligned} \tag{21}$$

where  $T_e$  and  $T_p$  are the electron/phonon temperature,  $\lambda$  is the thermal conductance and  $p$  the sum of the absorbed DC and RF power. The power propagation from the electrons to the phonons and from the phonons to the substrate called  $p_{ep}$  and  $p_{ps}$ ,

$$\begin{aligned}
p_{ep} &= \frac{c_e}{n\tau_{ep}T_e^{n-1}}(T_e^n - T_p^n) \\
p_{ps} &= \frac{c_p}{n\tau_{esc}T_p^{m-1}}(T_p^m - T^m),
\end{aligned} \tag{22}$$

where  $\tau_{ep}$  is the electron-phonon relaxation time,  $\tau_{esc}$  is the phonon escape time,  $c_e$  and  $c_p$  the electron/phonon heat capacity and  $n = 3.6$  because we described NbN and  $m = 4$  is found in [46]. The LO power is assumed to be absorbed homogeneously over the bridge which is valid for frequencies above the gap frequency (for a bulk NbN  $\sim 1.3$  THz) and the DC power is only absorbed in the hot-spot. In addition, any non-equilibrium effects were ignored. As a boundary condition the temperature of the edge of the bridge has to be equal to the bath temperature of the contact pads. The mixer gain in the hot spot model is given by:

$$G_{mixer} = \frac{2(I_0 C_{RF})^2 P_{LO} R_L}{(R_0 + R_L)^2} \frac{1}{(1 + C_{DC} I_0^2 \frac{R_0 - R_L}{R_0 + R_L})^2}, \tag{23}$$

where  $C_{RF}$  and  $C_{DC}$  are the heat capacities of the absorbed DC and RF power. The mixer noise temperature of the hot-spot model similar to the lumped element contribution from Eq. 19 by [40]. The noise temperature contributions at the minimum of the IF is given by.

$$\begin{aligned}
T_{Johnson} &= \frac{2T_e R I_0^2}{\alpha^2 P_{LO}} \\
T_{Fluctuation} &= \frac{2T_e^2 G}{\alpha^2 C_{RF}^2 P_{LO}}.
\end{aligned} \tag{24}$$

## 2.4 Detection Principle

As shown in Sec. 1.3 the heterodyne detection is preferred for observation of spectral resolved transition line in the THz range.

In the THz-range no low noise amplifiers (LNAs) were available. Thus heterodyne mixers were used to down converting the THz signals (RF) into the GHz range. After down conversion to the GHz intermediate frequency (IF) signals can be amplified with LNAs. The IF signals can then be processed and detected. For the heterodyne detection the RF signal has to be combined with a reference signal. The reference signal has a large amplitude (output power of about several  $\mu\text{W}$ ) at fixed frequency and preferably phase locked, with a shift of about 1 GHz to the RF frequency. It is called a local oscillator (LO). In my work I focus on the double sideband (DSB) heterodyne receiver which is shown in the shape of Fig. 19. The block diagram a.) shows the principle of the coupling of the signal and LO to the spectrometer. In diagram b.) a schematic of a DSB receiver down converting process is shown. The RF and the LO signal were combined with a beamsplitter. Then both signals are coupled via an antenna to the mixer.

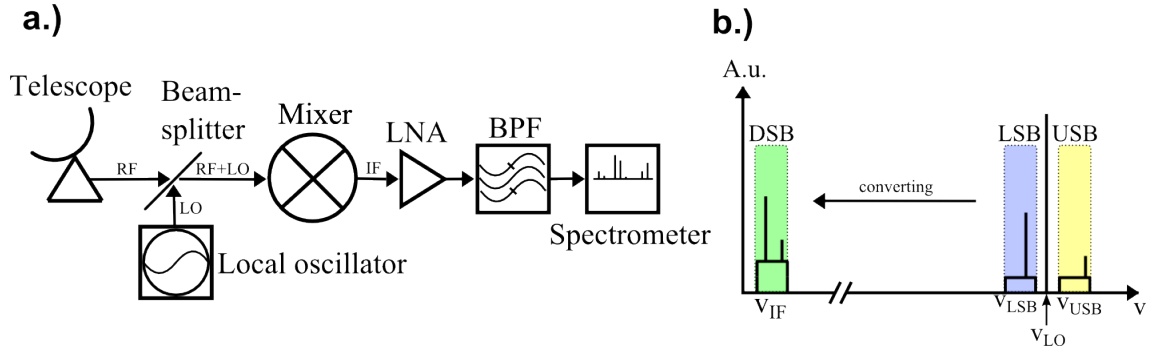


**Figure 17:** a.) show a block diagram of a heterodyne receiver. b.) show a schema of the DSB mixing process.

The main property of a mixer is the highly non linear I-V characteristic. For classical mixers such as a Schottky diodes the LO reference signal and the observation signals are multiplied. For HEB mixer the sum of both voltage signals is mixed. The dissipated power of the Signal and the LO in the mixer is equal to:

$$\begin{aligned}
 P_{RF} &= \frac{1}{R} [V_S \cdot \cos(wst) + V_{LO} \cdot \cos(w_{LO}t)]^2 \\
 &= \frac{1}{R} \left[ \underbrace{V_S^2 \cdot \cos^2(wst) + V_{LO}^2 \cdot \cos^2(w_{LO}t)}_1 + \underbrace{2V_S V_{LO} \cdot \cos(wst) \cos(w_{LO}t)}_2 \right], \quad (25)
 \end{aligned}$$

where V the voltage and w the angular frequency ( $w=2\pi f$ ). To approximate the dissi-

ated power two trigonometric identities has to be used to simplify the equation 25

$$\begin{aligned} \cos^2(x) &= \frac{1 - \cos(2x)}{2} \\ \cos(x)\cos(y) &= \frac{\cos(x-y) - \cos(x+y)}{2}. \end{aligned}$$

Using those two identities the dissipated power is then given by:

$$\begin{aligned} P_{RF} &= \frac{1}{R} \left[ \frac{V_S^2}{2} (1 - \cos(2w_S t)) + \frac{V_{LO}^2}{2} (1 - \cos(2w_{LO} t)) \right. \\ &\quad \left. + V_{LO} V_S [\cos((w_{LO} - w_S)t) - \cos((w_{LO} + w_S)t)] \right] \\ &= \frac{1}{R} \left[ \frac{V_S^2 + V_{LO}^2}{2} + \frac{V_{LO}^2 \cos(2w_{LO} t)}{2} + \frac{V_S^2 \cos(2w_S t)}{2} \right. \\ &\quad \left. + V_{LO} V_S [\cos((w_{LO} - w_S)t) - \cos((w_{LO} + w_S)t)] \right]. \end{aligned} \quad (26)$$

Only the difference of both signals ( $w_S - w_{LO}$ ) is dominating the dissipated power. The result of the output signal is given approximated by:

$$P_{RF} \approx \frac{1}{R} \left[ \frac{V_S^2 V_{LO}^2}{2} + V_{LO} V_S \cdot [\cos((|w_{LO} - w_S|)t)] \right]. \quad (27)$$

The frequency band above the LO frequency called the upper sideband (USB) and below the LO frequency the lower sideband (LSB). Both sidebands the positive and negative difference of the LO frequency mixed to the IF (see Fig:19 b.)). This type of mixer, a double sideband (DSB) mixer adds signals and noise from both sidebands into the IF band.

During heterodyne measurement the so called direct detection effect can increase the receiver noise temperature. The origin and a solution to avoid this effect were discussed in the next section.

#### 2.4.1 Direct Detection

HEB Mixers can also be used as a direct detector. The so called direct detection effect appears in a HEB Mixer during a heterodyne measurement when the input port signal is changed from the hot to the cold load at a constant LO input power level. Due to the low LO power requirement of a HEB mixer the change in input power of the load is large enough to be directly detected by the HEB, thereby changing the bias conditions for the heterodyne

detection of the hot/cold load. The reason for the power change is the black body radiation, which heats the electrons in the HEB. The measured bias current changes about  $0.4 \mu\text{A}$ , at an average current of  $30 \mu\text{A}$ , for the case in Fig. 18. Since the mixer gain is a function of the bias current the gain changes, and the condition for an accurate hot/cold calibration of the heterodyne sensitivity is violated. This direct detection effect is observable directly in the I-V curve (see Fig. 18). The effect on the hot/cold calibration is such that at the hot load input the mixer DC current is smaller than at the cold load input, which reduces the mixer gain, whereby IF output power at the hot load input is less than without the direct detection effect. The direct detection effect falsely increases the measured heterodyne noise temperature using the Y-factor method.

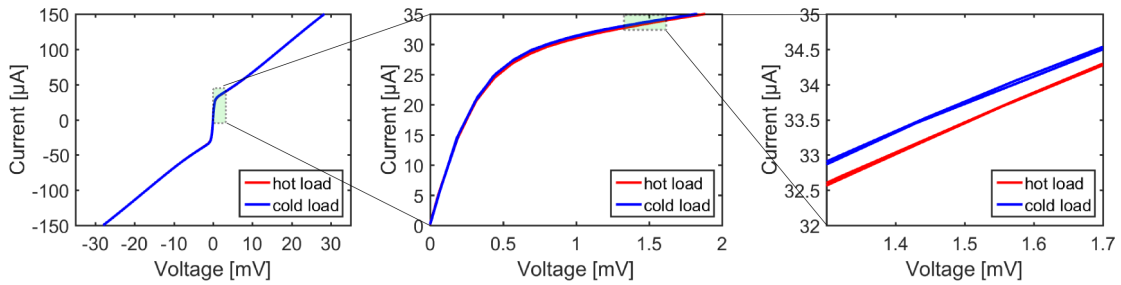


**Figure 18:** DC-I-V curve of the optimal LO power level operation for a typical HEB. The red curve representing the hot load as an input port for the mixer and blue the cold load.

The change of the bias current leads to a change in the mixer gain. This change in gain is followed by a reduced Y-factor and an increased  $T_{rec}$ . This effect can be suppressed by adjusting the LO power level each time when changing the loads to keep the observed DC-bias current identical for each load input [47]. For astronomical observation, particular for an array, it is not possible to individually compensate for each single mixer to change the LO power level.

The strength of the direct detection effect depends absolutely on the load temperatures and on the RF bandwidth of the mixer. Waveguide mixers have the advantage of a low frequency cut-off there below no signal is coupled to the HEB and a high frequency over-modulation of the waveguide where the waveguide probe is not so effective anymore. The RF bandwidth of a waveguide mixer is generally less than 1 octave. In the laboratory, we also can use the direct detection for measuring the broadband RF response of a HEB mixer which I will explain in Sec. 5.2.

The definition of the sensitivity of a heterodyne receiver is discussed in the next section with a focus on the 2 - 5 THz frequency range.

## 2.5 Receiver Sensitivity

The sensitivity of a receiver system depends on the fundamental quantum noise limit and of noise the different components. The output power of the receiver is written as:

$$P_{rec} = P_{in} \cdot G_1 G_2 \cdots G_n + P_1 G_2 \cdots G_n + \cdots, \quad (28)$$

where  $P_{in}$  is the power of the input signal,  $G_i$  is the gain and  $P_i$  is the input noise of a component. For  $P_{in}$  we usually use a blackbody. The spectral radiation of a blackbody is given by Plancks law:

$$B_f(T, f) = \frac{2hf^3}{c^2[\exp(\frac{hf}{k_B T}) - 1]}, [W \cdot m^{-2} sr^{-1} Hz^{-1}] \quad (29)$$

where  $f$  is the frequency,  $T$  physical temperature,  $c$  the speed of light,  $h$  the Planck constant and  $k_B$  the Boltzmann-Konstante. The power emitted per mode over a bandwidth  $B$  from a black body is given by

$$P_{Planck}(T, f) = \frac{\frac{hf}{B}}{\exp(\frac{hf}{k_B T}) - 1} \cdot [W] \quad (30)$$

At low frequencies  $f$  and high physical temperatures  $T$  the emitted power per mode can be approximated by the Rayleigh-Jeans approximation because  $hf \ll k_B T$ . The noise power is then proportional to an  $T$  by  $P = k_B T / B$ . For the frequency range of 2 - 5 THz it can thus not be approximated because  $hf$  is in the same order of magnitude as  $k_B T$  for temperature range of 10 K - 300 K. Instead of an approximation the Planck power emitted per mode has to determine the power delivered by the blackbody input signal.

In the description of the dissipation-fluctuation theorem, the fluctuation noise is added to the Planck power emitted per mode is given by Callen-Welton (CW) [48]:

$$P_{CW}(T, f) = k_B T B \frac{\frac{hf}{k_B}}{\exp(\frac{hf}{k_B T}) - 1} + \frac{hfB}{2k_B}. \quad (31)$$

The additional noise is the fluctuation noise which is introduced by the receiver system itself. The noise power in a bandwidth  $B$  is represented by a equivalent noise temperature:  $T_i = \frac{P_i}{k_B B}$ . A comparison of the equivalent noise temperature determined with the input power calculated with Planck, Callen-Welton and the Rayleigh-Jeans as a function of the physical temperature is shown in Fig. 19.

At the operation frequency of 1.9 THz and between the temperatures 77 K and 295 K the calculated mixer noise temperature determined using the Callen-Welton expression Eq.

31 converges to Rayleigh-Jeans expression but at a frequency of 4.7 THz this is not valid anymore.

In measurement Sec. 6 we used Planck power per mode to calculate the receiver performance, which is used for observation at the telescopes. The Callen-Welton power per mode was used for the calculation of mixer noise temperature because the additional quantum noise which is always present was not attributed to mixer noise.

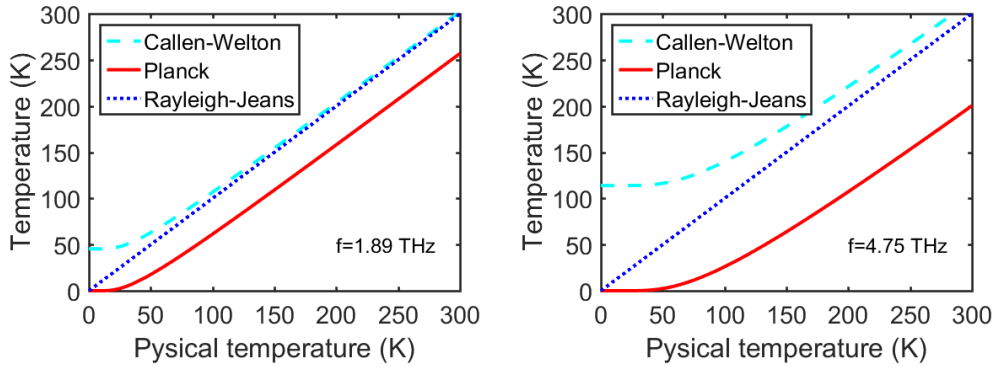


**Figure 19:** Noise temperature as a function of physical temperature (operation frequency 1.9 and 4.7 THz) determined by the input power per mode from Planck/Callen-Welton/Rayleigh-Jeans expression.

The equivalent temperature is determined by the input power from Planck and Callen-Welton for two typical physical load temperatures of 298 K and 77 K operating at 1.9 THz and 4.7 THz are listed in Tab. 3.

Frequency	1.9 THz		4.7 THz	
Physical temperature	298	77	298	77
	(K)	(K)	(K)	(K)
Planck	255	40	199	13
Callen-Welton	300	86	312	126

**Table 3:** Calculated temperature based on input power from Planck and Callen-Welton per mode from a two typical physical temperature of 298 K and 77 K for the two operation frequency 1.9 THz and 4.7 THz.

From Eq. 28 the equivalent receiver noise temperature ( $T_{rec}$ ) is given by:

$$T_{rec} = T_1 + \frac{T_2}{G_1} + \frac{T_3}{G_1 G_2} + \dots + \frac{T_n}{G_1 G_2 \dots G_{n-1}}. \quad (32)$$

The gain can be calculated from Eq. 28 by a different measurement. The sensitivity of a receiver system is calculated by the "Y-factor"-method. The "Y-factor"-method enables the calculation of the receiver noise temperature ( $T_{rec}$ ) with a calibration measurement. For the measurement two black bodies with a well known physical temperature were necessary.

The absorbing loads were approximated black bodies (perfect absorbers). The Y-factor is defined as the ratio between the IF output power of the receiver at the hot (room temperature) load input and at the cold load input (floating in liquid Nitrogen):

$$Y = \frac{P_{out,hot}}{P_{out,cold}} = \frac{T_{rec} + T_{in,hot}}{T_{rec} + T_{in,cold}}, \quad (33)$$

where  $T_{in,hot}$  and  $T_{in,cold}$  are the equivalent temperatures.  $T_{rec}$  can then be obtained by:

$$T_{rec} = \frac{T_{in,hot} - YT_{in,cold}}{Y - 1}. \quad (34)$$

This technique is used for the calibration for all observations. It assumes that the mixer response varies linearly with input load temperature and that there are no saturation effects of any component of the receiver. In addition, the gain can be calculated by the difference of the output power which will be discussed in Sec. 6.1.7.

In the next section we continue with the mixer circuit design and the fabrication steps for the HEB mixer devices for The GREAT LFA and H-channel.

### 3 Mixer Design and Fabrication

The following chapter deals with the design concept and the fabrication of the mixers. First the conceptual mixer design for all mixers with coupling of the radiation to the HEB is presented (see Sec. 3.1) followed by the individual design for the operating frequencies of 1.9 and 4.7 THz and the fabrication of the devices, mixer blocks and the feedhorns (see Sec. 3.2) as well as the assembly of the mixer blocks.

#### 3.1 Mixer Design

The hot electron bolometer device as non-linear element is much smaller few  $\mu\text{m}$  in width and few hundreds nm in length (see Sec. 2.3) than the wavelength (158 or 63  $\mu\text{m}$ ) of the radiation it responds to. A small area of the film is required to reduce to required incident LO power [40] and to match the impedance film of the circuit (see Sec 3.1.1). An antenna is therefore required to effectively couple to the free-space radiation field. Principally, two different technological approaches are used: One using a dielectric lens and a planar open structure antenna [49] [50] and the other with a waveguide feedhorn and antenna. Both options have their advantages and disadvantages. The quasi-optical mixers based on a circuit on a substrate which is glued on a hemispherical silicon lens. This lens focuses the radiation on the antenna. For the coupling of the free-space radiation to the HEB a twin slot antenna or a spiral antenna is most commonly used [51],[52],[53]. The waveguide mixers based on a feedhorn, which has a transition at the end of the horn to the waveguide.

I focus on our own development based on waveguide feedhorn coupling. One significant advantage is the decoupling of the optical parameters of the circuit to the feedhorn. The waveguide based mixers were well established in the GREAT and HIFI instrument ([54], [55]).

The 1.9 and 4.7 THz mixer designs based on a further development from Pütz et al. [21] which was designed and simulated by Netty Honingh. The designs were adopted for the different frequency and observation target. The circuits are designed (see Sec. 3.1.1 and 3.1.3) for optimal coupling from the waveguide to the HEB over the designed RF band.

The input waveguide to the HEB device defines the low frequency cut-off frequency of the mixer and also acts as a linear polarizer to the electromagnetic field. The electric field vector is parallel to the short side of the waveguide. The longer length of the waveguide defines the cut-off frequency which is proportional to the length (e.g. 48  $\mu\text{m}$  length, resulting in a cut-off frequency of 1.56 THz). The longer waveguide width defines the waveguide impedance.

The simulation of the mixer circuits is done with the Computer Simulation Technology (CST) microwave studio (MWS) with 3D EM simulation packages [56].

### 3.1.1 1.9 THz Circuit Design

The 1.9 THz circuit design is based on the GREAT NbTiN mixer design [21]. In this design the waveguide probe is connected to a Co-Planer Waveguide (CPW) transmission line on a substrate. The antenna is matched to the electrical field of a waveguide cavity, capacitors and the RF choke. The combination of the capacitors and the RF inductors (on the IF line) acts as low pass filter in the IF line, which reflects the RF radiation. The capacitor and the Rf chokes are located in a substrate channel. Fig. 20 shows a 3D cut and S21 (square root of the transition) coupling from the waveguide (port 1) to the HEB (port 2).

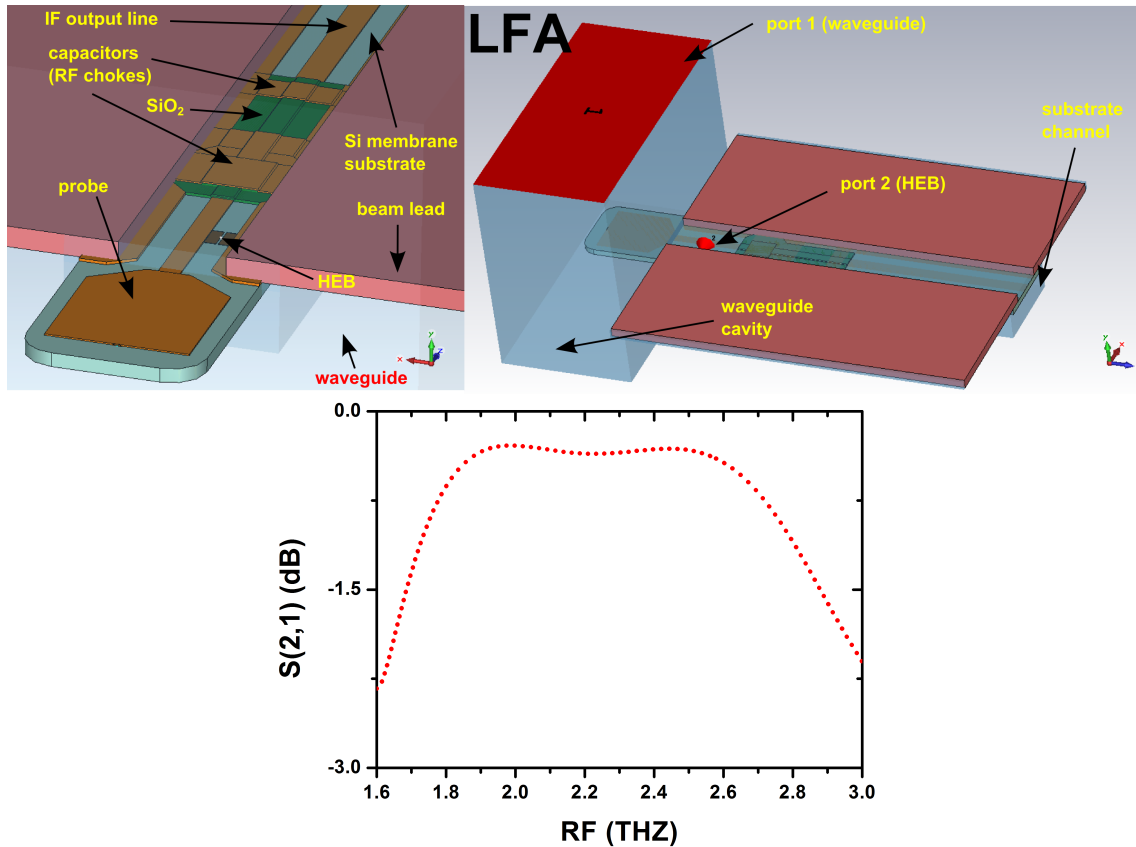


**Figure 20:** The top left and right are the cuts of the LFA-2 design in the CST MWS. The S21 (square root of the transition) from the waveguide port 1 to the HEB port 2 is shown in the bottom plot in dB as a function of the RF in THz.

The RF response is optimized to have a wide response between 1.9 - 2.5 THz to cover several line transitions. One of the main transition to be observed in this frequency band is

the C<sup>+</sup> fine structure line at 1.9 GHz (see Sec. 1.1). The circuit consists of a 200 nm thin gold on a 2  $\mu\text{m}$  Si membrane substrate. 400 nm of the dielectric SiO<sub>2</sub> is deposited for the fabrication of the capacitors. The circuit is surrounded by a 3  $\mu\text{m}$  thick gold beam leads. The beam lead technology is used for positioning the device on top of the waveguide and for the contact to ground of the circuit. Also beam leads act as a RF “gasket” between the horn and the block with a clean electrical contact. Further, they buffer the strain caused by differential contraction of different materials at cryogenic temperature to avoid mechanical stress.

An impedance matching is important for low loss coupling of the RF radiation to the HEB. Two designs (LFA1 and LFA2) with the similar circuit design with different impedances (80 and 120 Ohm) are fabricated on the same wafer to concern the impedance mismatch. The impedance depends of the width of the NbN film (4.5  $\mu\text{m}$  for LFA1 and 3.5  $\mu\text{m}$  for LFA2). The width of the film and small shifts in the direction of the waveguide can be used to adjust the impedance for further wafer runs.

### **3.1.2 IF Impedance Mismatch**

The device response is calculated from the waveguide to the HEB without the IF output of the mixer. The IF mismatch between the HEB and the SMA connector is assumed to be negligible. To verify the transmission from the mixer to the IF output at the SMA connector a simulation in CST was done (see Fig. 21). The result for typical resistance values are shown in Fig. 22. The transmission losses are below -1 dB over the band from 0 - 5 GHz with a maximum change of gain over the band of - 0.5 dB, assuming that the IF output impedance of the HEB device equals its normal state resistance.

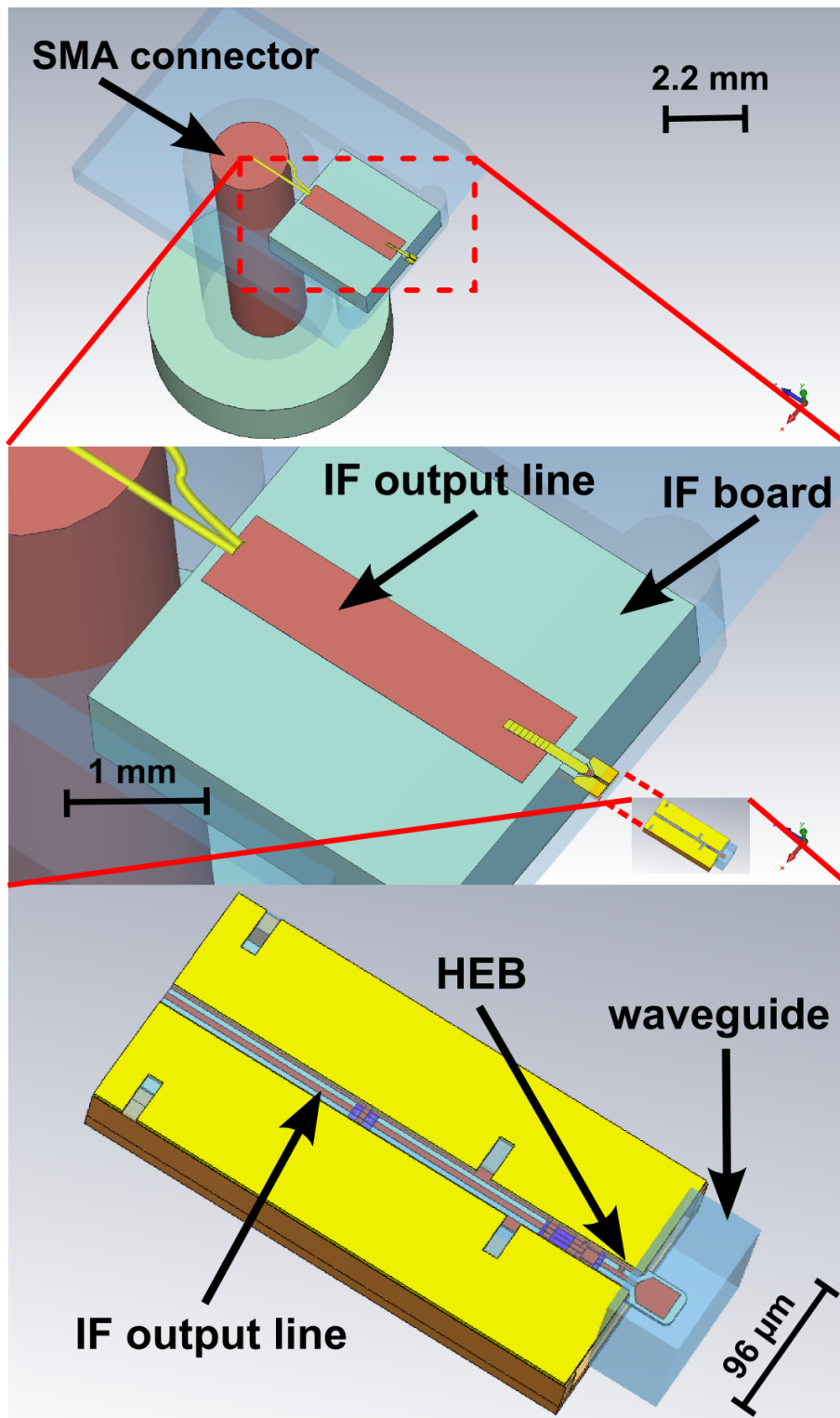


**Figure 21:** 3D model of the IF transmission path from the HEB to the SMA connector (IF output of the mixer block).

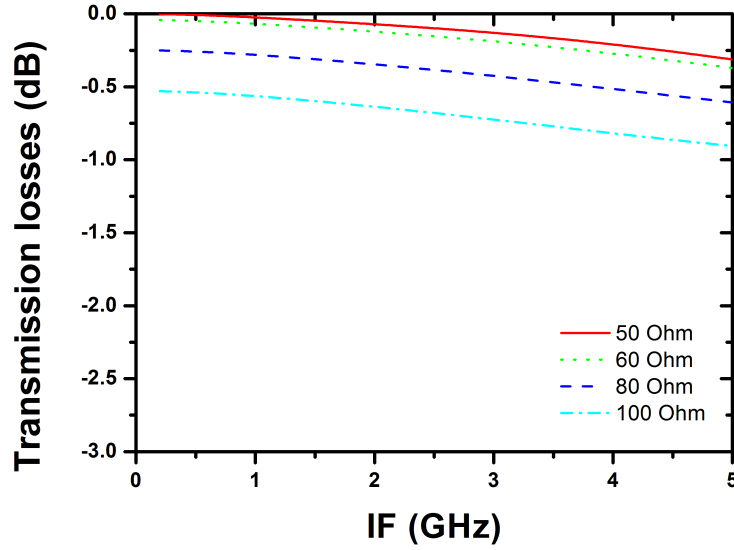


**Figure 22:** Transmission losses calculated with CST for typical impedance  $R=R_n/2$  between 50 and 100 Ohm based on the broken line transmission model (see 2.3.5).

### 3.1.3 4.7 THz Circuit Design

The focus for the 4.7 THz mixer is observing the O fine structure line at the rest frequency of 4.7448 THz [57] (see Sec. 1.1). For the observation of this transition no broadband response is necessary. For the 4.7 THz circuits two designs were chosen to fabricate. The designs HFA-3 and HFA-1b differ from the use of the dielectric  $\text{SiO}_2$ . The HFA-1b design is based on a circuit without  $\text{SiO}_2$  because the electromagnetic properties of  $\text{SiO}_2$  at cryogenic temperature and at the operating frequency of about 5 THz are unknown. The HFA-3 design is based in principle of the LFA circuit which is scaled to higher frequencies. The HFA-3 design has a broadband RF response of 1.5 THz to be able to cover in addition also other lines. The HFA-1b design has only a peak response with a bandwidth of 0.5 THz. The design consists of a standard suspended micro strip, RF choke and an E-plane waveguide probe. A  $\lambda/4$  inductive high impedance line is used as the DC and IF contact to the ground on the other side of the waveguide. In Fig. 23 the 3D cut and the S21 from the waveguide to the HEB are shown for both designs. Depending on the measurement results one of those designs will be chosen for the upGREAT array.

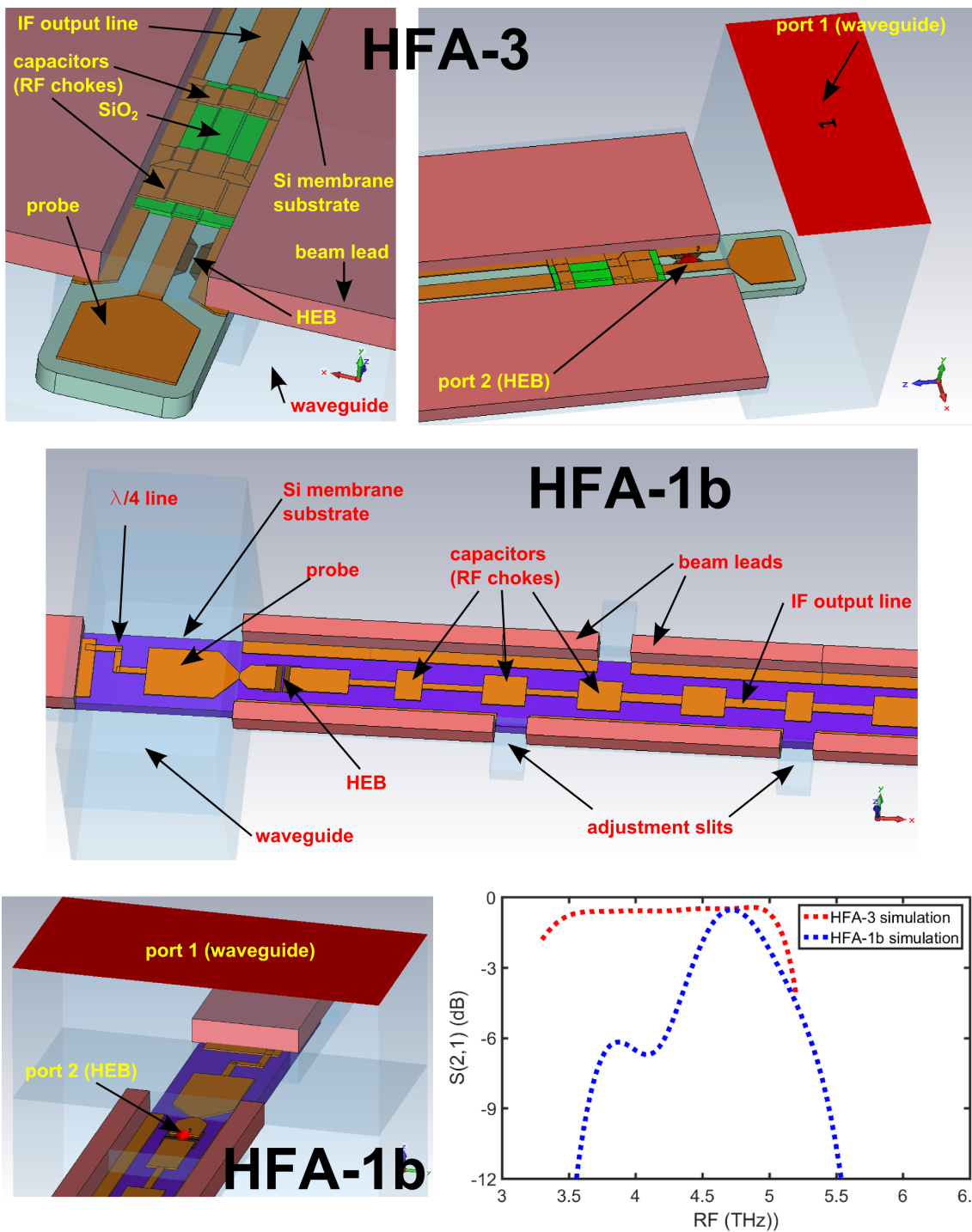


**Figure 23:** The top left and right are 3D cuts of the HFA-3 design in the CST MWS. The middle and the bottom left are 3D cuts of the HFA-1b. The S<sub>21</sub> from the waveguide port 1 to the HEB port 2 is shown in the bottom right plot in dB as a function of the RF frequencies in THz for both designs.

## 3.2 Fabrication and Assembly

The fabrication of a mixer unit can be divided into four steps. The first step is the fabrication of the device. The second and third steps are mixer block and feedhorn/ clamp fabrications. The fourth step is the mounting of all separated parts.

### 3.2.1 Devices

The device fabrication in the clean room facilities for all presented mixers is done by Karl Jacobs and Patrick Pütz. The mixer devices for upGREAT mixers consist of several thin film layers which are deposited on a Silicon (Si) on insulator (SOI) wafer. A SOI wafer consists of a 300  $\mu\text{m}$  thick Si wafer with on a thin  $\text{SiO}_2$  layer on top on which a 2  $\mu\text{m}$  (stress free) high resistivity Si layer is deposited. These wafers are necessary to fabricate a device on a thin Si membrane substrate [22] [58] [59].

High resistivity Si has the advantage of low losses at THz frequencies [60]. A measured transmission of a thick 531  $\mu\text{m}$  high resistivity Si wafer shows no significant transmission losses between 1 - 6 THz (see Fig. 24) [61]. The transmission of the Si wafer is measured with a FTS (see Sec. 5.2). The periodically frequency dependent transmission of the thick Si substrate originating from reflections. We assume that the losses are even lower at cryogenic temperatures. By reducing the temperature less charge carriers are available to couple to the radiation.

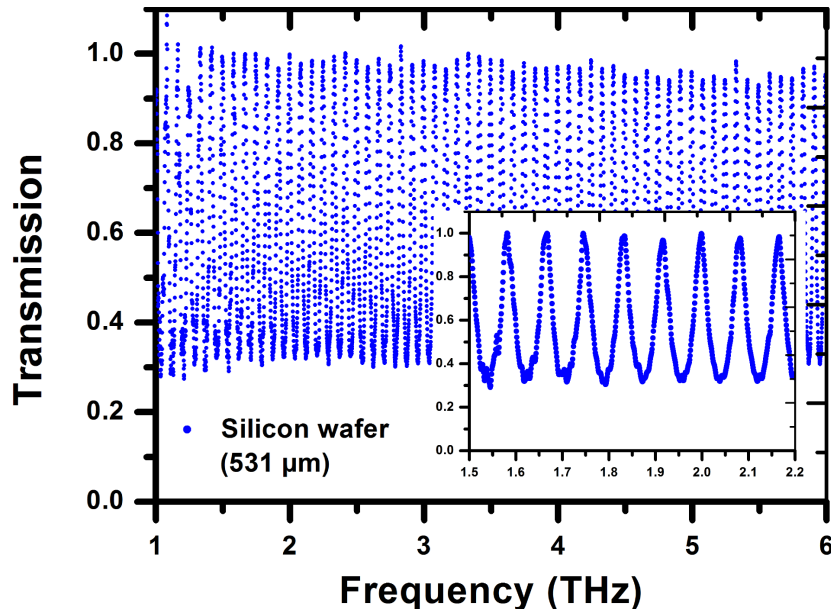


**Figure 24:** Transmission of a 531  $\mu\text{m}$  thick silicon wafer measured with a Fourier Transform Spectrometer (see Sec. 5.2) between 1 - 6 THz. Inset shows a zoom in in the frequency range of 1.5 - 2.2 THz. [61]

The wafers have a diameter of 3 inches (resulting in a 3 cm x 3 cm chip). One wafer is divided into 20 sectors (A, B, C, ..., T) with devices and 6 sectors for layer tests of gold see Fig. 25. The four point test structures for the Au thin film layers made of different single gold layers are of the circuit layers. The structures with the shape of a square and a long line can be used for measuring of the conductivity of the pure gold layer (see Fig. 25).

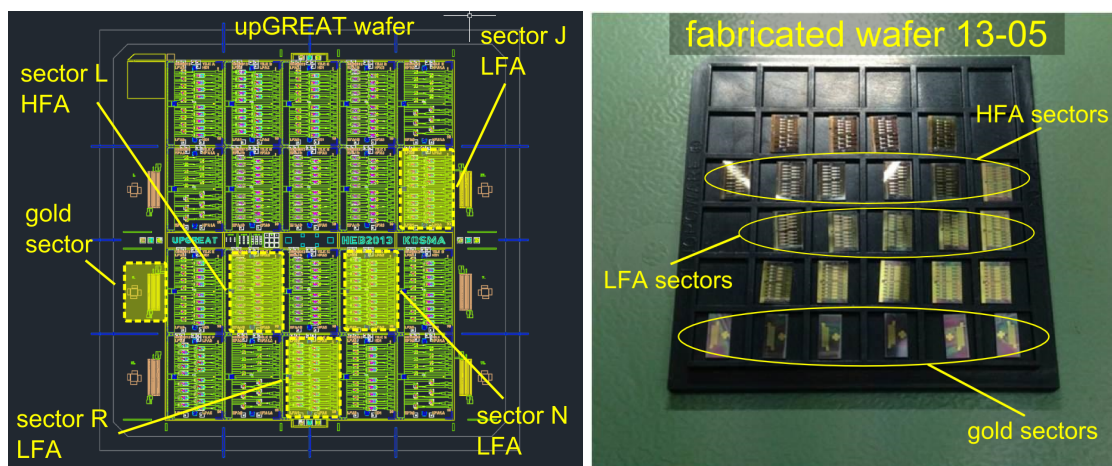


**Figure 25:** Left: mas of the upGREAT wafer with highlighted sectors which are used for the mixers. Right: image of separated sectors from a manufactured wafer.

The wafer consists of several designs for different frequencies. The main designs are LFA1/LFA2 (sectors B/J/N/P/R) and the HFA-1b / HFA-3 (sectors D/G/H/I/L/M) are used for the GREAT and upGREAT instruments. The wafers are processed at the front and back side [58]. On the front side, the HEB and the planar circuit have to be defined (see [22]). On the backside of the wafer, the insulator is etched away and cut into separate sectors.

After device fabrication, the SOI wafer is diced into the separated sectors. At this stage, I measured the devices for the first time with DC characterization. The results of the measurements for several parts are shown in a later Sec. 6.1.1 and 6.4.1. After the characterization of the sectors the ones with the best performance (highest  $T_c$  and  $I_c$  with a good impedance matching) are chosen to continue for further processing to a HEB mixer. These sectors are then etched on the back side and separated into the single devices ready for mounting into the mixer block [22].

In Fig. 26 scanning electron microscopy (SEM) images for two designs LFA2 (top) and HFA-1b (bottom) are shown. A zoom in on the waveguide and a second zoom in on the NbN film show the details of the fabricated circuits.

Three wafers upGREAT13-05 (13-05), upGREAT14-08 (14-08) and upGREAT14-11 (14-11) are used for the characterization of the HEBs. After the first heterodyne measure-

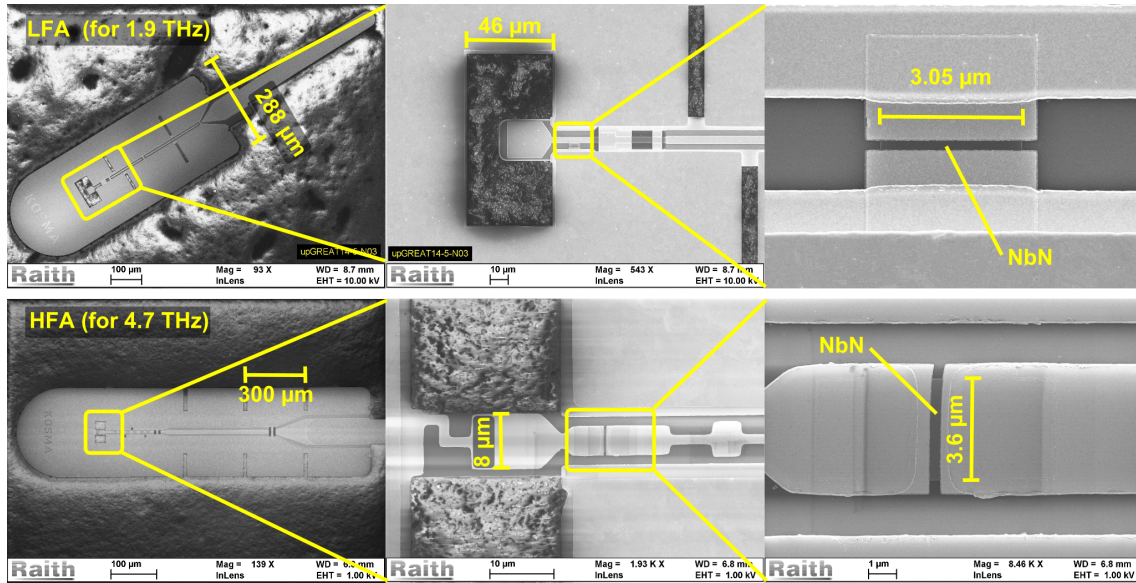


**Figure 26:** Scanning electron microscopy (SEM) images of a LFA 2 (top) and HFA-1b (bottom) devices. Left figure: device with the surrounding beam leads, middle figure: zoom on the probe in the waveguide and right figure: zoom on the HEB with Au contact pads [28].

ments of the wafer 13-05, I measured that the estimated required local oscillator power for optimal operation is too high for an array receiver due to the limited output power of the LO (see 7.1.3). In addition, both LFA designs also have a different power requirement due to the difference in film volume (about 30 %). The product of the volume and the critical current density is a good measure of  $P_{LO}$  [62].

The required LO power for the optimal operation was reduced for the new wafers. The change from the wafer 13-05 to 14-08 and 14-11 is mainly the reduction of the film volume by reducing the film thickness from 4.5 nm to 3.5 nm to reduce the LO power requirement. In addition, the length of the devices on 14-11 and 14-08 was reduced to 200 nm for wafer 14-11 and 14-08 compared to 300 nm for wafer 13-05. Both LFA designs are reduced to one design (LFA2) with the smaller width of 3.5  $\mu\text{m}$ . In addition, the number of devices that can be used is increased, which increases the probability to have similar devices with good performance for an array and to replace devices (more details see 3.2).

### 3.2.2 Mixer Blocks

A mixer block is used to mount the device, horn-clamp and the IF output components. The mixer blocks are made of oxygen free copper tellurium alloy (CuTe) with a footprint of 17 mm x 17 mm and height of about 15 mm. This material combination has the advantage of a good thermal heat conductivity and is hard enough for manufacturing structures of a few

**Table 4:** Table of the waveguide and substrate channel dimension and their tolerances. x is the larger and y the smaller length of a rectangular shape. The tolerances restrict the variation in power coupling to less than 5 %.

desgin	waveguide x ( $\mu\text{m}$ )	waveguide y ( $\mu\text{m}$ )	depth ( $\mu\text{m}$ )	channel x ( $\mu\text{mm}$ )	channel y ( $\mu\text{m}$ )	depth ( $\mu\text{m}$ )
LFA	96	48	26	188	30	10
tolerances	$\pm 5$	$\pm 5$	$\pm 5$	+7/-0	+0/-10	+4/-0
HFA	48	24	22	106	14	4
tolerances	$\pm 3$	$\pm 2$	$\pm 2$	+0/-5	+2/-0	+2/-0

$\mu\text{m}$  into metal with sharp edges without burrs. These structures are the critical part of the block. They consist of the waveguide cavity and substrate channel, which are manufactured by direct metal machining on a precision CNC [63]. The blocks are manufactured in our workshop which has experience based on the GREAT single mixers [58]. A stamping tool of hardened steel is also fabricated in-house to be able to achieve a precision of  $1 \mu\text{m}$  for the stamped dimension of this structure. The structures are manufactured in series of stamping and milling sequences of the block (See Fig. 27).

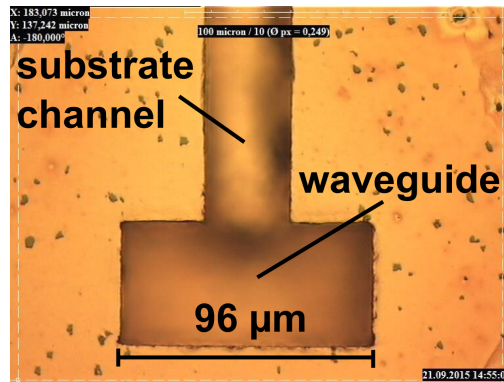


**Figure 27:** Waveguide ( $96 \mu\text{m} \times 46 \mu\text{m}$ ) and substrate channel (width  $30 \mu\text{m}$ ) stamped into a LFA mixer block. The block is fabricated in the workshop.

This procedure prevents the increases of burrs, which is an issue for a flat mounting of the device into the block. This flatness is important for a good coupling of the signal and reduces the stress on the thin device which is pressed with the horn-clamp. The waveguide and the device channel dimensions for the different designs are listed in Tab. 4.

Each mixer unit has to be checked for the tolerances which are determined by the CST simulations for the waveguide and device channel. In addition to the mechanical tolerances, the demands for mounting of the device have to be fulfilled. Furthermore, the residual particles in the waveguide have to be removed from a substrate channel. At the end of the

substrate channel, a second wider channel is milled into the block for the IF signal line. Beyond that, a recess for an IF board is milled into the block. This board contains just a line with an impedance of 50 Ohm. The output line board is used to reduce strain from the connector to the device during the thermal cycling and for broadening the IF output line. For the connector, a hole is milled perpendicular to the plane of the circuit board, through the block. A SMA connector is used for the connection to the IF-output.

In Fig. 28 a set of LFA mixer blocks is shown. A zoom into the stamped waveguide at the substrate channel shows the sharp edges of the high precision structures with flat back-short.

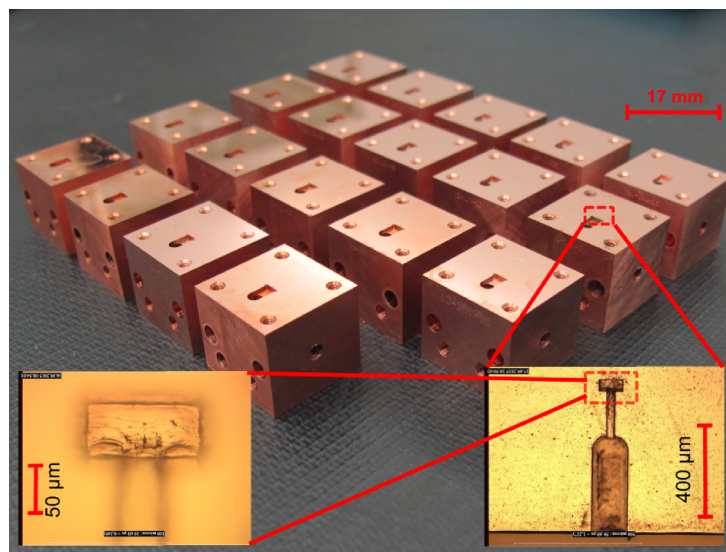


**Figure 28:** 19 mixer blocks for LFA mixers fabricated in the workshop. A zoom in, with a magnification of 500, to the location of the device is shown in the lower right inset. A further zoom in, with a magnification 1000, to the back-short of the waveguide is shown in the lower left inset.

### 3.2.3 Horn-Clamp

The optical interface between the waveguide to the receiver optics is a feedhorn. This feedhorn consists of an extension of the waveguide from the block with a transition from the rectangular to a circular end of the horn (see Fig. 29). It is a smooth-walled spline profile horn [64]. The design is based on the horns of the GREAT mixer for 1.9 THz [21]. This type of horn is adapted for LFA mixers to have a broad RF band coupling up to 2.5 THz.

In addition, horns are scaled to 4.7 THz for the H-channel and HFA. The optimization for the bandwidth, the cross polarization characteristics and the manufacturing are done by Radiometer Physics GmbH [65]. The feedhorn consists of copper with a thin gold layer on the copper surface. After delivery of the horns, each horn has to be verified in a similar way as the mixer blocks when all critical dimensions are in specified tolerances.

Then each signal horn has to be manufactured and press-fit into a horn-clamp fabricated in our the workshop. This clamp is necessary to assemble the horn by the alignment of the waveguides in to of each other and for clamping the horn on the mixer block. The clamps are made from Aluminum because it has a larger coefficient of thermal expansion as copper. During the cool down, the feedhorn will be compressed by the aluminum clamp. It can be easily machined (instead of copper or steel). A LFA feedhorn and a clamp are shown in Fig. 29. The mixer can now be assembled in one unit.

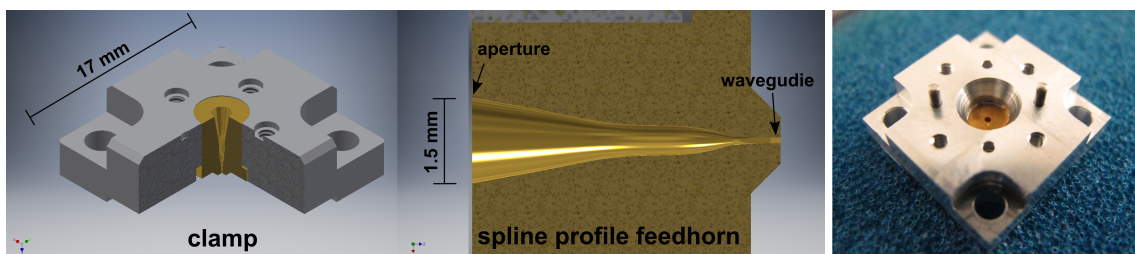


**Figure 29:** The left figure represents a 3D model with a cut through the center of the horn-clamp. In the center the horn profile is shown as cut of the 3D model [65]. The right a photo of a feedhorn press-fit into a horn-clamp. The aperture of the profile is the small hole in the center of the horn-clamp.

### 3.2.4 Mixer Assembly

The final step of the mixer fabrication is assembling the separate units together, which is done by Micheal Schultz. The devices are assembled on top of the waveguide with a hexapod micro-manipulator with an accuracy of  $0.2 \mu\text{m}$ . The micro-manipulator allows a mounting of the device in respect to the waveguide of the mixer block with precision of  $< 1 \mu\text{m}$ . First, the IF-DC board which, is an output line on a  $530 \mu\text{m}$  thick Si substrate with an impedance of 50 Ohm, has to be glued on the mixer block. Then the IF-DC board is connected by wire bonds to the SMA output connector (see Fig. 30) which is connected to a load, to prevent electrostatic damage.

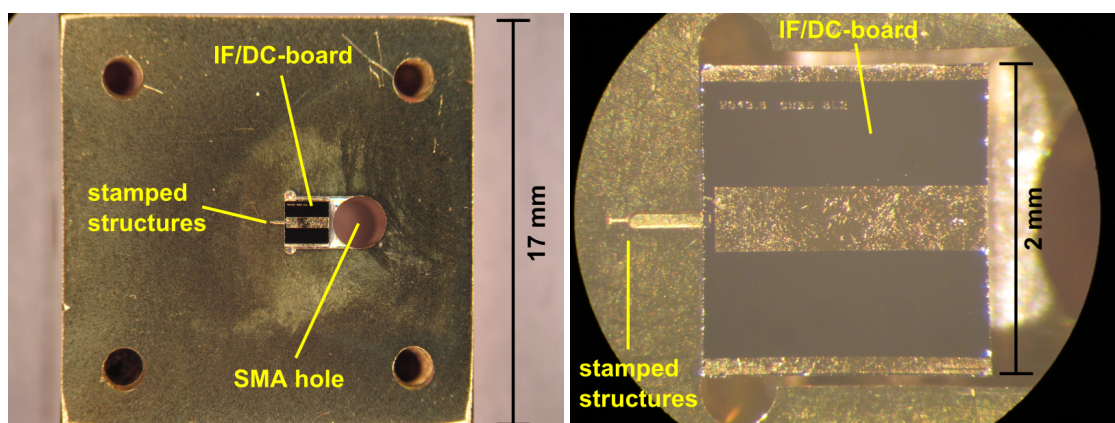


**Figure 30:** IF/DC board mounted into the mixer block.

The advantage of the IF-DC board is the separation of the device from a momentum, on the SMA inner connection during screwing of the IF connector. Then device mounting has to be done, which is the most critical part of the entire process. Three main issues that might occur during assembly, which could be a reason for a later poor performance: the device position tolerances in the waveguide have to be less than  $1 \mu\text{m}$  (for 4.7 THz), electrostatic discharges could damage the NbN film and mechanical failures (crack of the device, loss bonds). The device is first aligned to waveguide via an optical microscope. For the ground connection of the circuit, the beam-leads are connected by ultrasonic tab bonds to the mixer block. The IF output line at the end of the device is bonded to an IF/DC board (see Fig 31).

At this stage of the mixer block assembly, the DC characteristics can be measured to monitor the superconducting properties of the device. Then the normal state resistance ( $R_n$ ), the shape of the DC-IV curve at 4 K and the superconducting properties  $T_c$  and  $I_c$  are the expected range the mixer can be further assembled. Otherwise, the device has to be removed and replaced by another device.

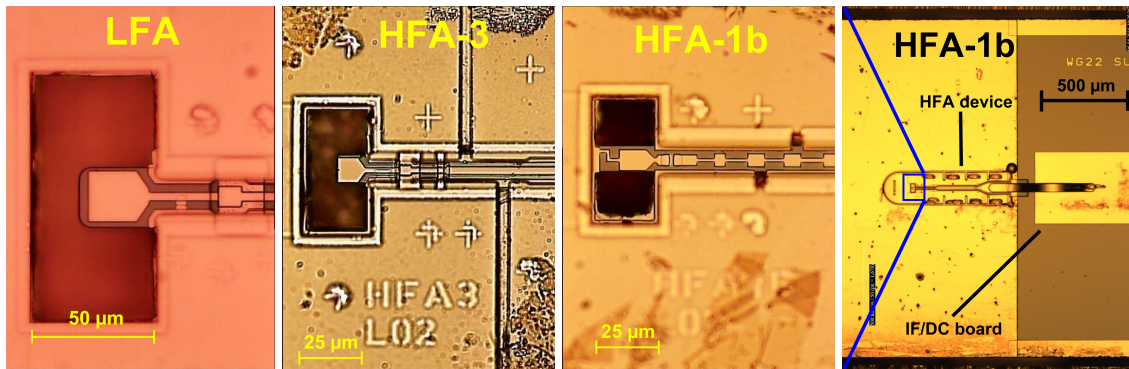


**Figure 31:** Microscope images of assembled devices. From Left to right: LFA, HFA-3 and HFA-1b mounted devices and a zoom out from device HFA-1b to top of the mixer block with IF-DC board.

After this step, the horn-clamp can be assembled on the block. Similar to the device the horn clamp is optical aligned by a microscope. The clamp is handled with a dedicated tool to avoid displacement or rotation with respect to each other. The clamp is then fixed with four M2 screws. This procedure is done during observing the waveguide alignment. A complete assembled LFA mixer block with a view into the feedhorn where the device can be seen at the end of the waveguide is shown in Fig. 32.

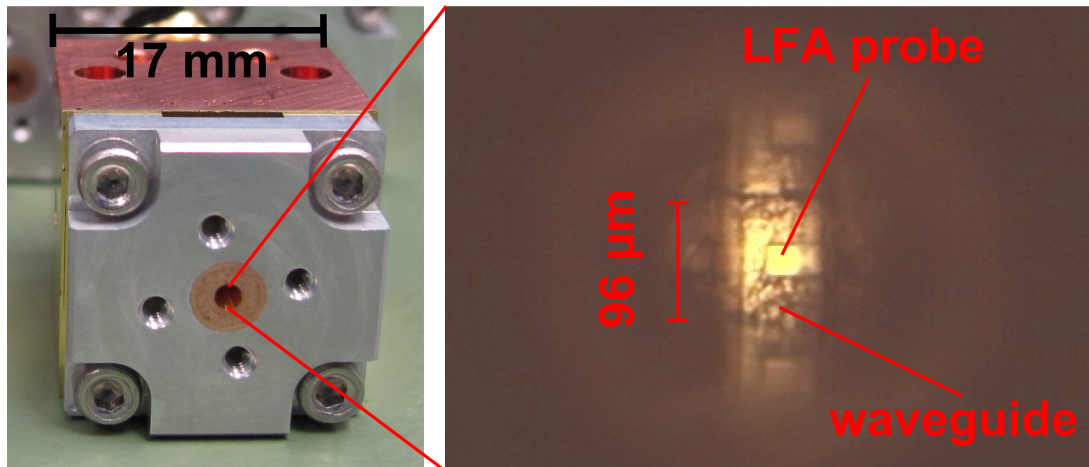


**Figure 32:** Assembled mixer block on the left side and on the right side a view of the probe antenna looking through the feedhorn.

## 4 Heterodyne Measurement Setup at 1.9 to 4.7 THz

A significant part of this thesis was the development of a stable and reliable setup for the characterization of the mixers for the LFA mixers. The input signal of a mixer is called Radio Frequency (RF) and the output Intermediate Frequency (IF). The heterodyne setup for the measurements at 1.9 THz consists of several components that can be subdivided in the RF section which operates at THz frequencies and the IF section that operates at GHz frequencies. A schematic of the setup is shown in Fig. 33 and in the Fig. 34 where both parts of the setup are highlighted. Both parts of the setup, especially for the RF setup for 1.9 THz for the LFA mixer characterization, are presented in this section.

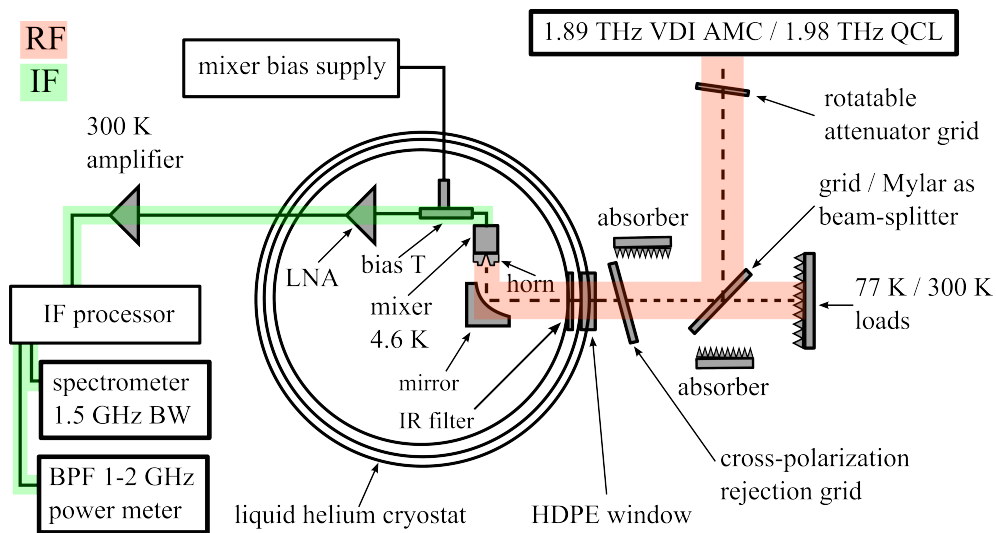


**Figure 33:** Schema of the 1.9 THz heterodyne setup. Red lines visualize is the RF path and green is the IF signal of the receiver.

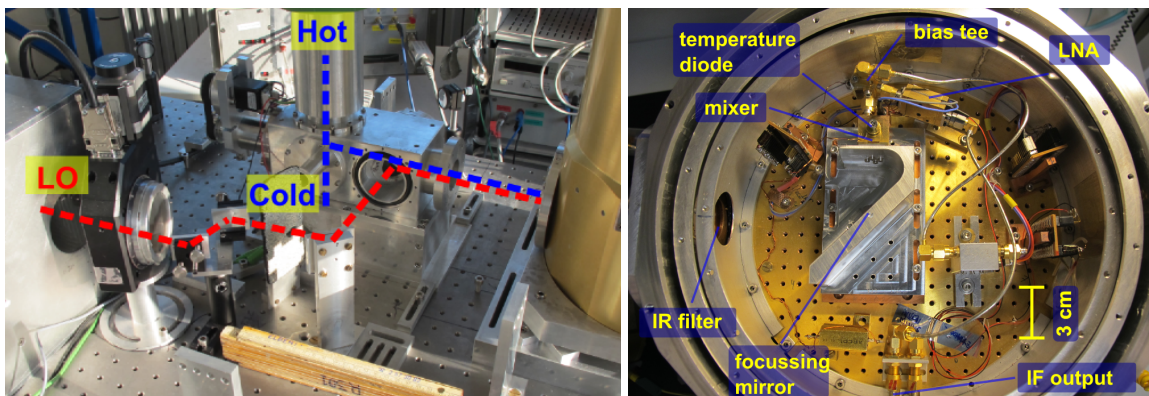


**Figure 34:** Images of the 1.9 THz heterodyne setup. Red lines visualize is the RF path and green is the IF signal of the receiver. Left photo of the setup with indicated beam paths of the LO and the THz calibration source of the Hot/cold load to the dewar. Right photos of the open dewar with the cold optics and IF components.

## 4.1 Radio Frequency Setup for the Operation at 1.9 THz

The Radio Frequency (RF) part of the receiver system consists of the local oscillator source, the THz calibration sources, the optical interface and the mixer. The optical coupling of the radiation was calculated with the Gaussian beam optics [66] by Netty Honingh.

Depending of the application and operation frequency different types of local oscillators are used like gun-oscillators, commercial Amplifier Multiplier Chains (AMC), gas lasers or novel quantum cascade lasers (QCL) [67]. The Local Oscillator (LO) source for the 1.9 THz receiver is an AMC (from VDI [68]) which multiplies the output signal at 13.125 GHz of a synthesizer by a factor of 144 to 1890 GHz LO output. During the measurements, the LO is constantly set to maximum output power. For the optimum adjustment of the LO-power incident on the mixer, a rotatable wire grid is used to attenuate the LO. The LO beam is guided with two flat adjustment mirrors on focusing mirror, which focus the LO radiation to the center of the beamsplitter (BS). The THz calibration sources in the setup consist of two blackbody microwave absorbers, one at room temperature ( $\sim 295$  K) and one cooled down to 77 K by immersing it in liquid nitrogen which is reflected by a flat mirror to the BS. The THz calibration source and the LO radiation are combined, either with a thin dielectric foil (e.g. 12 or 23  $\mu\text{m}$ ) or with a wire grid as a BS. The calibration sources radiation is coupled in transmission through the BS and the LO in reflection to the dewar. A radiation splitting factor of typically 90% calibration sources and 10% LO is chosen. From the BS the radiation is coupled to the dewar window.

The dewar window consists of a HDPE foil with a thickness of 370  $\mu\text{m}$  which was chosen for a high transmission of 1.9 THz and 4.7 THz. A low pass filter is used as an infrared shield for the unwanted external radiation [69]. The transmission of all used dielectric foils was measured at room temperature with a Fourier transform spectrometer (FTS, see 5.2). The transmission on the main LO test frequency of 1.89 THz and for both side bands of the mixer is about 0.94 for the IR filter and approximately 0.92 for the HDPE window (see Fig. 35).

Since most of the LO radiation is transmitted through the BS, an absorbing load must be installed as a beam dump. Else the significantly higher power of the LO can reflect back into the signal path and create strong standing waves. The LO power variation coupled to the mixer introduces a ripple in the IF band, which makes it more difficult to interpret the data. The ripple is particularly large when a wire grid is used as a beamsplitter (see Fig. 36). In this case, the LO signal incident on the mixer has a component that is orthogonal to the polarization of the mixer. This component is fully reflected at the mixer, and then again partly reflected at the BS grid. To avoid a standing wave a cross-polarization rejection wire

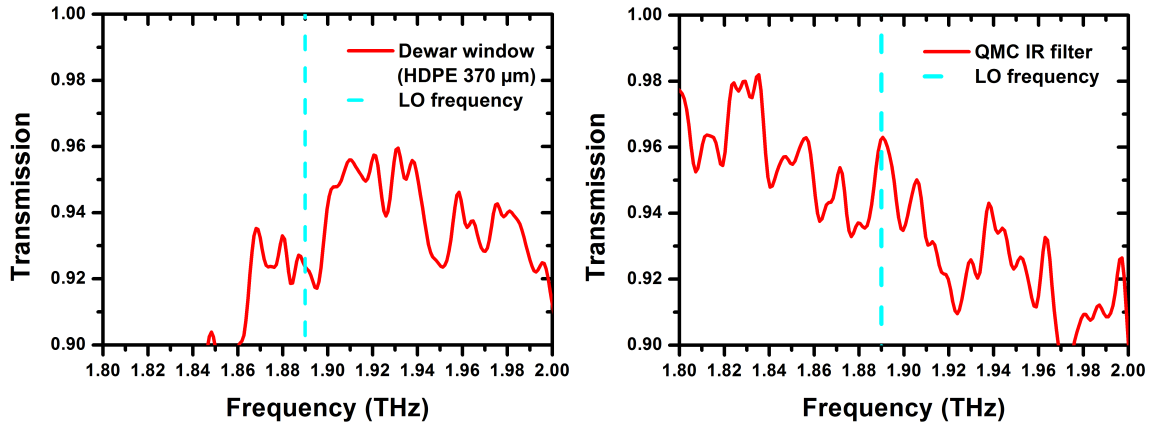


**Figure 35:** Left: THz transmission of 370  $\mu\text{m}$  HDPE foil measured with a FTS, right: THz transmission of IR filter measured with a FTS. Both measurements are done at room temperature in a evacuated compartment in a frequency range between 1.8 - 2.0 THz.

grid was added in front of the dewar window. The wires of the grid were set perpendicular to the electrical field of the waveguide to transmit the desired part of the LO signal. In addition, the grid was set under a tilt of 15  $^\circ$  to the optical axis. In this configuration, the undesired component of the LO was reflected out of the path between mixer and BS. The reflected LO signal is directly coupled on an absorber load.

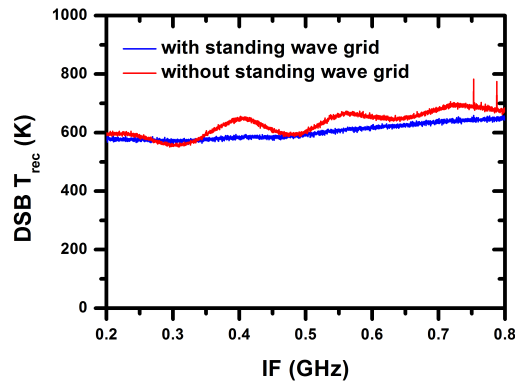


**Figure 36:** Comparison of the measured receiver noise temperature as a function of the IF between 0.2 - 0.8 GHz. The in first measurement in red no additional wire grid is set in front of the dewar. In the second measurement in blue a wire grid is set in front of the dewar. The grid removes all optical standing waves from the measured noise temperature.

The path from the loads to the dewar window ( $\sim 35$  cm) and the LO path ( $\sim 80$  cm) were under atmosphere. The transmission through the atmosphere leads to losses of the signals (transmission of about 0.9) which are discussed in Sec. 6.1.4. A final focusing mirror inside the dewar is mounted with the mixer on the cold plate (cooled with liquid Helium to about 4.5 K). The THz signals are focused to the feed horn and then coupled via the waveguide

transition to the waveguide probe of the device and absorbed by the HEB bridge. Here the LO and calibration signal are mixed and the signal is down converted to the intermediate frequency (IF). The IF Signal is coupled out of the mixer via a low-pass filter integrated in the device connected to the center conductor of a SMA connector which is the starting point of the IF output chain.

## **4.2 IF Setup at 0.2 to 5 GHz for the 1.9 THz Measurements**

From the Intermediate Frequency (IF) output of the mixer the IF is guided to an external bias tee (bias T) see Fig. 34. The bias tee is a three-port network with a DC bias input, IF output and IF input/DC output port. The DC bias is coupled to the mixer without disturbing the IF signal guided out of the IF port.

The first amplification of the IF signal is done with a cryogenic Low Noise Amplifier (LNA, [70]) with a bandwidth of 0.2 - 5 GHz a return loss of less than 10 dB and a gain of about +30 dB. After the LNA the signal is coupled out of the dewar to 295 K. A second warm LNA with a gain of +46 dB further amplifies the IF-signal before it is coupled to the IF-box see Fig. 37. I developed and build the IF box for the operation with an AFFTS which is discussed in next sections and in Sec. 5.4.3.

### **4.2.1 Intermediate Frequency-Box**

The IF signals have to be amplified to match the right level for the signal processors which follow the IF-box. For that purpose, an amplifier and attenuator chain is required. In addition, with internal mixers are used for mixing a bandwidth of 1.5 GHz from a higher center frequency to an IF lower one (see Fig. 37). This mixing step of IF signal is necessary to reconstruct the mixer IF bandwidth which is discussed in Sec. 4.2.2. In this thesis, I did the development, the construction and test of IF box. In addition, the software for the measurement setup was adapted.

Inside the IF-box the signal is first amplified by an amplifier (ZVA1 [71]) with a bandwidth of 0.7 - 18 GHz with a gain of +26 dB. Switch 1 (SW1) defines the mixing path and the direct path (see Fig. 37). In the direct path the signal is directly guided to switch 2 (SW2). Otherwise, the signal has to follow the mixer path (Sec. 4.2.2) before it is guided back to switch 2. Next, the signal is amplified using an amplifier with a bandwidth of 0.1 - 18 GHz (ZVA3 [71]) and a gain of +26 dB. Next the IF power level is optimized with a variable attenuator to -15 to 0 dB. A third switch (SW3) is used to provide six different output options for the IF box. The LPF1 output port has a Low Pass Filter (LPF) with a frequency of 1.45 GHz. The LPF2 output port has a LPF with a frequency of 2.35 GHz and



can be used for a spectrometer with 2.5 GHz bandwidth. Furthermore, the YIG-filter output port with a Yttrium Iron Garnet filter (YIG) which was a tunable Band Pass Filter (BPF) with a bandwidth of 15 MHz was available.

The YIG filter and the Power meter output of the IF box base on one a switch position which was later divided. First a BPF between 1 - 2 GHz and then a DC isolator was used. Behind the DC isolator the IF was spitted with a -10 dB coupler into two signals. The -10 dB signal is detected with a DC power detector and then amplified by a DC amplifier before the DC detector signal was coupled out of the IF box. The second output of the coupler was coupled as an output port for a power meter. The direct output of the IF-box is used without any filter. The 1.44 GHz LPF and the power-meter output were mainly used for the characterizations of the mixers. The frequency dependent sensitivity of the IF box is impart of the calibration of the receiver setup. The measurement results are shown in Sec. 6.1.7.

#### 4.2.2 The Mixing Path

Due to the limited bandwidth of 1.5 GHz of the Digital Fourier-Transform (DFT) spectrometer, the IF band had to be cut in different bands (see Sec. 5.4.3). Those bands have to combine to able to reconstruct the mixer bandwidth which is in the range of 3.0 - 4.5 GHz. I decided to measure the complete IF band in four overlapping bands a - d (see Tab. 5).

band	IF-box input (GHz)	LO 1 (GHz)	LO 2 (GHz)	output IF (GHz)
band a	0.2 - 1.5	-	-	0.2 - 1.5
band b	1.2 - 2.7	8.9	7.7	0.0 - 1.5
band c	2.4 - 3.9	10.1	7.7	0.0 - 1.5
band d	3.6 - 5.1	11.3	7.7	0.0 - 1.5

**Table 5:** IF band spit into four bands a-d. LO 1 and LO 2 frequencies configurations for all different bands.

For band a, the signal can bypass the mixer path as it already is at baseband. The other bands b-d have to process in the mixing path.

At the mixing path, the signal has to converted at mixer 1 to higher frequencies with a synthesized signal from LO 1. The LO 1 frequency is depended on the choice of the IF band. The mixed signal was then filtered with a bandpass filter (BPF) between 5 - 7.5 GHz to remove all unwanted mixing products and remains of LO1. An additional amplifier (ZVA3 [71]) with a gain of +26 dB is necessary to provide enough signal for the second mixing step where the signal was down converted again. This filtered signal was mixed with a second synthesizer signal from LO 2 at mixer 2 down to 0 - 1.5 GHz. Then it was coupled

to switch 2. After switch 2 the IF chain is the same for all bands.

After the main part of the measurements were done two eXtended bandwidth FFTS (XFFTS [72]) with a bandwidth of 2.5 GHz IF-box were added to the setup. Due to this change and a need of an additional calibration measurement an adjusted version of the IF-box were used to calibrate the main version by a mixer calibrated in both setups.

### 4.3 4.7 THz Single Pixel Receiver

During the first tests of the 4.7 THz single pixel no local oscillator operation was available at 4.7 THz in Cologne. So heterodyne measurements were only possible in a collaboration with the MPI in Bonn [22]. A schematic diagram of the receiver is shown in Fig. 38. The cold load here is cooled by a cryocooler to a physical temperature of 130 K. The beamsplitter in this configuration is a 3  $\mu\text{m}$  Mylar foil. The transmission of this foil at the frequency of interest is 0.835. The optical compartment is evacuated to a pressure of  $10^{-2}$  mbar. The LO is a Quantum cascade Laser (QCL) developed by Richter et al. with an output power of 150  $\mu\text{W}$  and a frequency range of approximately +2 to -4 GHz around the oxygen line [20].

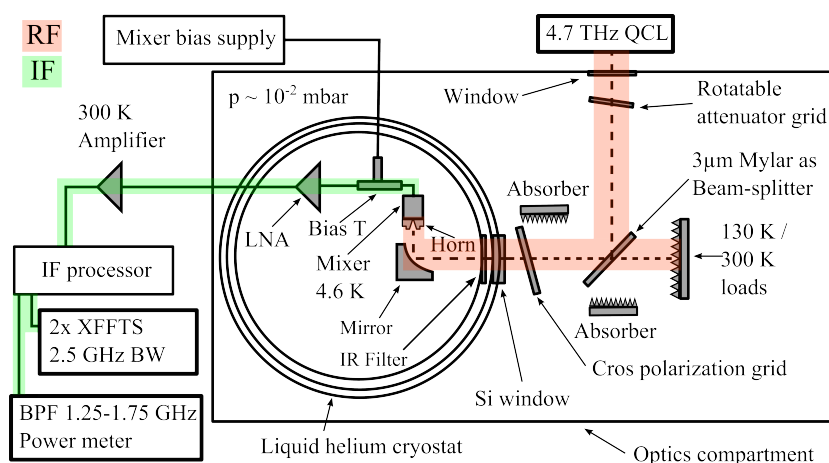


**Figure 38:** Scheme of the Heterodyne receiver setup for 4.7 THz at the MPI in Bonn. RF part red area and IF part green area.

### 4.4 Differences to the GREAT Receiver Channels

The main difference of the upGREAT receiver system to the heterodyne measurements was the operation of 14 mixers in an array. In the heterodyne measurements only one single mixer is measured. The signal paths were evacuated for the GREAT receiver channels. An evacuated path leads to higher transmission of the signal and thus better calibration due to well-established brightness temperatures of the hot and cold load. The receiver then

operates under more stable conditions and reaches a lower noise temperature. In addition, it increases the amount of available LO power per device which is crucial in the THz range due to reduced losses in the optical path. The upGREAT LFA setup consists of two parts, one for each sub-array. Each sub-array consists of 7 mixers which are fed by a one LO unit. The LO and sky signal are combined with a beamsplitter and then divided into seven beams by a phase grating. The phase grating divides the power equally for each mixer. This beam bundle is then coupled into the dewar to the mixers [24] [19]. In addition GREAT and upGREAT use DFTS spectrometers with a bandwidth of 2.5 GHz (FFTS [72]). The spectrometers were upgraded to XFFTS spectrometers with a bandwidth of 4.0 GHz.

## 5 Measurement Methods for HEB Mixer Characterization

The measuring methods which were used to characterize the mixer are listed in the following sections. These characterizations can be split in the DC and the RF/IF parts where the different methods are used. In Sec. 5.1, the DC characterization with the IV and RT curves are presented followed by the measured method of the broadband RF response in Sec. 5.2. The noise temperature is measured with the following methods: 1.) spectral intermediate frequency response (see Sec. 5.4.3), 2.) local oscillator power sweep (see Sec. 5.4.2) and 3.) Voltage sweep (see Sec. 5.4.1). Furthermore, the two methods of the determination of the required local oscillator power are shown in Sec. 5.3. The LO power is either determined by the incident coupled LO power or by the isothermal lines method.

### 5.1 DC Characterization

The DC characteristics of a HEB micro-bridge are the current-voltage (I-V) characteristic and the resistance versus temperature (R-T) dependency. The HEBs are measured with a dipstick in a liquid helium by immersing the device, and in the case of the R-T measurement, slowly pulling it up.

After the final fabrication steps, the devices are separated and then integrated into the mixer block. At this stage, the measurements of the DC properties are repeated to see if there were any changes due to the last fabrication and mounting steps. The characterization was either done with a different dipstick where the assembled mixer can be mounted on or inside a dewar on a cold plate.

For the I-V measurements a DC bias supply is used as a constant current source that can be swept from a voltage of -50 mV to +50 mV. The voltage is set as a bias and the current and the voltage are recorded using a four-point measurement scheme.

The R-T dependency is measured with a calibrated temperature diode between room temp and 4 K (between 25 K and 4.2 K on the cold plate). The R-T measurements of the DC characteristics are performed using a dual lock-in amplifier setup, one for the voltage and one for the current [73]. A small current modulation of typically 1 or 10  $\mu\text{A}$  is used, to measure the device resistance within a temperature range of 4.2 K and about 25 K (maximum resistance of the NbN HEB). The critical current ( $I_c$ ) and the critical temperature ( $T_c$ ) can be taken from the measured data (see 2.3.3).

## 5.2 Broadband RF Characterization

The bolometric direct-detection response of the HEB microbridge can be used as a tool for the characterization of the broadband RF response. In the direct detection mode, the bath temperature of the HEB mixer is increased until the DC I-V curve has approximately the same heating level as an optimum operation level using a LO. The voltage bias is typically set to the identically value as for optimum heterodyne response. The response can be measured with a Fourier transform spectrometer (FTS) by Bruker [74] (FTS model IVS 66v/S). A FTS consists of a Michelson interferometer and a mercury lamp which behaves as a broadband THz source. The Michelson interferometer consists of two mirrors whereas one mirror is fixed and the other one is movable [66]. By the variation of the distance of the mirror to the beamsplitter, an interference pattern is produced which is measured by the HEB as a variation of the DC bias voltage when the HEB is current biased. By Fourier transformation of the interference pattern the response as a function of the frequency can be calculated. The absolute height of the recorded FTS spectrum for each mixer depends on the bias conditions of the HEB (voltage and temperature), the gain settings of the DC amplifiers in the FTS and the bias box. These are the reasons why the measured response is not a good indication of total spectral response. The internal FTS spectral transfer function (optics inclusive beamsplitter, frequency resolution) can be calibrated with an empty "background" measurement using the FTS internal DTGS detector circuit. In contrast, the measured frequency response of the mixer in direct-detection mode is not affected by the HEB bias conditions for the range of interest. The suitably scaled measured frequency response can be directly compared the with expected spectral power coupling ( $S_{21}$ )<sup>2</sup> as calculated by the circuit simulator CST Microwave Studio [56]. A typical mixer and calibration measurement of the FTS is shown in Fig. 39. The FTS with the DTGS detector is used to characterize windows, filters and other optical components.

## 5.3 Local Oscillator Power Requirement

A reliable estimate of the local oscillator power ( $P_{LO}$ ) which is required to operate a mixer is very important for building an array receiver. A typical approach for a heterodyne array receiver is to use one local oscillator (LO) source for several mixers. In this case, the system is less complex and require significantly less space by using only one LO unit. The LO beam has to be divided in the optics into separated beams with equal divided power. Each mixer should have than the same power requirement. Otherwise, the LO power of each mixer inside the array has to be adjusted individually, which increase significantly the complexity of the receiver.

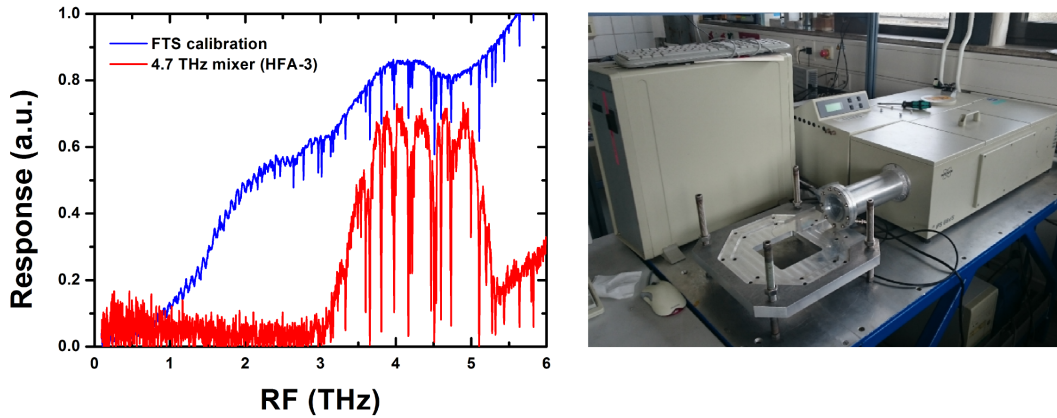


**Figure 39:** Left: the measured response of an empty FTS recorded with of the internal DGTS detector (blue data set) as the background for calibration. The response of a 4.7 THz mixer of the HFA-3 design measured as a function of frequency (red data set). Right: image of the FTS in the laboratory.

For the characterization of a single mixer a reference source which is in our case a Virginia Diodes (VDI) Amplifiers Multiplier Chain (AMC) [68] for the determination of the requirement  $P_{LO}$  is used. At the operating frequency of 1.89 THz (maximum output power of the AMC) the output power of the LO is  $21.4 \mu\text{W} \pm 0.4 \mu\text{W}$  given by the specification from VDI. For the estimate of the required  $P_{LO}$ , we determine the incident  $P_{LO}$  in front of the feed horn inside the dewar. The electric field of the LO and the mixer waveguide are set to be parallel and in the horizontal polarization. The incident  $P_{LO}$  is then dependent on the angle of an attenuator wire grid in the optical path of the output of the LO (see Fig. 40).

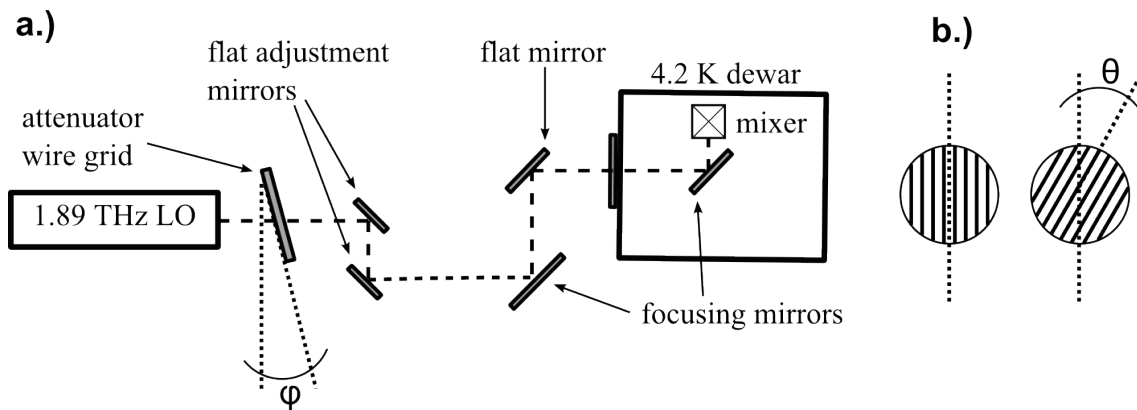


**Figure 40:** a.) LO signal path from LO to the HEB dewar b.) Wire grid angle  $\Theta$  definition (signal path through the plane).

The LO has a diagonal horn designed for a center frequency of 1.9 THz. The wire grid provides attenuation of the Gaussian beam via a computerized rotational stage. The grid plane is tilted by an angle  $\phi$  of 15 degree relative to the incident plane (see Fig. 40). This

tilt avoids multiple reflections in the optics, which can cause standing waves. The rotational angle of the grid  $\Theta$  is measured in the plane of the grid. The transmission through the grid is given by the projection of the grid plane to the incident plane. This leads to an effective angle  $\Theta_e$  giving by [66]

$$\Theta_e = \arctan(\tan(\Theta) \cdot \cos(\varphi)). \quad (35)$$

The angle difference from  $\Theta$  to  $\Theta_e$  due to the tilt is 0.5 - 1 degree. The available  $P_{LO}$  is reduced by this tilt at maximum by 10 %. Behind the grid three adjustable flat mirrors are used for alignment. The two focusing mirrors are necessary to collimate the beam and to optimized beam waist position. In front of the dewar the beamsplitter was replaced by a flat mirror to have maximum LO power coupling to the mixer. The beam has to be transmitted through the HDPE window with a transmission of 92 % and the IR filter with a transmission of 94 %. At last the beam is focused to the mixer feed-horn with an elliptical mirror. I neglected the losses from the flat and focusing mirrors and assume to have an equal atmospheric absorption for each measurement. The transmission for the in air path of about 80 cm are estimated for the conditions of a humidity of 50 % of about 80 cm path is approximately 0.84 %. It is based on extrapolation of a measurement with the THz Time Domain Spectroscopy (THz-TDS) by [75]. All devices are measured at a bath temperature of 4.5 K (+/- 0.2 K). The bias conditions are set to the point of optimum performance (low noise temperature) at a voltage of 1.0 – 1.5 mV. The setup was unchanged for all measured devices to have a comparable power estimate.

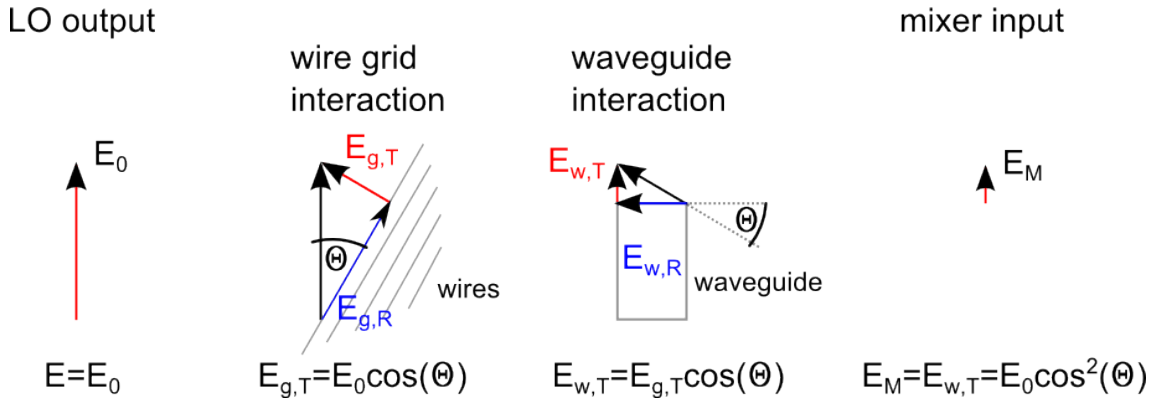


**Figure 41:** Change of the electric field vector due to interaction with the wire grid and the waveguide. The electrical field of the LO and the waveguide is set parallel.

The incident LO power is determined by the grid angles and the waveguide polarization. The electric field of the LO source ( $E_0$ ) has to couple to the wire grid attenuator (see Fig. 41). Here only the field which is perpendicular to the grid wires  $E_{g,T}$  is transmitted to the grid.

Then at the waveguide only the field which is parallel to the short side of the waveguide  $E_{w,T}$  transmitted to the waveguide. Here the field is given by  $E_M = E_0 \cdot \cos^2(\Theta)$ . The transition of the LO signal is given by

$$T = E_M^2 = E_0^2 \cdot \cos^4(\Theta). \quad (36)$$

Another approach is the determination of the absorbed  $P_{LO}$  by the so called isothermal technique [76]. In the lumped element model it is assumed that the device heated up in the same way by  $P_{RF} = P_{LO} + P_{signal}$  and  $P_{DC}$  which is shown in heat balance equation 8. Here all incident  $P_{LO}$  absorbed by the device. The resistance of the film is supposed only depending on the temperature of the electrons which depend on the bath temperature and the incident radiation coupling to the HEB. By comparing two IV curves, with and without LO power radiation, with an isotherm as a straight line that crosses both curves in point p1 and p2, the amount of absorbed  $P_{LO}$  is then equal to the difference in power between the two points.

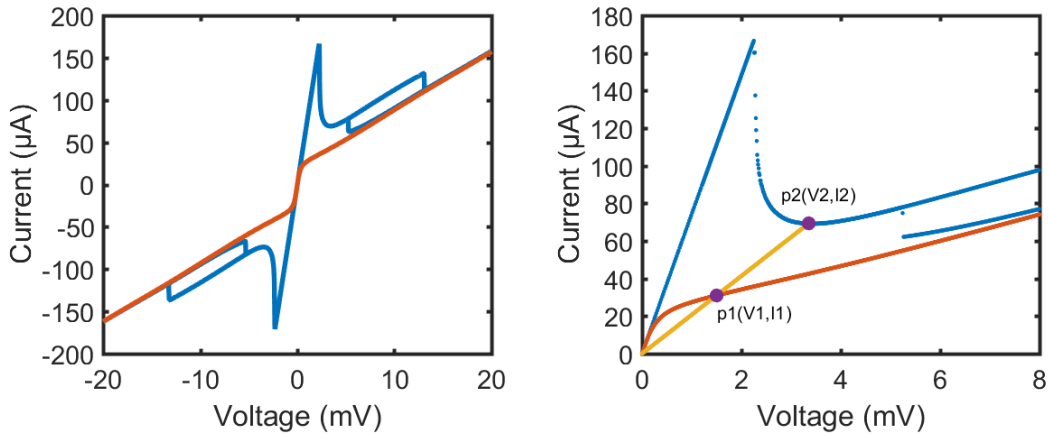


**Figure 42:** Left plot: measured DC-IV curve for device R06 (wafer 14-08) with and without LO radiating on the mixer. Right plot: zoom on the bias operation point p1 with a linear interpolation from zero to the IV curve without LO power to the cross point p2. The absorbed LO power is given by the difference in DC power.

For the calculation of the absorbed power of this method the unpumped (no LO) and a pumped (with LO) DC current voltage (IC) curve have to be measured (for a typical DC-IV curves see Fig. 42). The isothermal line starting from zero and crossing the pumped IV curve at the operating point p1 ( $I_1, V_1$ ) [76]. Further the line is extended to the cross point p2 ( $I_2, V_2$ ) to the unpumped IV. The absorbed power is then equal to difference in DC power from the point p1 to p2:

$$P_{LO,ISO} = (I_2 V_2 - I_1 V_1). \quad (37)$$

## 5.4 Heterodyne Measurements Methods

For the heterodyne measurements, I used three different methods to determine the dependency of the measured noise temperature ( $T_{rec}$ ) by three different parameters to determine to optimal operation conditions.  $T_{rec}$  for all methods is calculated with the Y-factor from Eq. 33. Each method delivers  $T_{rec}$  with a focus on a different property of the mixer. The voltage sweep is used to determine the optimal bias condition for the HEB mixer. The local oscillator power sweep is used for the determination of the optimal LO power and for the estimation of the change  $T_{rec}$  due to the direct detection effect. The spectral response is used to measure  $T_{rec}$  as a function of the intermediate frequency from 0 - 5 GHz.

### 5.4.1 Voltage Sweep

The Voltage Sweep (VS) method is based on a measurement with a power meter. The noise temperature is averaged over the IF band between 1 and 2 GHz by measuring the IF output power through a bandpass filter. The LO pumping level is fixed at optimal incident LO power and the voltage is swept over a range of -50 mV to +50 mV. Here the optimal bias voltage is between 0.5 - 2 mV for a typically measured HEB mixer (see Fig. 43).

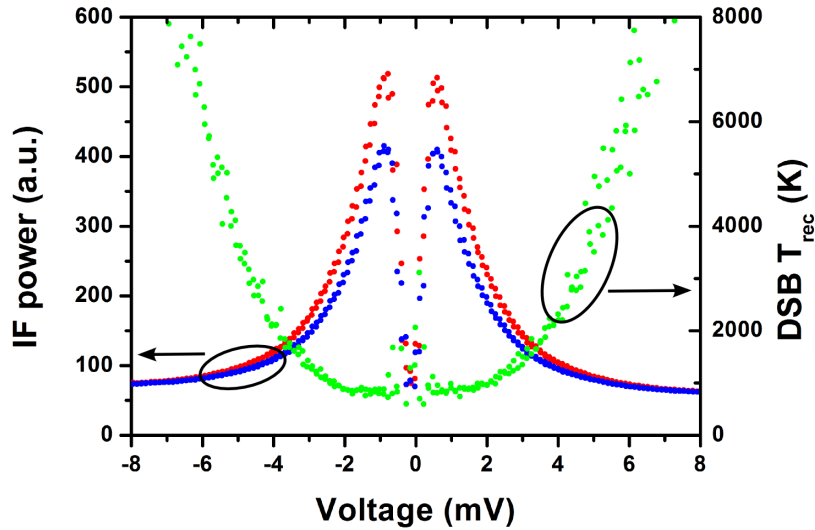


**Figure 43:** Voltage sweep: IF power measured as a function of the bias voltage for a hot load (red) and cold load (blue) on the left axis and on the right axis is in receiver noise temperature (green).

### 5.4.2 Local Oscillator Power Sweep

During the Local Oscillator Power Sweep (LOPS), the receiver average noise temperature is measured as a function of the amount of incident LO power ( $P_{LO}$ ) which is coupled to the

HEB [77]. The  $P_{LO}$  is varied by a rotating polarizer grid in front of the LO. It attenuates the linear polarized LO radiation depending on the angle of the grid wires with respect to the LO polarization. The detected IF power as a function of  $P_{LO}$  is measured by a power meter.

At a constant  $P_{LO}$  and fixed bias voltage, the current through the mixer changed by modification of the input signal from hot to cold load due to the direct detection effect (see Sec. 2.4.1). The current change leads in Eq. 11 to a modification of the mixer gain between the measurement of the hot and cold load which is followed by an increase of  $T_{rec}$ .

To determine  $T_{rec}$  without the direct detection effects, the output power for the hot and cold load have to be used for the same bias current. The measured hot and cold load input calibration signals as a function of the bias current are used for a polynomial interpolation (polynomial of the 10th order). This interpolation is used to calculate the Y-factor from Eq. 33 at the same bias current. The calculated  $T_{rec}$  is not influence anymore by the direct detection because the device is now biased under the same mixing conditions (see 2.4.1 and [78], [79]). The result of a LOPS for a typical measured mixer is shown in Fig. 44.

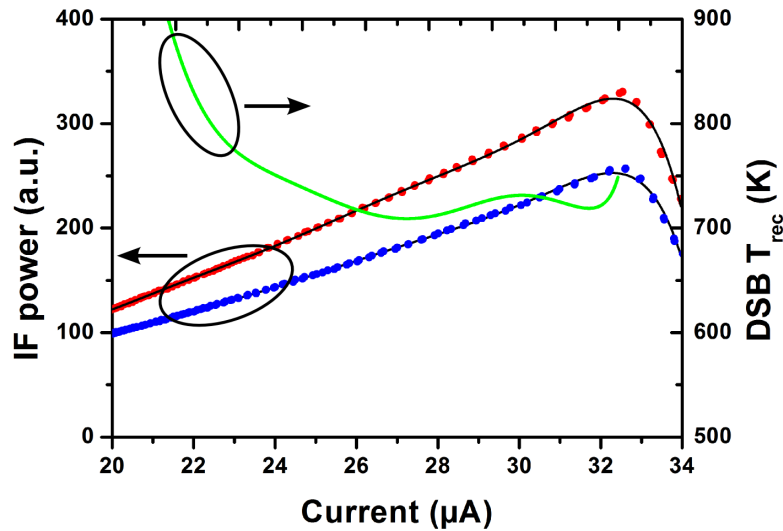


**Figure 44:** Local oscillator power sweep: IF power measured as a function of the bias current for a hot load (red) and cold load (blue) on the left axis and on the right axis is the receiver noise temperature (green).

This method delivers the optimal amount of LO power (grid position) and bias current for the fixed bias voltage at which the LOPS performed. The  $P_{LO}$  at this stable operating point is then kept fixed for the best performance in the spectral IF response from Sec. 5.4.3.

### 5.4.3 Spectral Intermediate Frequency Response

A Digital Fourier Transform Spectrometer (DFTS) is used for a spectral resolved measurement. The Array Fast Fourier Transform Spectrometer (AFFTS) is a spectrometer with a

spectral resolution of 212 kHz over a bandwidth of 1.5 GHz (8192 Channels) [80]. The DFTSs is used with the mixing path in the intermediate frequency-box to measure the spectrum over a range of 0.2 - 5.0 GHz to cover the HEB mixer bandwidth (see Sec. 4.1). A DFTSs used in astronomy for example in GREAT and upGREAT (see Fig. 3) for wide-band and high resolution observations.

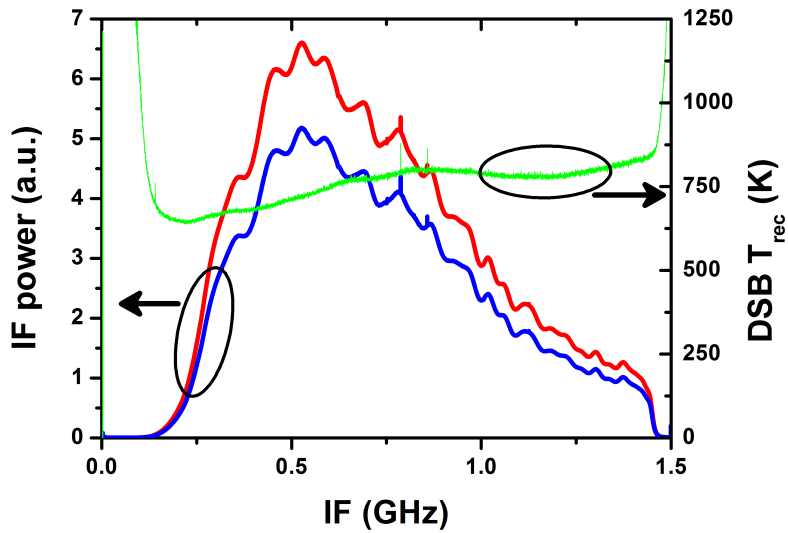


**Figure 45:** IF power measured as a function of IF for the hot load (red) and cold load (blue). The standing wave in the measured IF power coming from the optical standing waves which are constant and not influence the noise temperature. On the right axis the receiver noise temperature (green) is plotted.

## 6 Characterization of the HEB Mixers

The following chapter focuses on a detailed DC and heterodyne characterization of HEB mixers for both 1.9 and 4.7 THz operation frequencies. As material for the superconducting film two possible material combinations were studied. The first material combination is a superconducting NbTiN film on a Si<sub>3</sub>N<sub>4</sub> membrane substrate. This material combination was well studied for single mixers for the GREAT receiver by Pütz et al. [54]. The second material combination is a superconducting NbN film on the Si membrane substrate. This material combination was already very thoroughly studied by other groups and has consistently proven to be the material combination that gives the best mixer performance [34] [37]. Experimental data show that the mixer noise bandwidth of mixers based on NbN is significantly higher compared to those which are based on NbTiN. The noise bandwidth of NbTiN HEBs is in the order of 2 GHz and the one of NbN HEBs is in the order of 4-6 GHz [54] [34] [37]. For observations a large noise bandwidth is important to cover broad transition lines with a single measurement due to the broadening from the Doppler effect. A comparison of the measured performance of the HEB mixers based on NbN and NbTiN is shown in Ch. 7.

This chapter is subdivided into five sections. In the first two sections, the results of the 1.9 THz mixers based on NbN for metal and Si inlay waveguide blocks are presented. The main focus lies on the LFA mixers for LFA receiver channel for GREAT. In the third part, the 1.9 THz mixer results for the NbTiN based device are shown. Furthermore the result of a 4.7 THz mixer for the GREAT H-channel are present in the fourth part. In the fifth part the HEB mixer is used for characterization of a QCL local oscillator. A detailed discussion about the results in this chapter is shown in Ch. 7.

### 6.1 HEB Mixers Based NbN

In this section, a detailed characterization of mixers based on NbN film on a Si membrane substrate is presented. These mixers are devices which are later integrated into the LFA receiver channel for GREAT [23] [19]. The DC properties and the change after the mounting of the device is shown in the first half of this section. The RF properties of the broadband RF response to the IF response are present in the second half of this section. In total, the data from 19 mixers are used for all analysis because for these mixer a similar measured data set were available.

### 6.1.1 DC Properties

After the separating of the fabricated wafer into sectors (see Sec. 3.2.1), the DC properties of the devices are measured. The individual sectors are measured for the verification of the device DC properties and for a preselection of devices for the mixer assembly. The DC characterization of the devices is done for the current-voltage (I-V) characteristics and for the temperature-resistance (R-T) dependencies. The R-T characteristics of a typical device are shown in Fig. 46. It is a device from the wafer 14-11 from sector J.

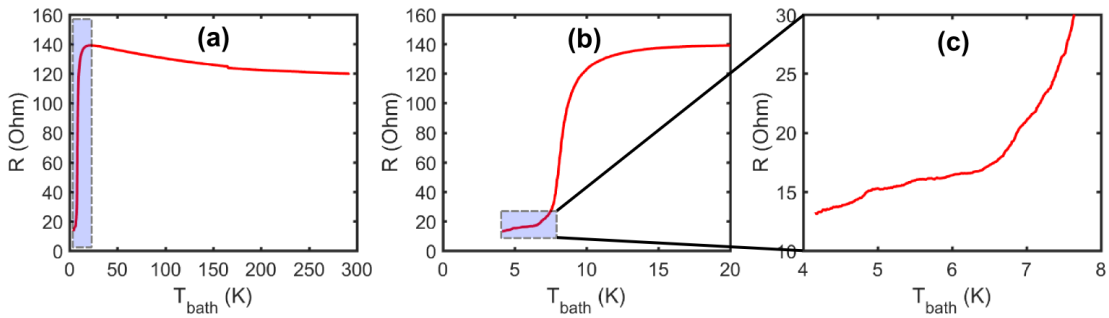


**Figure 46:** Left Plot(a): resistance dependency of the temperature between 4.2 - 295 K for the device 14 from sector J of wafer 14-11. Center plot (b): resistance dependency of the temperature between 4.2 - 20 K. Right Plot (c): Resistance dependency of the temperature between 4.2 - 8 K.

Three effects in different temperature ranges are shown. The first temperature range is starting from room temperature until about 25 K. During cooling the device the resistance increases with decreasing temperature (a) Fig. 46) and reaches the maximum of the resistance about 25 K (b) Fig. 46). Afterwards, The resistance decreases rapidly until it reaches the critical temperature  $T_c$  which is 7.8 K for this test device. This transition belongs to the characteristics of the NbN film between the two gold contact pads. After this transition, the resistance reaches a plateau, which is thought to be the result from the proximity effect of the gold contacts on the NbN layer (c) Fig. 46) [81]. The third transition, hardly visible, below 5 K is thought to be due to the transition of the bilayer of NbN-Au leads (200 nm thickness).

To check the uniformity, the measurements of the RT and IV curves were studied. However, the device IV and RT characteristics deteriorate slightly during the final handling steps inclusive membrane etching and mounting into the mixer. So in addition, the RT and IV curves are measured again after assembly. The comparison of all R-T curves for the separated sectors and the assembled mixers is shown in Fig. 47 for the sectors J and N of wafer 14-11, respectively in Fig. 48 for the sectors J and R of wafer 14-08. The devices from these sectors are used for the LFA mixers. The residual resistance in the R-T curves on the handle

wafer is attributed to the series resistance caused by the 3 mm long and 200 nm thick gold leads on the wafer (see Sec. 3) that is also visible in the IV-curves of Fig.'s 49 and 50. The series resistance in the RT curves in the dewar is subject of further study.

In the following, we concentrate on the main transition of the RT and investigate changes to  $T_c$  and  $R_n$  and the increase in their variance related to processing and handling of wafer sections.

The DC resistance of a mixer at room temperature is a probe for the device sheet resistance at 4.2 K. The normal state resistance increases for all devices after the final fabrication steps and assembly of the mixer unit. The results for the measured R-T curves and for the I-V curve of a set of measured mixers are listed in Tab. 6.

The I-V measurements before the device separation and after the mounting was done with a liquid Helium dipstick. It is very much visible that the device characteristics of sector R changed significantly from on-wafer diptest to device mounting the mixer block. A further analysis of the DC results is shown in Sec. 7.1.1.

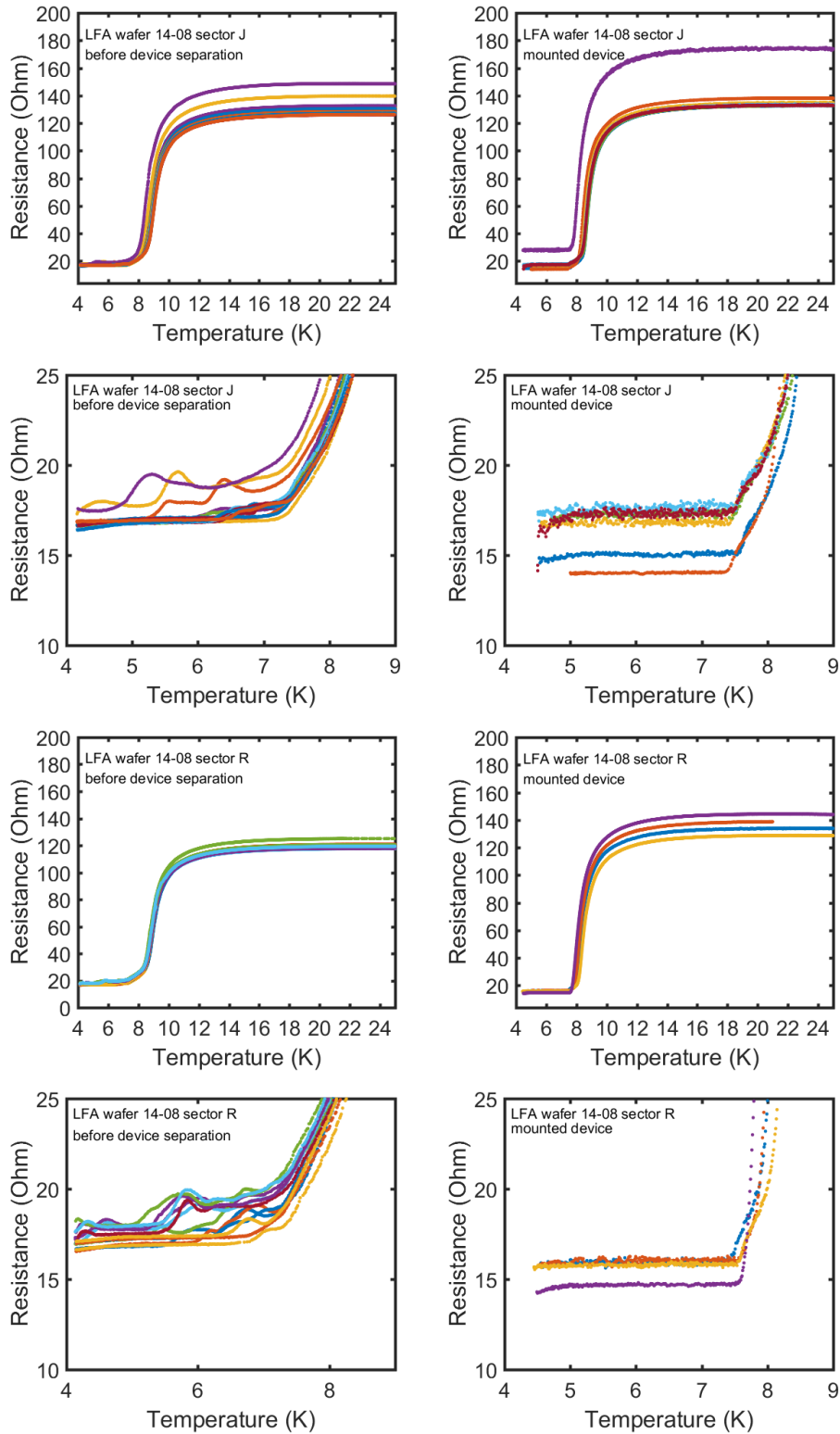


**Figure 47:** Set of R-T measurements for the devices from wafer 14-08 of sector J and R. Plots on the left side are measured before the device separation and on the right side after the mounting of the devices.

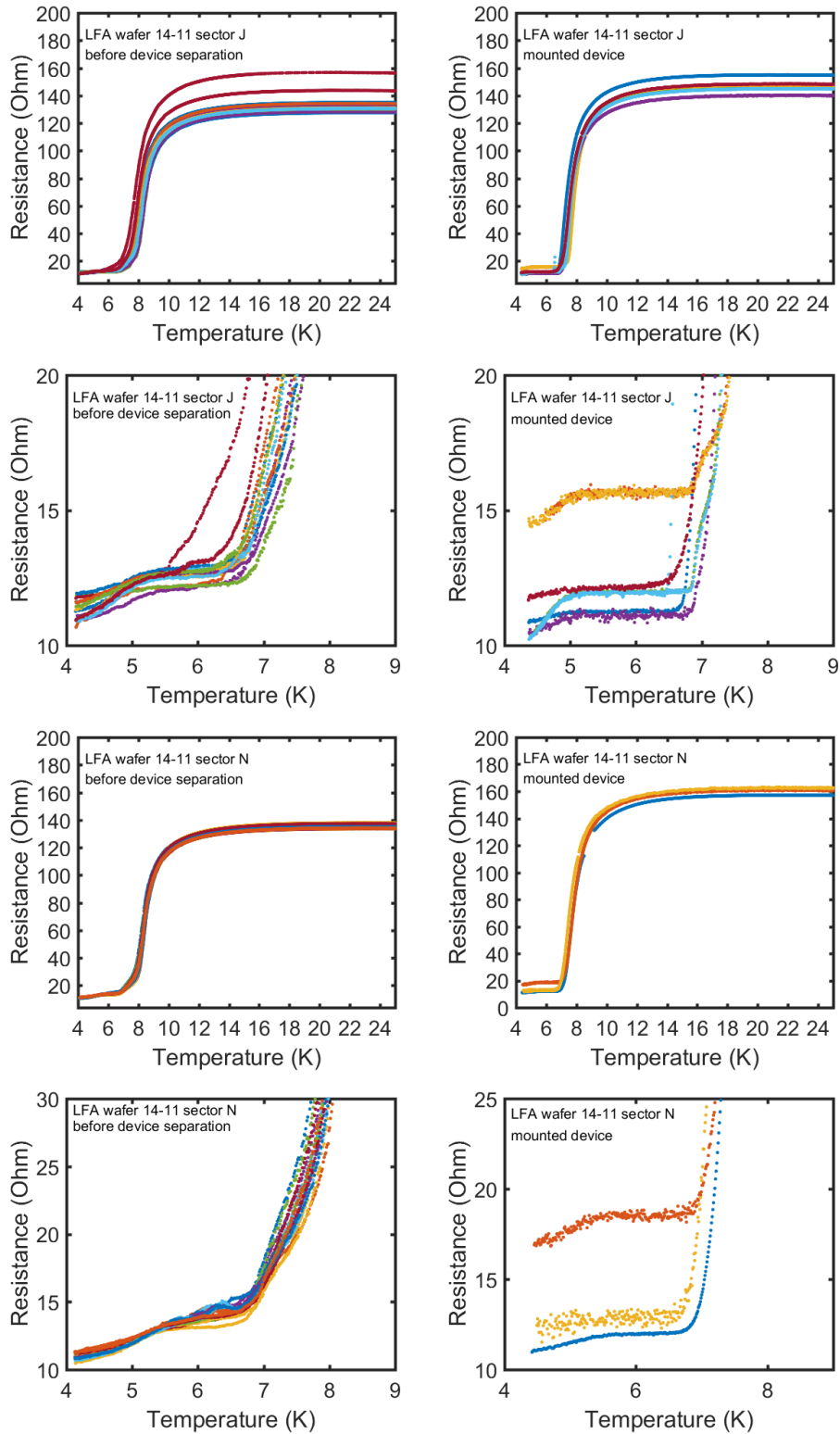


**Figure 48:** Set of R-T measurements for the devices from wafer 14-11 of sector J and N. Plots on the left side are measured before the device separation and on the right side after the mounting of the devices.

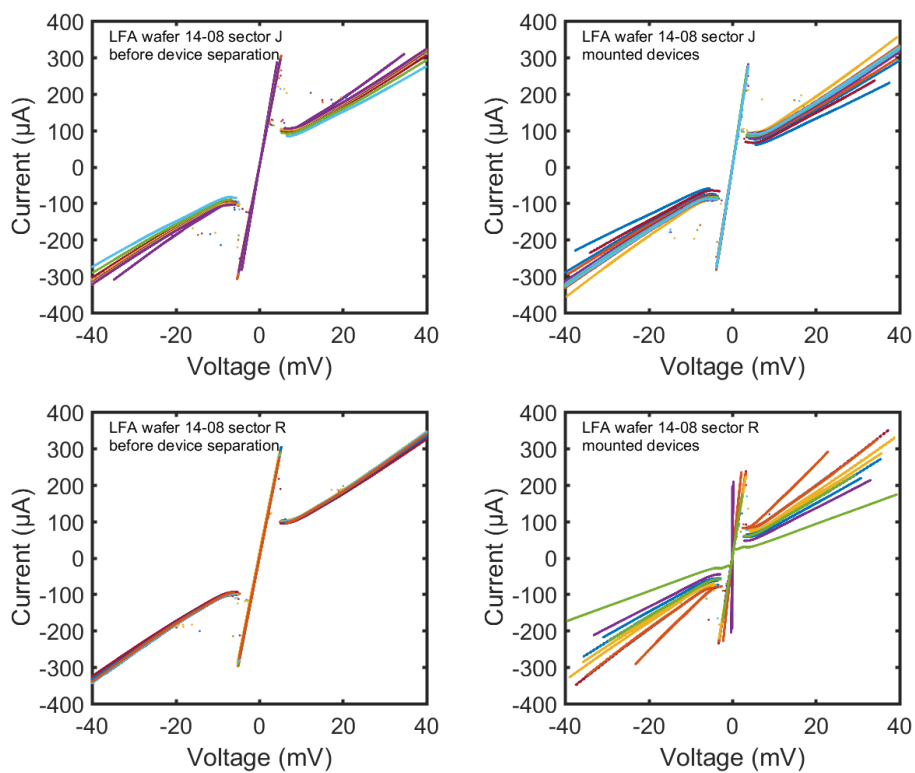


**Figure 49:** Set of I-V measurements for the devices from wafer 14-08 of sector J and R. Plots on the left side are measured before the device separation and on the right side after the mounting of the devices.

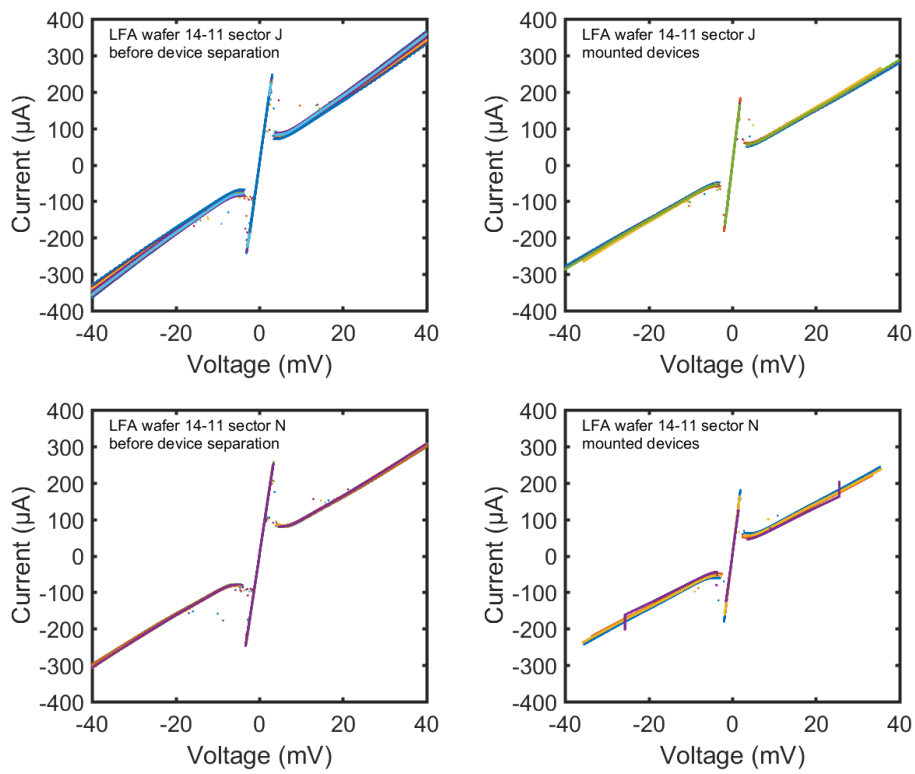


**Figure 50:** Set of I-V measurements for the devices from wafer 14-11 of sector J and N. Plots on the left side are measured before the device separation and on the right side after the mounting of the devices.

## 6.1.2 Analysis of the Resistance Change

The residual resistance ( $R_{4K}$ ) is measured at a bath temperature of 4.2 K and determined from the linear slope of the IV curve around a bias voltage of 0 mV is shown in Fig. 51. In addition the peak resistance at 20 K is shown in Fig. 52. The averaged  $R_{4.5K}$  value of wafer 14-11 devices are 11  $\Omega$  respectively 14  $\Omega$  for 14-08. The averaged  $R_{peak}$  values of wafer 14-11 devices are 150  $\Omega$  respectively 130  $\Omega$  for 14-08. The designed HEB impedance is 120 Ohm. The difference to the design values leads to an impedance mismatch which introduces loss into the circuit. This will be discussed in Sec. 6.1.7.

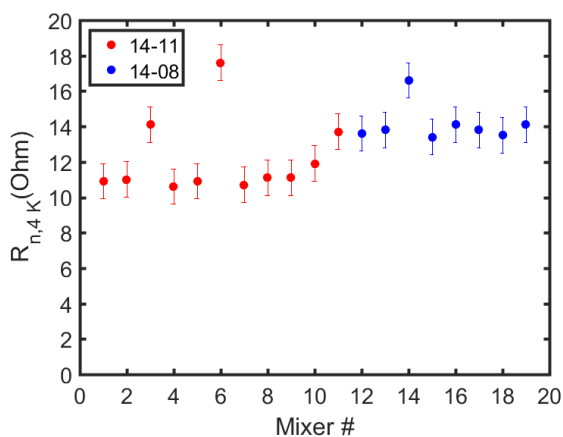


**Figure 51:** Residual resistance at 4 K for both wafers (red 14-11, blue 14-08) determined by the RT and IV curve.

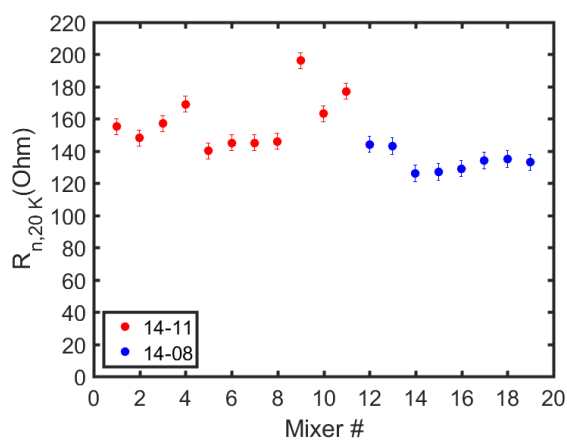


**Figure 52:** Resistance at the peak of the RT curve at about 20 K for both wafers (red 14-11, blue 14-08).

wafer	sector	device	T <sub>c</sub> (K)	Δ T <sub>c</sub> (K)	R <sub>4.5K</sub> (Ohm)	R <sub>peak,~22K</sub> (Ohm)	R <sub>300K</sub> (Ohm)
14-11	J	6	7.52	1.81	10.8	155	127
14-11	J	18	7.75	1.77	10.9	148	121
14-11	N	13	7.94	1.92	11.0	157	130
14-11	N	7	7.79	1.85	14.1	168	129
14-11	J	14	7.77	1.70	10.6	140	118
14-11	J	17	7.79	1.52	10.9	145	121
14-11	N	3	8.12	1.61	17.6	145	121
14-11	J	13	7.99	1.52	10.7	147	118
14-11	R	3	7.21	1.82	11.1	190	132
14-11	N	19	7.83	1.65	11.1	162	133
14-11	N	17	7.56	2.39	11.9	171	134
14-08	R	19	8.31	1.59	13.7	144	107
14-08	R	16	8.65	1.64	13.6	129	113
14-08	R	14	8.75	1.48	13.6	127	114
14-08	J	11	8.95	1.45	13.4	129	112
14-08	J	16	8.87	1.50	14.1	134	107
14-08	J	12	8.79	1.37	13.8	135	108
14-08	J	8	8.93	1.46	13.5	133	100
14-08	J	15	8.94	1.38	13.8	133	107

**Table 6:** Table of properties for a set of 19 mixers. The properties were measured and calculated from the R-T curves of the assembled mixers.

### 6.1.3 THz Broadband Response of the Mixers

A measurement of the broadband RF response of each mixer is an important instrument to check the RF circuit of the HEB film. Measured deviations can be used as a feedback into the RF design or point to issues with the feedhorn to waveguide interface. A shift in the RF band is an indication of misalignment of the device inside the block or a shift of the feed horn in respect waveguide of the block which is shown for a 4.7 THz device in Sec. 6.4.2. A flat and low intensity RF response is an indication a bad coupling to the HEB (e.g. losses introduced by a particle inside the horn). A reason for this effect can be either an issue of the feed horn or the antenna probe on the chip. Only a few measurements of the wafer 14-08 are available due a broken FTS beamsplitter during the measurement period. The response measurements of the mixers were corrected for the frequency response of the FTS source.

The response of 11 mixers from the wafer 14-11 and one mixer from 14-08 are plotted in Fig. 53. The black dotted line is the simulation response from the design of the mixer's RF circuit (see Sec. 3.1.1) and the black dashed line indicates the frequency of the LO for my heterodyne measurements. In addition the bottom plot in Fig. 53 shows a zoom of the response between 1.85 - 1.95 THz. The frequency dependence of the response of both wafers was very similar. The low frequency cut-off varies in about 0.1 THz for the measured mixers. The overall shape of the RF responses is equal for all mixers which indicates that the manufacturing of the waveguide is very precise. The absorption lines in the RF band are caused by water vapor in the air path of 2 - 3 cm between the dewar and the FTS and partly by the remaining water vapor inside the evacuated FTS. The difference between the simulation and the measured RF response is discussed in the Sec. 7.1.2 of the Ch. 7.

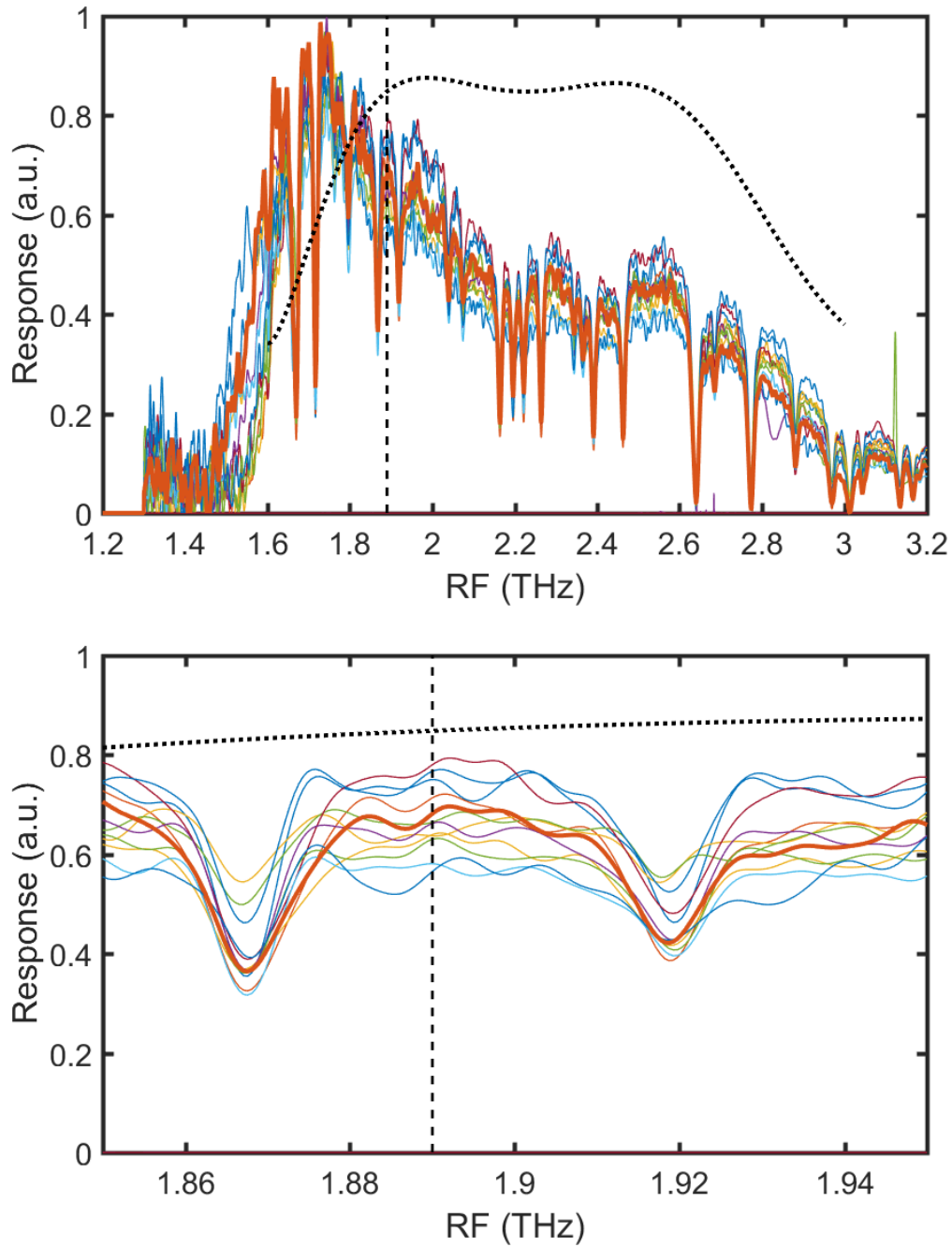


**Figure 53:** FTS measurement of 11 devices from 14-11 and one device from 14-08. The response of mixers is measured in a.u. (auditory units) as a function of the RF frequency. Dashed line indicating the frequency of the heterodyne experiments. The bottom plot shows a zoom on the operation frequency. The two absorption lines at 1.86 and 1.92 THz are from residual water vapour in the optical path.

### 6.1.4 Heterodyne Response

The HEB mixer sensitivity is measured by the receiver noise temperature. The receiver noise temperature ( $T_{rec}$ ) can be calculated from the Y-factor method explained in Sec. 2.4. To be able to compare all mixers the measured data have to be corrected for the different beamsplitter (BS) configurations. The BS coupling for the radiation is optimized for each mixers individual for the different amounts of incident LO power for optimal operation. For a higher incident LO power requirement the BS has to set to a higher reflection of the LO radiation to the mixer and lower transmission of the radiation of the calibration loads.

For the mixers of wafer 14-08 a wire grid with different coupling (rotational angle) was used as a beamsplitter in most measurements and for mixers of wafer 14-11 a 12  $\mu\text{m}$  Mylar foil (see Sec. 4.1 and Fig. 33). The radiation coupling of 0.96 using the Mylar foil was used for the mixers which need a incident LO power requirement below 1.5  $\mu\text{W}$ . For mixers that required more incident LO power, a wire grid was used. The coupling depends on the angle of the wire to the horizontal ranging from 0.44 - 0.96. The amplitude of the standing waves in the IF (see Fig. 36) depending on the coupling of the LO radiation. The amplitude is increased for higher LO coupling.

For a better comparison, the measured receiver noise temperatures ( $T_{rec,c}$ ) was corrected for the transition of the radiation through the beamsplitter ( $G_{BS}$ ). The measured input power was elevated due to the additional input power coupled from the room temperature load which couples in transition to the mixer. To calculate the  $T_{rec,c}$ , the physical temperature ( $T_{el}$ ) of the load has to calculated first by:

$$T_{el} = T_{coldload} \cdot G_{BS} + T_{room} \cdot (1 - G_{BS}). \quad (38)$$

Besides the beamsplitter, all other components in the signal path of the receiver were not corrected for. There individually measured transmission properties are summarized in Tab. 7. The table lists two frequencies corresponding the two different local oscillator units used during mixer characterization (see Sec. 6.5 [82]).

The losses of the air path of 35 cm are estimated in Sec. 4.1. The total optical losses ranging from 0.31 to 0.69 (-5.1 to - 1.6 dB). The receiver heterodyne performance is measured using three different routines (the local oscillator power sweep, DC current voltage sweep and the spectrometer measurement) which are all based on the Y factor method mentioned in Sec. 2.5.

frequency (THz)	Gain at 1.88	Gain at 1.89	Physical temp. (K)	Planck temp. (K)	Noise temp. (K)	Noise temp. (K)
beamsplitter	0.44 - 0.96	0.44 - 0.96	298	255	379 - 12	379 - 12
air path	0.87	0.91	298	255	101 - 46	67 - 31
window	0.933	0.924	298	255	56 - 26	61 - 28
IR filter	0.863	0.849	90	52	34 - 16	37 - 15

**Table 7:** Optical components from the hot/cold load to the mixer with their gain at 1.88 THz and 1.89 THz. Optical transmission (Gain) directly from FTS measurements. The Physical, Planck and noise temperature of these components are listed.

### 6.1.5 Local Oscillator Power Sweep

A typical measurement of a local oscillator power sweep (LOPS) is shown in Fig. 54.

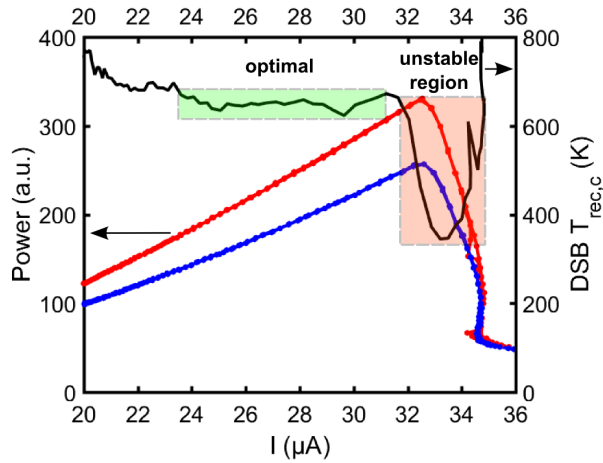


**Figure 54:** The detected power measured as a function of the bias current (representing sweeping the LO power for Mixer N19 from wafer 14-11 operating at a bias Voltage of 1.25 mV. Left edge of the plot is over and right under pumped.). Red data points measurement of the hot and blue of the cold load. On the secondary axis the DSB receiver noise temperature is plotted.

The detected power is measured as a function of the bias current at fixed bias voltage. The current is changed by applying a varying amount of LO power modified by an attenuator grid in steps of the order of  $0.1^\circ$ . The averaged receiver noise temperature corrected for the beamsplitter coupling ( $T_{rec,c}$ ) between 1 - 2 GHz using a band pass filter is plotted on the secondary axis against the bias current.  $T_{rec,c}$  is almost constant over current range from 23 - 31  $\mu\text{A}$ . Starting at the maximum of the power level  $T_{rec,c}$  decreases for higher current (or less LO power).

When the LO power level leads to a mixer bias current of 32 - 34  $\mu\text{A}$ , the device leaves the stable operation point and  $T_{rec,c}$  decreases rapidly to a minimum of about 400 K. In this operating range a small change of LO power could lead to a significant change of the noise temperature. The DC IV curve is under-pumped and show a residual of the hysteresis. The under-pumped LO power level, we call the unstable region. Beyond that bias level the noise temperature increases rapidly. The results at the optimum operating point of mixers with devices from for both wafers 14-08 and 14-11 which were study are shown in Fig. 55. The noise temperature corrected for the beamsplitter coupling is given by  $T_{rec,c}$ . The averaged  $T_{rec,c}$  for wafer 14-11 is  $(750 \pm 50)$  K and for 14-08 was  $(700 \pm 50)$  K.

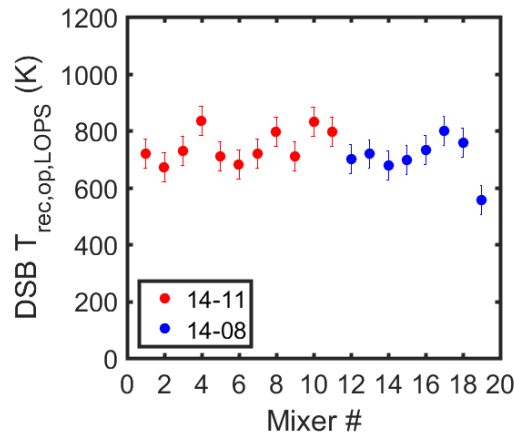


**Figure 55:**  $T_{rec,c}$  of the optimum operation point from the LOPS for a set of 19 mixers. 11 mixers of wafer 14-11 in red and 8 from wafer 14-08 in blue.

### 6.1.6 Voltage Sweep

For a voltage sweep, the LO power is set to a fixed value and the voltage is swept in 0.01 mV steps from -50 to 50 mV. At every voltage point the DC current through the HEB and the IF power at the receiver output in a 1-2 GHz detection bandwidth are measured with a power meter. In Fig. 56, the IV curves for an unpumped (no LO power), optimum and under pumped LO power levels are shown.

For the optimal and under pumped levels of the detected power, the noise temperature and current are shown as a function of the bias voltage in Fig. 57. Plot a) shows a zoom on IV curve. The optimum pump level in comparison with the under pumped level (unstable region) shows no residual hysteresis. The hysteresis should not be confused with a small direct detection effect (see Sec 2.4.1) which is visible as well, also in the optimum pumped curve. Plot b) shows the measured power with a power-meter, scaled in arbitrary units. The

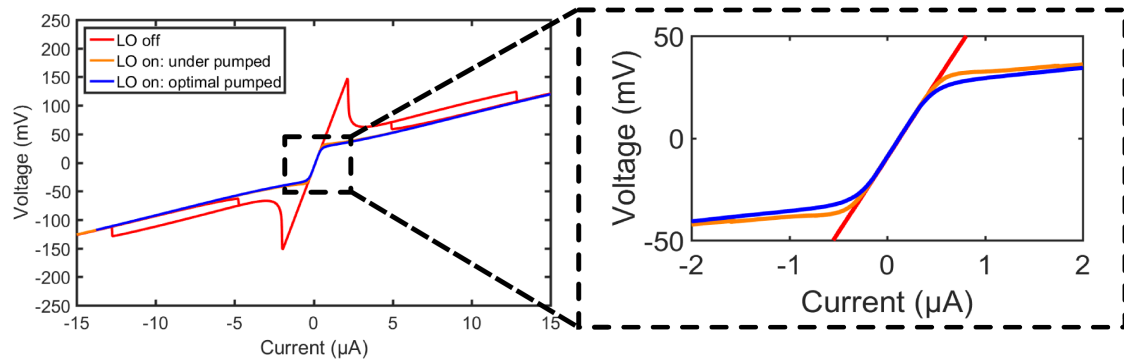


**Figure 56:** Current plotted against the Voltage for three LO levels: LO on: under pumped, LO on: optimum pumped and LO off. Right plot show a in zoom on the central part of the IV. (device R19, wafer 14-08)

power in the unstable region is obviously connected to the hysteresis in the IV curve. In part c.) the  $T_{rec,c}$  for both cases are shown.

For a wide voltage bias range from 0.6 to 1.6 mV which is typical of NbN mixers a nearly constant optimal  $T_{rec,c}$  can be achieved. The unstable region shows a jump of  $T_{rec,c}$  of about 50 % between 0.6 mV and 1.4 mV which is the voltage range of the hysteresis. The unstable region appears for both wafers at a similar bias range 0.5 - 1.5 mV and at a current of 30 - 50  $\mu$ A and can also observe in the measurements of the NbTiN mixers (see Fig. 77). The unstable region is there for all mixers I have tested, given a certain LO power and bias voltage range.

The optically corrected noise temperature ( $T_{rec,c}$ ) averaged over the device from the wafer 14-11 for this method is  $(820 \pm 80)$  K and for 14-08 is  $(800 \pm 60)$  K. The results for wafer 14-08 and 14-11 are shown in Fig. 58.

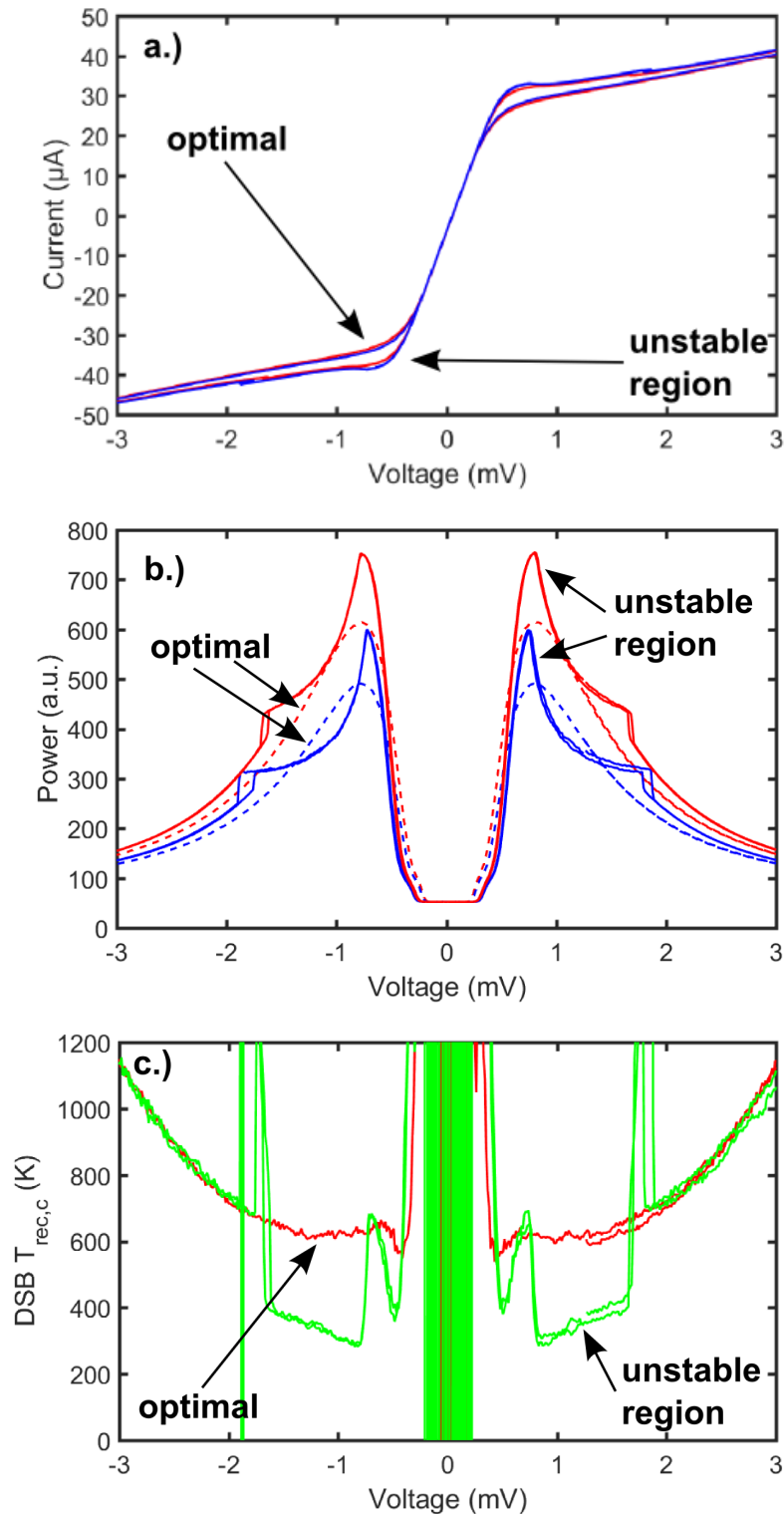


**Figure 57:** HEB mixer IV curve for two different pump levels for an optimum operation and under-pumped (unstable region). In plot a.) and b.) the red curves correspond to the measurements of the hot and blue of the cold load. a.) Zoom on the DC IV curve. b.) Detected power level in a.u. as a function of bias Voltage. c.) DSB receiver noise temperature as a function of bias Voltage. (device R19, wafer 14-08)

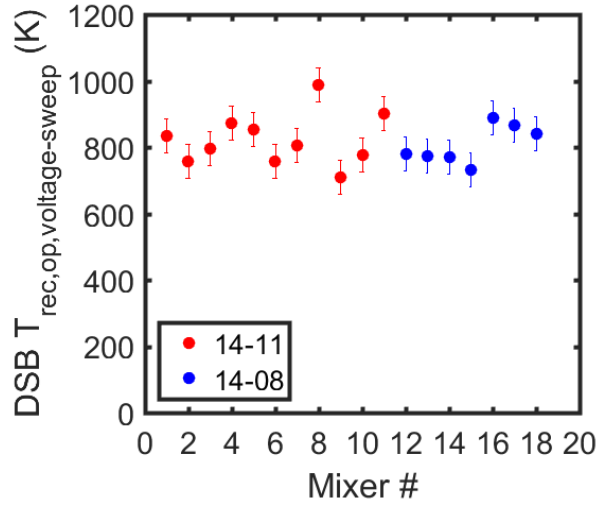


**Figure 58:** The receiver noise temperature for optimum the operating point of voltage sweep measurements (IF power between 1 - 2 GHz) of a set of 19 mixers. Device from wafer 14-11 in red and 14-08 in blue. The measurement of Mixer number 19 is missing because the data set was not complete recorded.

### 6.1.7 Mixer Gain and Noise Temperature

For the de-embedding of the mixer performance from  $T_{rec,c}$ , the IF chain which is an important part of a receiver system has to be calibrated. Here the IF noise temperature and the IF gain have to be determined. The first calibration of the old IF chain was done in the beginning of the LFA measurement series. This old IF chain was optimized for AFFTS (see Sec. 4.2) with a bandwidth of 1.5 GHz. By the introducing of the two XFFTS, with bandwidth of 2.5 GHz for each spectrometer, a new IF chain had to be cross calibrated to be able to compare the measurements with both IF chains. As a calibration mixer I used the mixer M40 (device J19) from the wafer 14-08 which is still available for tests in Cologne (and not integrated into the upGREAT receiver). This mixer was measured in detail in with both IF chains.

First, I calibrated for the new IF chain using a 50 Ohm load instead of a mixer inside the dewar. This load has a good match to the impedance of the LNA input. A temperature diode and a heater are mounted on the load to measure the output noise as a function of the load temperature. The IF output noise can be measured either by a spectrometer or by a power meter. The IF noise temperature can be calculated by the Y-factor method based on measurements at least two different load temperatures. The resulting IF noise temperature as a function of the IF measured with the an array fast Fourier transform spectrometer (AFFTS, see Sec. 5.4.3) is shown in Fig. 59. The IF noise of the old chain is almost constant with a value of 6.5 K over band form 0.4 - 5 GHz. The IF noise temperature of the new IF

chain is measured with a different spectrometer. The spectrometer is a XFFTS [72] with a bandwidth of 2.5 GHz and a channel number of 32k [72]. Each channel has a width of 80 kHz. Also the result of the IF noise temperature for the new chain is shown in Fig. 59. The noise temperature of the new chain also starts at 6 K, but rises up to 10 K.

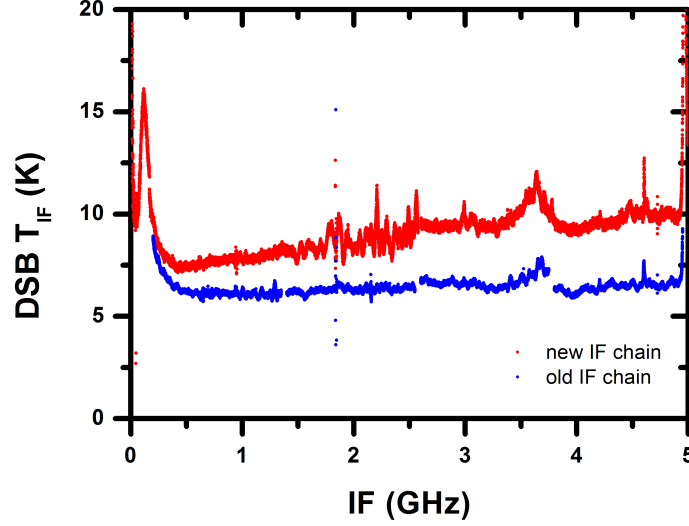


**Figure 59:** Noise temperature of the old IF chain measured with AFFTS spectrometer and new IF chain after the integration of two FFTS spectrometer. The old IF chain is plotted in blue and the new in red.

The gain of both IF chains can be determined by measuring power at the output of the IF chain for different but known input temperatures, provide one records the settings of the variable attenuators. The measured power as a function of temperature is shown in Fig. 60. In this plot the linearity of the new IF chain is shown which is important for reliable measurement results for the power.

The averaged power measured in  $\mu\text{W}$  over a bandwidth of 1 - 2 GHz with the power-meter can be used to calculate the averaged IF gain in this band. The gain is determined by:

$$G_{IF}(1-2\text{GHz}) = \frac{[P_{out}(hot) - P_{out}(cold)] \cdot 10^{att/10}}{k_B B (T_{hot} - T_{cold})}, \quad (39)$$

with an error calculated with the Gaussian error propagation of:

$$\Delta G_{IF}(1-2\text{GHz}) = \sqrt{2 \left( \frac{\Delta P}{P_o(h) - P_o(c)} \right)^2 + \left( \frac{\Delta B}{B} \right)^2 + \left( \frac{\Delta T_h}{T_h - T_c} \right)^2 + \left( \frac{\Delta T_c}{T_h - T_c} \right)^2}, \quad (40)$$

here  $P_{out}(i)$  is the measured power in  $\mu\text{W}$ ,  $att$  is the internal attenuator setting of the

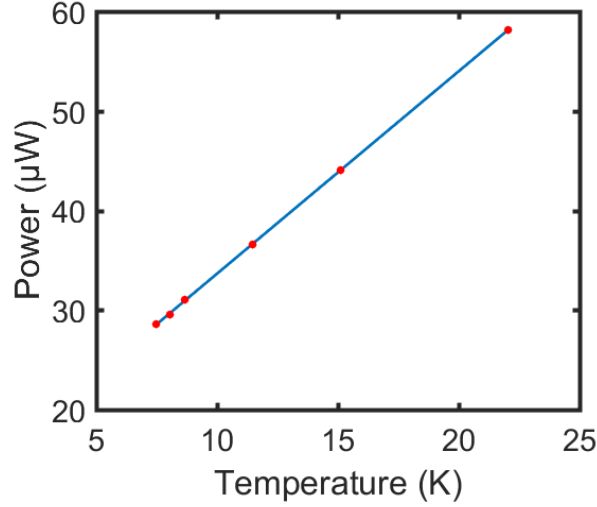


**Figure 60:** The cold IF chain measured with a 50 Ohm load at the input of the LNA as a noise source. The detected power measured with a power-meter in  $\mu\text{W}$  between 14 and 7 K. Interpolation of the linear dependency represented by the solid line.

IF box in dB,  $k_B$  is the Boltzmann constant,  $B$  the filter bandwidth of the IF box and  $T_i$  the physical temperature of the load. The output of the IF box for the power-meter is restricted with a 1 - 2 GHz bandpass to a  $B$  of 1 GHz. The error of the power I estimated as  $1 \mu\text{W}$  at the power-meter (error  $< 1\%$ ). The measured temperatures are within 0.01 K, because the temperature drifts due to the heating with heater over the integration time of about of 2 - 5 min. The attenuator assumed to have a negligible error in comparison to the other errors. The averaged  $G_{IF}$  (1 - 2 GHz) is then equal to  $(86.5 \pm 0.3)$  dB.

For the calculation of the mixer gain the total receiver and the "gain" in the signal path between the external calibration load and the mixer. The latter gain of the receiver system can be calculated by the product of all lossy optical components listed in Tab. 7. The receiver gain can be calculated from the measured power values at a heterodyne measurement with a mixer. The averaged receiver gain at 1 - 2 GHz is equal to:

$$G_{rec}(1 - 2 \text{ GHz}) = \frac{(P_{hot,out} - P_{cold,out}) \cdot 10^{att/10}}{k_B B (T_{hot} - T_{cold})}, \quad (41)$$

with an error, giving by Eq. 40. Here the accuracy of the temperature of the hot load is assumed to be 5 K (resulting in a  $\Delta T_{rec} \pm 20$  K) because the room temperature was never accurately measured during the operation of the mixer. The temperature of the cold load is assumed to be more accurate because I used an absorber covered by liquid nitrogen with an error of 1 K. The mixer gain of the individual mixer, then can be calculated in linear units by:

$$G_{mix} = \frac{G_{rec}}{G_{IF}G_{op}}, \quad (42)$$

with an error calculated with the Gaussian error propagation of

$$\Delta G_{mix} = G_{mix} \sqrt{(\Delta G_{rec}/G_{rec})^2 - (\Delta G_{IF}/G_{IF})^2 - (\Delta G_{op}/G_{op})^2}. \quad (43)$$

A list of the different gains is listed in Tab. 8, the IF gain of the old IF chain can be calculated by the results from the new chain. I assumed that the mixer gain is unchanged. The gain of the old chain is then equal to 88.4 dB, which is about 2 dB higher in comparison to the new chain.

device	IF chain	$G_{op}$ (dB)	$G_{rec}$ (dB)	$G_{IF}$ (dB)	$G_{mixer}$ (dB)
J19 (14-08)	new (2016)	$-5.5 \pm 0.1$	$74.9 \pm 0.5$	$86.5 \pm 0.3$	$-6.1 \pm 0.4$
J19 (14-08)	old (2015)	$-1.5 \pm 0.1$	$80.9 \pm 0.2$	$88.4 \pm 0.6$	$-6.1 \pm 0.4$ (assumption)

**Table 8:** Listed gain of the IF chains and the test mixer J19 for the calibration of both chains. The mixer gain is assumed to be constant over time period of 20 months.

The mixer noise temperature can be calculated by (followed by Eq. 32):

$$T_{mix} = (T_{rec} - T_{op}) \cdot G_{op} - \frac{T_{IF}}{G_{mix}}, \quad (44)$$

where  $T_{op}$  is the optical noise temperature of n optical components:

$$T_{op} = \frac{T_1(1 - G_1)}{G_1} + \frac{T_1(1 - G_2)}{G_1 G_2} + \dots + \frac{T_1(1 - G_n)}{G_1 \cdot G_n}. \quad (45)$$

The mixer noise temperature of this mixer J19 (14-08) is about  $480 \text{ K} \pm 50 \text{ K}$  which is 10 times the quantum noise limit of  $90 \text{ K}$  ( $\frac{hf}{2k_B}$ ). The errors of the mixer gain and noise temperature are calculated with experimental errors listed in Tab. 9.

The measured resistance  $R_n$  at the peak of the R-T curve shown in Sec. 6.1.2 in comparison to the design value of 120 Ohm leads to a impedance mismatch. The change of the gain for individual device is calculated in CST and considered in the calculation for the mixer gain and noise temperature is in Sec. 7.1.4. As discussed in Sec. 3.1.2, the IF impedance mismatch is negligible for the mixer performance. The noise temperature and the gain of the mixer of two sets of mixers from the wafer 14-08 and 14-11 are shown in Fig. 61.

property	estimated errors
power of the power-meter	1 $\mu$ W
bandwidth of the 1-2 GHz filter	0.01 GHz
temperature of the hot load	5 K
temperature of the cold load	1 K
beamsplitter grid angle	2.5 $^{\circ}$ (0.04-0.03)
beamsplitter Mylar	0.01
window	0.01
IR-filter	0.01
air absorption	0.10

**Table 9:** Estimated losses of measured properties of the gain in absolute values.

The averaged mixer noise temperature is determined using the Callen-Welton expression from Eq. 31, corrected for the impedance mismatch of the device, is  $(410 \pm 30)$  K for devices from the wafer 14-08 and  $(450 \pm 30)$  K for devices from wafer 14-11. The averaged mixer gain from the devices of wafer 14-08 is about  $-(5.2 \pm 0.3)$  dB and for wafer 14-11  $(-6.2 \pm 0.2)$  dB which is comparable with the results of -6 dB from Miao et al. [83]. A single device can generally not be identified by its mixer gain and mixer noise as belonging to one of the wafers. Taken all data from both wafers they can be distinguished as the overall gain is higher and the overall noise temperature is lower for wafer 14-08. A discussion of this results with a comparison to the theoretical lumped element model is presented in Sec. 7.1.4.

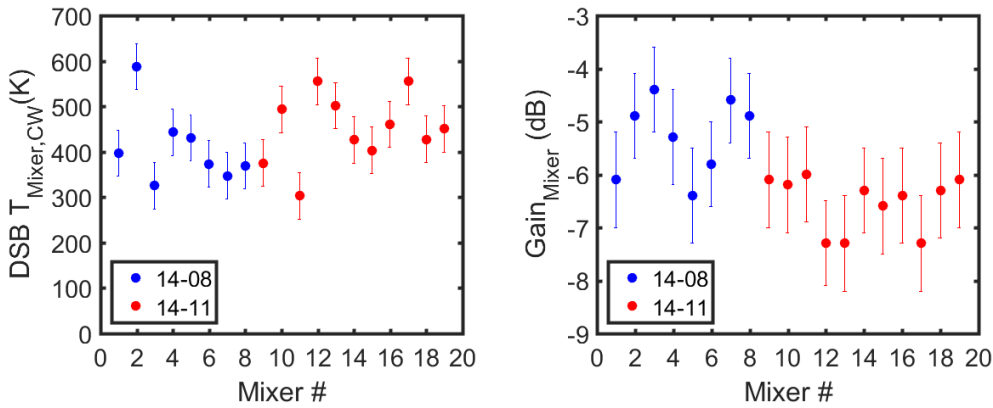


**Figure 61:** The averaged (1 - 2 GHz) mixer noise temperature for a set of 19 mixers are plotted in the left figure. The averaged (1 - 2 GHz) mixer gain for the same set of 19 mixers are plotted on the right figure. Both gain and the noise temperature are measured at the optimal operating conditions with a bias voltage of about 1.25 mV and an optimal LO power level with the lowest noise temperature.

### 6.1.8 Spectrometer Measurements

The frequency resolved IF noise can be measured with an array fast Fourier transform spectrometer (AFFTS see Sec. 5.4.3). In Fig. 62 a typical spectrum of a mixer is shown.

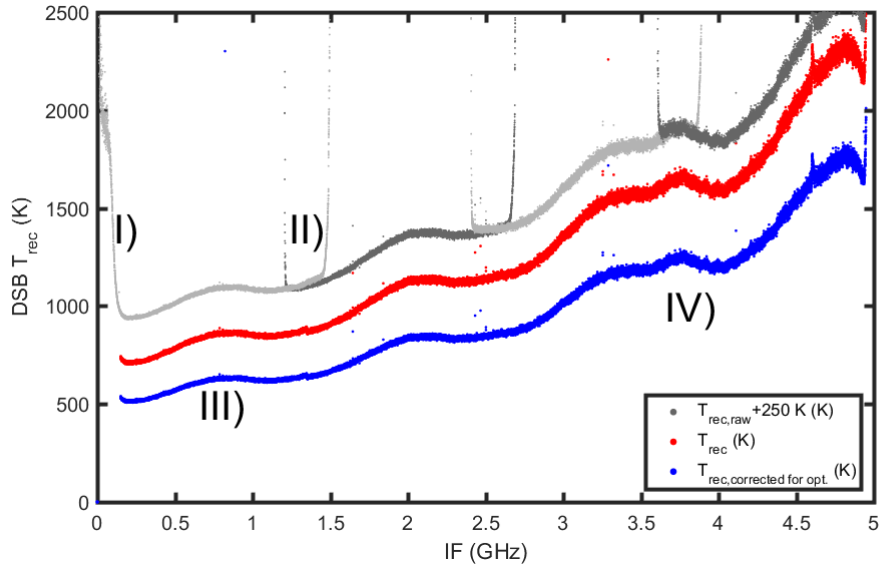


**Figure 62:** The  $T_{rec}$  measured with the AFFTS as a function of the IF. The gray points show the uncut and uncorrected measured noise bandwidth an offset of plus 250 K. The red points representing the cut and reconstructed band. The green line is a single roll of fit of the spectrum. The blue points are the receiver band corrected for all optical losses from the load to the mixer. The four artifacts (I-IV) are due to the measurement set-up and not due to the mixer.

The noise band of each mixer shows the same four effects which are artifacts of the test setup and not of the mixer. The effects are listed by the Roman numeral I to IV. At the lower frequency edge from 0 to 0.2 GHz the IF chain, especially the LNA gain rapidly decreases towards 0 GHz (I). Therefore the noise temperature is increasing below 0.2 GHz. Due to the limited bandwidth of the AFFTS spectrometer of 1.5 GHz, the band of the complete receiver spectrum has to be measured in 4 separate measurements with slightly overlapping frequency bands (II). Those bands have to stitch together to reconstruct the full band of the receiver (see 4.2). In addition the receiver band shows a standing wave with a period of about 1.1 GHz (III). The origin of this standing wave is a mismatch in the IF between the mixer and the LNA. The period is equal to length of 6.2 cm which corresponds to a transition trough Teflon dielectric in the connectors and the bias-T. At 3.7 and 4.6 GHz there are two features in the IF of the receiver (IV). Both are an artifact from the IF processor which are constant in frequency and are neglected in the determination of the mixer properties. The origin of those features is inside the IF-box due to issues of the mixing path with overlapping side

bands. The averaged (1 - 2 GHz) optical corrected receiver noise temperature are plotted in Fig. 63. The mean  $T_{rec,c}$  of the mixers of the wafer 14-11 was  $(900 \pm 60)$  K and from 14-08  $(870 \pm 40)$  K.

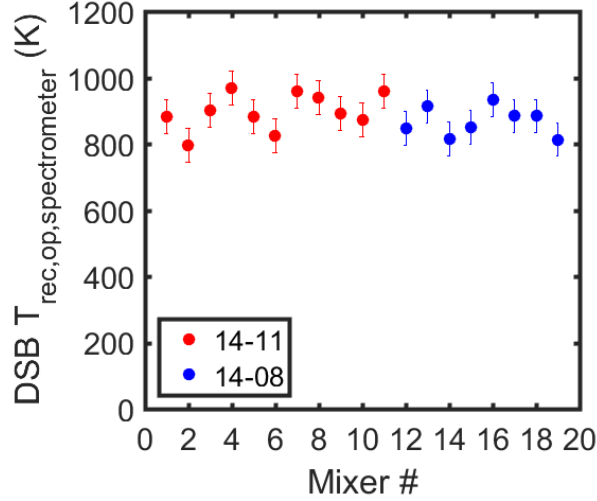


**Figure 63:** Averaged (1 - 2 GHz) receiver noise temperature, at optimum conditions, for the set of 19 mixers. 11 mixers of wafer the 14-11 in red and 8 from wafer 14-08 in blue. Both are measured at the optimal operating conditions with a bias voltage of about 1.25 mV and an optimal LO power level with the lowest noise temperature.

### 6.1.9 Noise Bandwidth

The Noise Bandwidth (NBW) can be calculated by using the measured spectrometer data from Sec. 5.4.3. This bandwidth can be fitted to first order by a single roll off fit to calculate the receiver noise bandwidth for each mixer [31]. The noise band was fitted by:

$$T_{rec}(f) = T_{rec}(0) \cdot (1 + (f/f_0)^2), \quad (46)$$

here  $f_0$  is the receiver NBW and  $T_{rec}(0)$  the noise temperature at 0 GHz. A typical fit of the data is shown in Fig. 64. The mixer is biased at the stable operation conditions with lowest noise temperature.

The NBW is calculated by Eq. 46 and plotted for all 19 mixers in Fig. 65.

The averaged bandwidth was  $3.9 \pm 0.4$  GHz. Both wafer 14-11 and 14-08 show similar averaged receiver NBW.

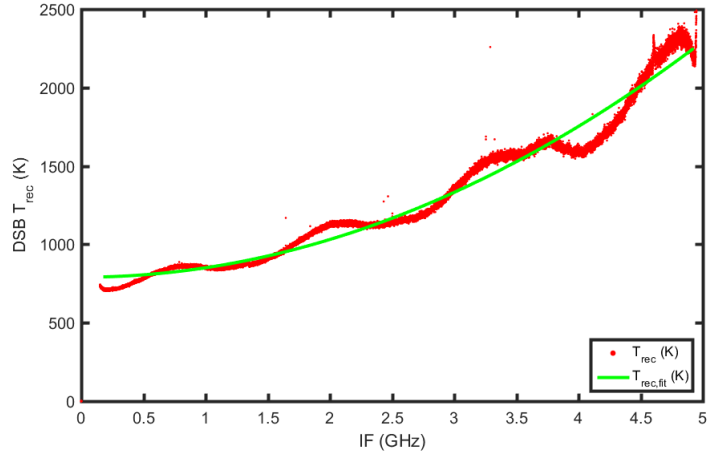


**Figure 64:** A comparison of the measured data from device J13 (wafer 14-11) with the fitted curve by using the Eq. 46.

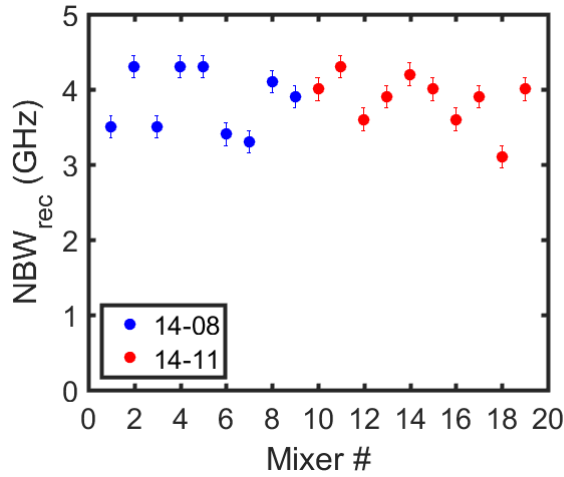


**Figure 65:** Receiver noise bandwidth for the set of 19 mixers. 11 mixers of wafer the 14-11 in red and 9 from wafer 14-08 in blue. The measured NBW is determined by a single pole roll-off fit to the spectrometer measurement between an IF of 0.5 - 5 GHz.

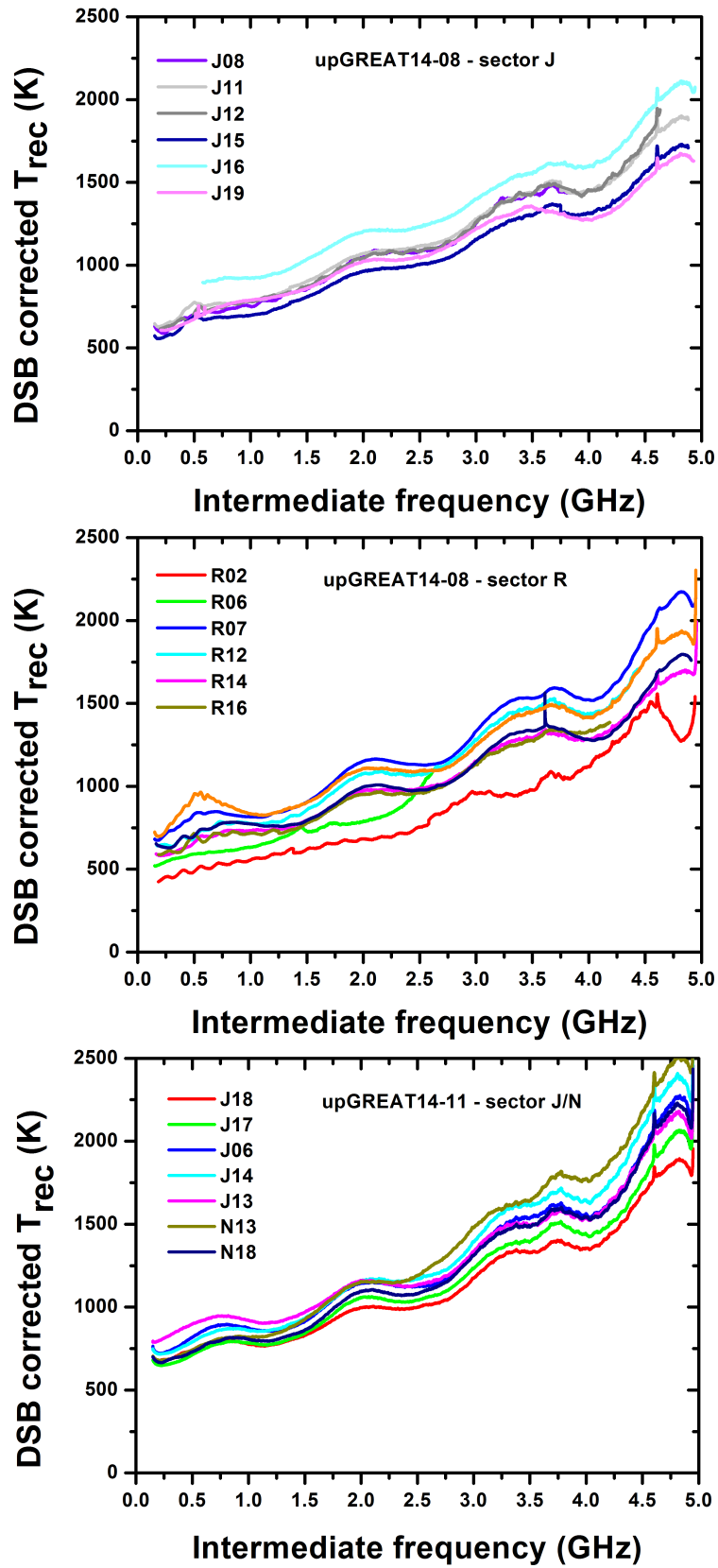


**Figure 66:** Receiver noise temperature as a frequency of IF corrected for the beamsplitter coupling. From top to bottom: wafer 14-08 sector J, sector R and wafer 14-11 sector J/N.

### 6.1.10 HEB Mixer Gain Bandwidth

To determine the mixer gain (and noise temperature) as a function of IF, the gain and noise temperature of the IF chain need to be known. To determine the gain of the total IF-chain as a function of the IF the spectrometer measurements have to be calibrated with a power-meter. The spectrometer gives as an output counts per channel which has to be translated to power in  $\mu\text{W}$ . The power meter averages the complete power of the IF band which is defined by a low pass filter (LPF). The LPF of the old chain is a filter with cutoff frequency of 1.45 GHz and 2.46 GHz for the new chain.

The XFFTS readout software cuts away the first 300 MHz. To estimate the missed power from the lower frequencies, I used a measurement from the main setup where the data are not reduced. The ratio from the total counts in the first 300 MHz in comparison to the full bandwidth of the low pass filter is about 3 % ( $6 \cdot 10^{15} / 2 \cdot 10^{17}$ ). Due to the degradation of gain from the amplifiers the contribution to the total power is low. So this small effect will be neglected for the power estimation. The reference for the measured power over the band is the power meter result. Here the absorbed power is averaged over the entire band. The averaged count number per channel can be determined by the integration of all counts from all channels in the band of the LPF (in total 28312). The total number of counts and the detected power level for the measurement at between 7.5 - 22 K are listed in Tab. 10:

temperature (K)	power (PM) ( $\mu\text{W}$ )	counts (SM) $10^{14}$	variable attenuation for SM (dB)
7.48	57	2.31	2
8.06	59	2.39	2
8.65	62	2.48	2
11.19	73	2.95	2
15.10	88	2.78	3
22.05	116	2.89	4

**Table 10:** The power level and total count number measured at various load temperatures. In addition the attenuation levels for the counts are listed. All measurements are amplified by 3 dB due to a reduced -3 dB attenuator for the calibration.

The power level and the counts have to be corrected for different attenuator settings. In addition -3 dB for all calibration measurements due to a removed attenuator. The power can then be calculated by a linear interpolation of the power meter level and the averaged spectrometer counts per channel. The interpolation and the data are shown in Fig. 67.

The counts can be interpolated by:

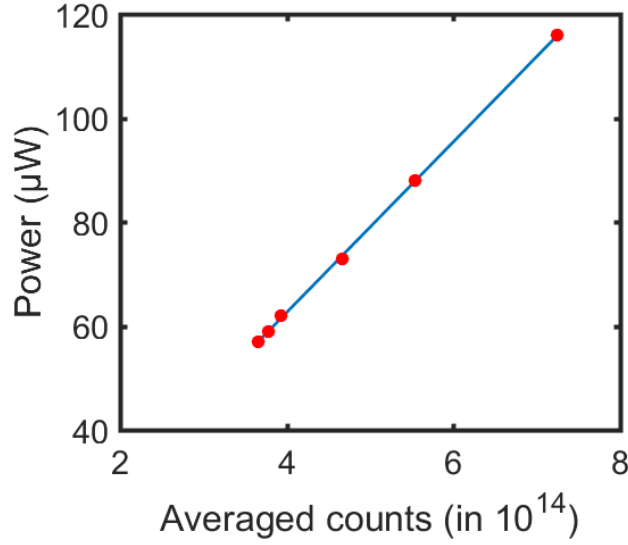


**Figure 67:** Power meter level as a function of averaged count from the XFFTS. The linear interpolation shows that the neither that power meter or the spectrometer is saturated.

$$P_{out}(W) = (1.641 \cdot 10^{-13} \cdot P_{out}(counts) - 3.02) \mu\text{W}, \quad (47)$$

where the power  $P_{out}$  is calculated in W and  $P_{counts}$  is measured in counts. None of the measurements were saturated because the IF output power is linearly dependent on the number of counts. The output power of the IF chain depends on the IF gain and is given by:

$$P_{out} = k_B T B G_{IF} + k_B T_{IF} B G_{IF}, \quad (48)$$

here  $k_B$  is the Boltzmann constant, T the temperature of the load,  $T_{IF}$  noise temperature of the chain, B the bandwidth and  $G_{IF}$  gain of the chain.  $T_{IF}$  is determined by a Y factor measurement (see Sec. 2.5) on the IF chain with two different input load temperatures. The gain, then can be determined from:

$$G_{IF}(f) = \frac{P_{out}(f)}{k_B B (T + T_{IF}(f))}. \quad (49)$$

The IF gain as a function of IF is shown in Fig. 68.

The mixer gain can be determined by Eq. 42. The results for a typical mixer is shown in Fig. 69.

The gain data between 0.5 and 2.5 GHz are well calibrated. Below 0.5 GHz all amplifiers in the IF chain loose gain rapidly. Above 2.5 GHz the IF chain has a different path with other attenuator settings. The calibration is only done for the lower frequency part because

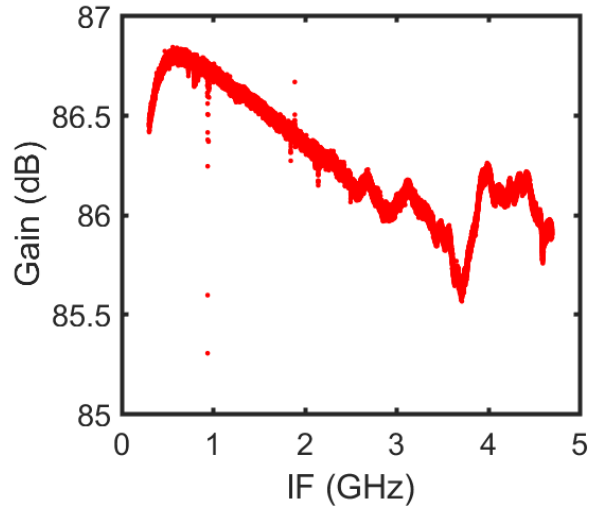


**Figure 68:** The gain of the new IF chain in dB as a function of the IF.

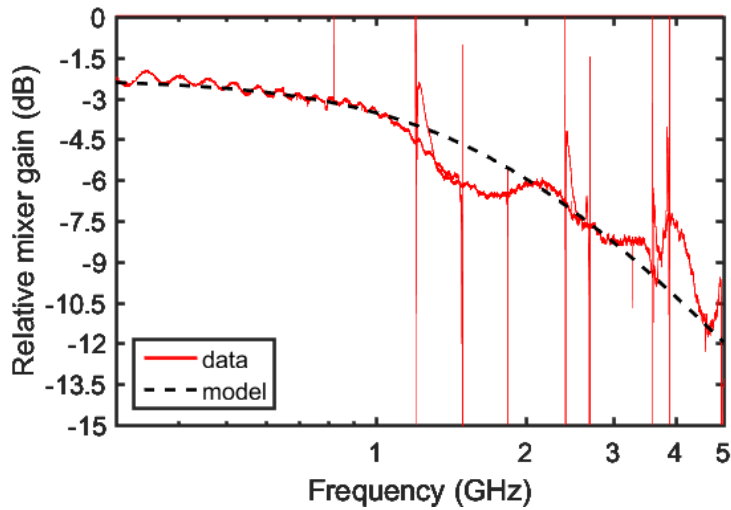


**Figure 69:** Relative mixer gain of device J19 from wafer 14-08 as a function of the IF. Data fitted with a single pole roll-off fit.

the gain bandwidth of the mixer is lower than 2.5 GHz. The IF gain bandwidth of these mixers is about 1.6 (- 0.1 / + 0.2) GHz for the wafer 14-08 and 14-11. The gain bandwidth for the set of LFA mixers are plotted in Fig. 70.

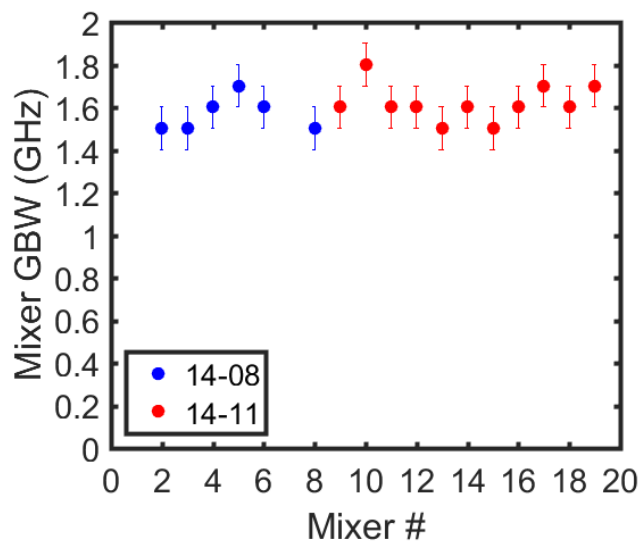


**Figure 70:** Mixer gain bandwidth (GBW) in GHz, for the set of 19 mixers plotted against in the order of the measured mixer.

### 6.1.11 Local Oscillator Power Requirement

The required Local Oscillator (LO) power is estimated based on two methods presented in Sec. 5.3.

The incident LO power is estimated by the measured grid angle  $\Theta$  of an attenuator wire grid. The results for a set of studied mixers is shown in Tab. 11.

wafer	sector	number	$\Theta$ ( $^{\circ}$ )
13-05	N	15	47.5
14-08	R	19	64.4
14-08	R	07	64.9
14-08	R	16	62.5
14-08	R	14	62.4
14-08	J	11	58.3
14-08	J	16	55.3
14-08	J	12	56.0
14-08	J	08	54.3
14-08	J	15	55.2
14-11	J	06	73.5
14-11	J	18	71.2
14-11	N	13	70.6
14-11	N	07	69.6
14-11	J	14	69.2
14-11	J	16	69.0
14-11	N	03	67.0
14-11	J	13	68.3
14-11	R	03	79.0
14-11	N	19	68.5
14-11	N	17	73.0

**Table 11:** Wire grid coupling angle  $\Theta$  in degree for device from wafer 13-05/14-08/14-11

In addition, the LO power is estimated with the isothermal method explained in Sec. 5.3. The results of both methods are presented in Fig. 71. The LO power for optimal operation of both methods is shown as a function of the critical current. The difference between the estimated optimum LO power by both methods is significant. Devices of all wafers show a variation of the required LO power dependent on the position of the wafer. The LO power followed empirically seems to follow the critical current as presented in Fig. 71.

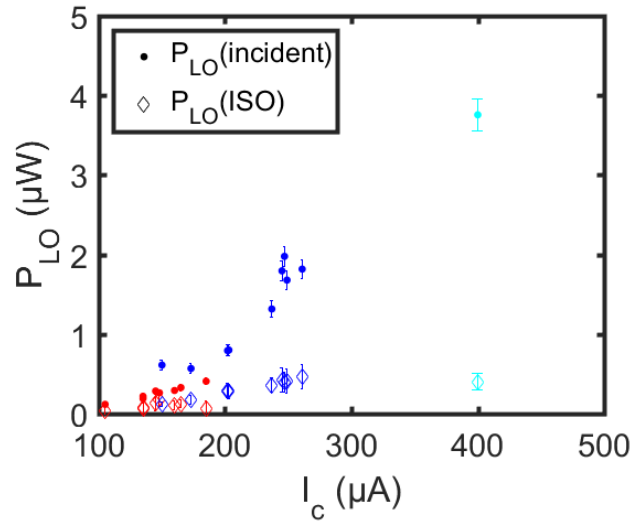


**Figure 71:** Measured required LO power as a function of the critical current ( $I_c$ ). The incident LO power measured with the attenuator grid is shown in circles and the LO power of the isothermal method is shown in diamonds. In total 19 mixers measured from three wafers: 13-05 in cyan, 14-08 in blue, 14-11 in red.

To estimate the typical dynamic range of the incident LO power with a margin of about 10 % of the receiver noise temperature a LOPS measurement was used. LO power which is coupled to the HEB was estimated by the angle of the rotating attenuation grid (see Sec. 5.3). The receiver sensitivity as a function of the incident LO power is shown in Fig. 72 for a mixer from wafer 14-11. The stable operation range (noise temperature within a variation of 10 %) for this mixer is between 0.62 and 0.85  $\mu\text{W}$  of incident LO power. This corresponds to the LO power deviation of  $\pm 15\%$ .

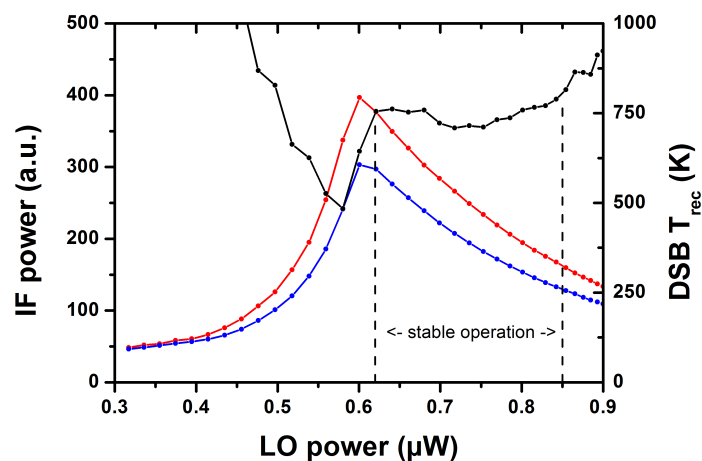


**Figure 72:** IF power for the hot and cold load as a function of the input LO power with the receiver noise temperature on the secondary axis. The stable low noise temperature operating LO power is between 0.62 and 0.85  $\mu\text{W}$

## 6.2 Silicon Inlay Waveguides

The metal waveguide manufacturing, especially for multi pixel arrays with decreasing dimensions for higher frequency is an issue. The mechanical tolerance can only be fulfilled with elaborate effort, but for an array the fabrication of a series of similar waveguides remains a challenge. Structures in the order of less than 100  $\mu\text{m}$  require a tolerance which is close to the mechanical tolerances of the machines. Another approach for the waveguide structures is the concept of a silicon micro-machining [84]. The silicon can be used as base material for the waveguide where the waveguide is etched into the silicon by deep reactive ion etching (DRIE) technology. The waveguide is then gold plated with a 1  $\mu\text{m}$  layer. The silicon waveguides can then be used as an inlay for a conventional a metal mixer block (see Fig. 73).

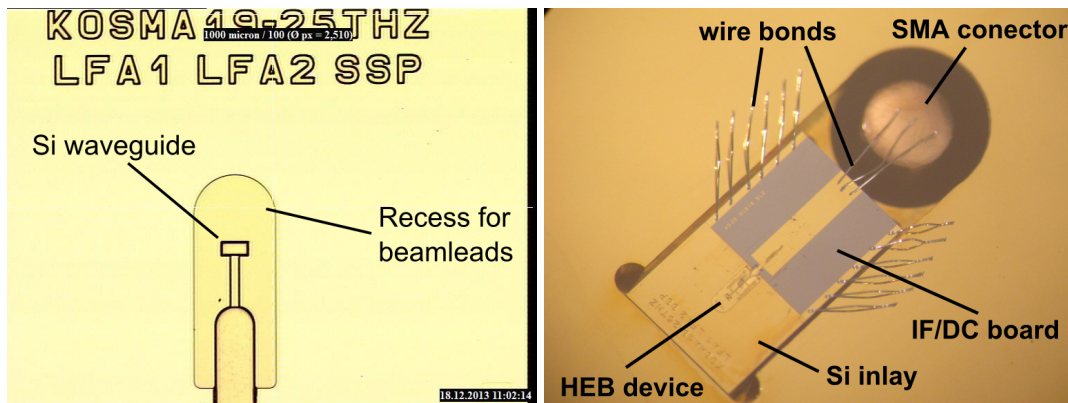


**Figure 73:** Left: gold plated LFA silicon inlay. Right: silicon inlay block with a assembled device.

At 1.9 THz, a prototype of the Si inlay block was fabricated and measured. The device which is assembled to the Si waveguide block is device J01 from the wafer 14-08. This device is from one of the sectors which are used for the upGREAT array. The FTS response of this mixer in comparison to a typical metal block mixer is shown in Fig. 74. Both FTS responses are similar to each other. The  $T_{rec}$  of device J01 is about 20 % higher as that of a similar device in a typical metal waveguide block.

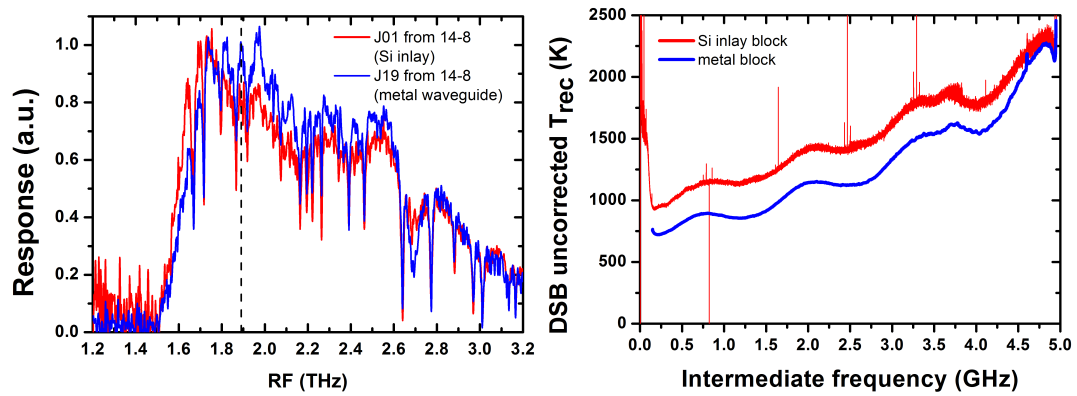


**Figure 74:** Left: FTS response for a typical metal block mixer in comparison with the first Si inlay block mixer (device J01 wafer 14-08). Right: DSB receiver noise temperature as a function of IF in GHz for a LFA mixer with the same Si inlay waveguide.

### 6.3 A 1.9 THz NbTiN HEB Mixer

The first measured phonon cooled HEB mixers in our lab were based on NbTiN which was used for the mixers in the single pixel receiver channels L1 (1.4 THz) and L2 (1.9 THz) of GREAT. One NbTiN HEB mixer was characterized in the same setup which is used in this work for comparison. The mixers were fabricated for the GREAT 1.9 THz single pixel receiver and for the STO project [54] [21]. This device is based on the material combination of NbTiN as the superconducting HEB bridge on a  $\text{Si}_3\text{N}_4$  substrate. The NbTiN bridge size is  $0.4 \mu\text{m} \times 3.1 \mu\text{m}$  with a thickness 4.5 nm. The  $\text{Si}_3\text{N}_4$  substrate has a thickness of  $2 \mu\text{m}$ . A microscope image of the device built into the mixer block and an image of the complete mixer unit is shown in Fig. 76.

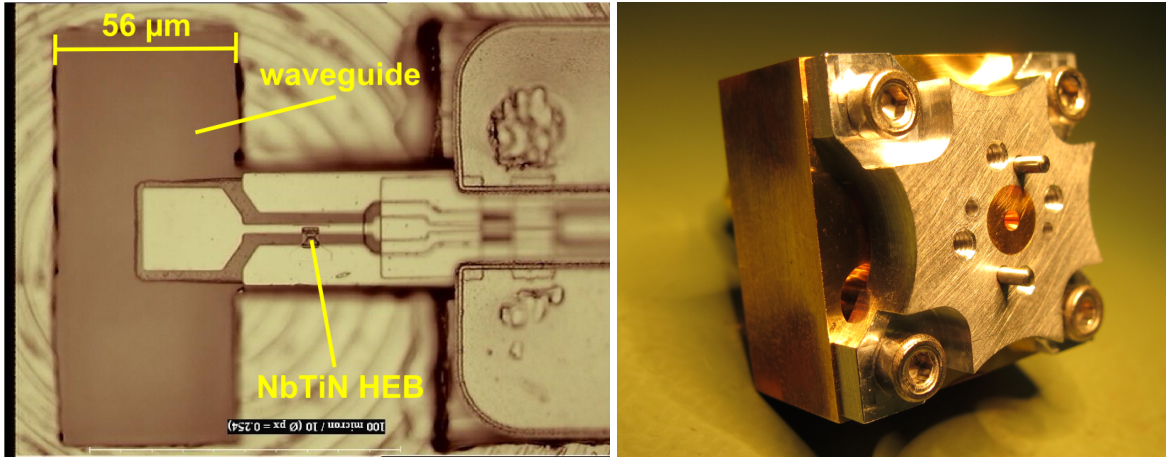


**Figure 75:** Left: Microscope image of a NbTiN device mounted in a mixer block. right: NbTiN mixer block assembled with a feed-horn clamp.

The DC I-V characteristics of the mixer shown in Fig. 76 are measured inside a liquid helium cooled cryostat. The critical current of this device is about  $220 \mu\text{A}$ . The R-T curve of this mixer is shown in right plot of Fig. 77. The critical temperature of the mixer is 7.9 K with a width  $\Delta T_c$  of 1.6 K.

At an under pumped LO power levels, the NbTiN HEB mixer device also has an unstable region at low bias voltages. The voltage sweeps (see Sec. 5.4.1) of two LO power levels are shown for a lower and a higher incident LO power in Fig. 77. By increasing the LO power, the unstable behavior vanishes. The required incident LO power for the optimal operation is about  $(0.5 \pm 0.1) \mu\text{W}$ . In the stable region the receiver noise temperature is about 1400 K.

The spectrally resolved measured receiver noise temperature measured with the AFFTS is shown in Fig. 78. The noise bandwidth of the mixer is about  $2.1 \text{ GHz} \pm 0.2 \text{ GHz}$ . Jiang et al. used NbTiN on a quartz substrate. They were able to achieve a noise bandwidth of 1.4

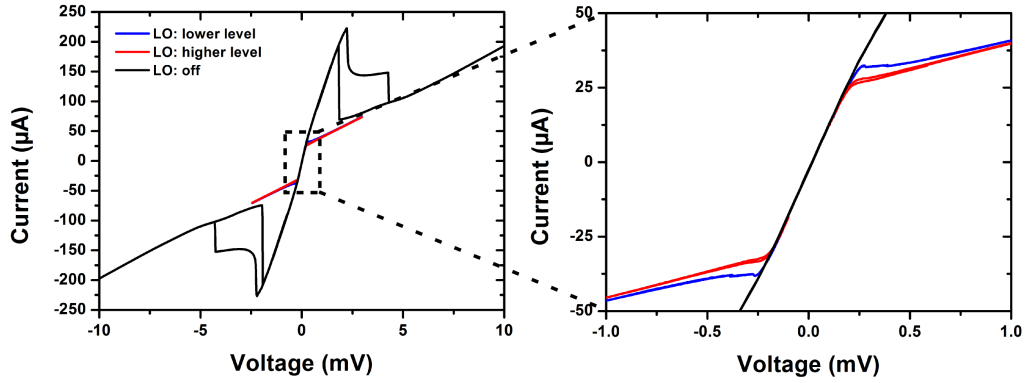


**Figure 76:** Left: IV curves of a NbTiN mixer for different LO input levels. Right: zoom on the inset of IV curves for the corresponding LO power levels.

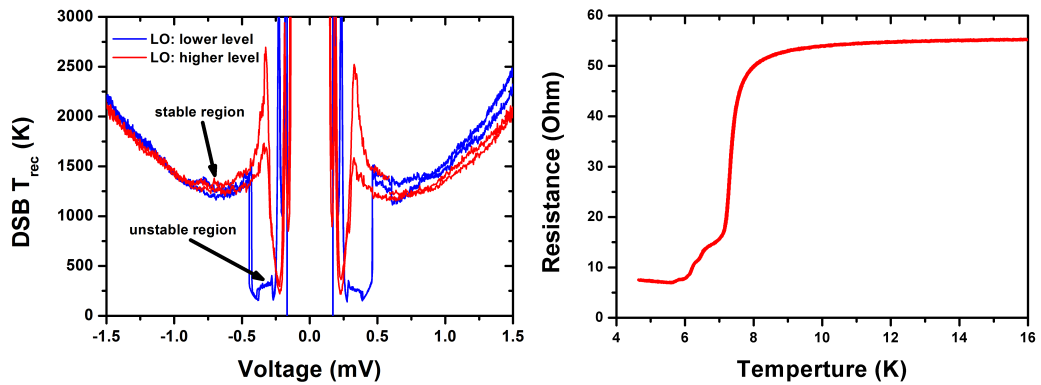


**Figure 77:** Left: DSB  $T_{rec}$  for two different LO power levels (unstable region vanishes with higher LO power). Right: RT curve of the HEB mixer with a  $T_c$  at 7.9 K.

GHz [85].

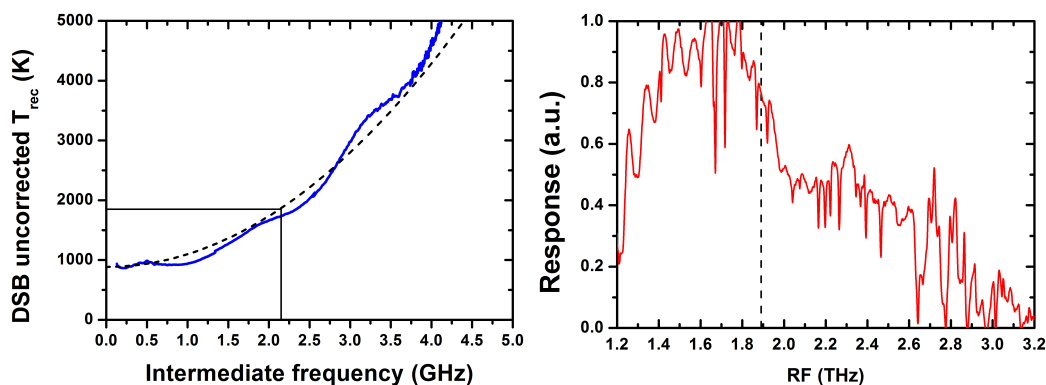


**Figure 78:** Left: DSB  $T_{rec}$  curve of a NbTiN HEB mixer. The noise bandwidth is determined by a single pole roll-off fit, plotted as the dashed line. The black lines indicating the noise bandwidth. Right: Power coupling as a function of RF frequency, measured with the FTS.

The mixer gain and noise temperature as the result from a LO power sweep (see 5.4.2) are presented in Fig. 79. The impedance mismatch of the NbTiN mixer is about + 0.2 dB, which is considered in the calculation of mixer gain and noise temperature. The mixer noise temperature at 1.5 GHz IF is in the order of  $500 \text{ K} \pm 50 \text{ K}$ . The gain at that operation point is  $-10 \text{ dB} \pm 1.0 \text{ dB}$ . A comparison between the performance of the NbTiN and NbN based HEB mixers is presented in Sec. 7.2.

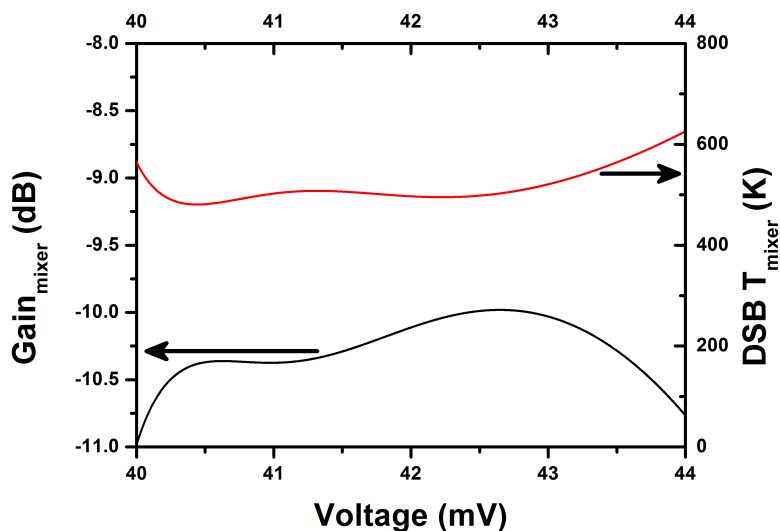


**Figure 79:** Mixer gain and DSB  $T_{mixer}$  (CW) of a NbTiN HEB mixer measured with the LOPS method.

## 6.4 4.7 THz GREAT H-Channel Mixer

The 4.7 THz mixer was developed for the GREAT H-channel [61]. It also serves as a prototype of the High Frequency Array (HFA) of upGREAT consisting of 7 mixers similar to the present mixer. The results of the two designs for the 4.7 THz HEB mixers, HFA-1b and HFA-3 (see Sec. 3.1.3), are presented in this section. The characterization of the 4.7 THz mixer is done in a similar way as the 1.9 THz [86] [22]. The setup differences in the 1.9 THz receiver system are described in chapter 4.3. The devices based of NbN film made from a different wafer than the LFA mixer devices. The wafer which is used for the 4.7 THz mixer is wafer 13-05 with film thickness of 4.5 nm and the length 300 nm of the HEB bridge. This larger volume of the film in comparison to the LFA wafers 14-11 and 14-08 corresponds to a higher LO power requirement for optimal operation which is not an issue due to the high power LO at 4.7 THz. The DC properties of the mixer are tested at first.

### 6.4.1 DC Properties

The DC properties are measured for a preselection of the best device before mounting into the mixer blocks. For the 4.7 THz device, two different designs were fabricated which have to be analyzed which are introduced in Sec. 3.1.3. In Fig. 80 the I-V and in Fig. 81 the R-T measurements form devices of the design HFA-1b before and after the mounting into the mixer blocks are shown. In Fig. 82 and Fig. 83 the DC results for the HFA-3 design are shown.

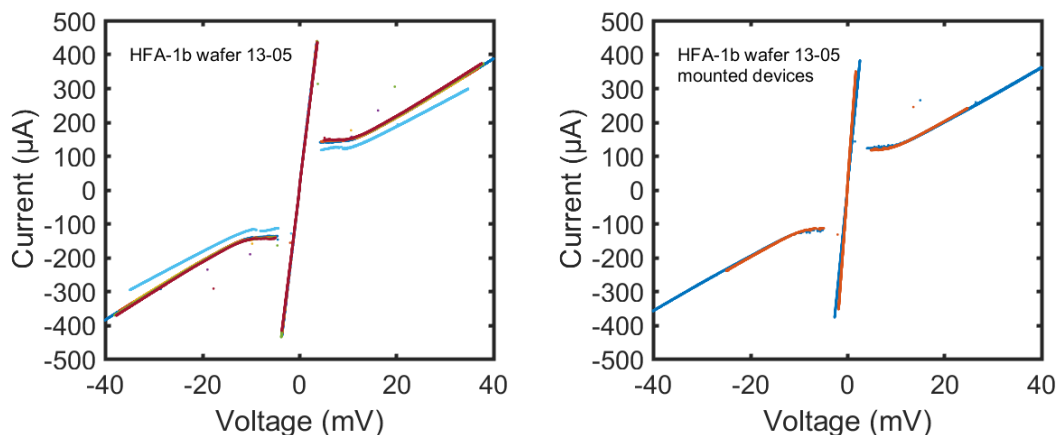


**Figure 80:** DC IV curve of the HFA-1b devices from the wafer 13-05 sector L. Left plot: pretested devices on the wafer. Right plot two tested mixers which were mounted inside the mixer block.

After the final fabrication steps and assembly of the mixer, the measured critical current is decreased from 450  $\mu\text{A}$  to about 400  $\mu\text{A}$ . The typical  $T_c$  decreases from 9.3 K to 8.9 K.

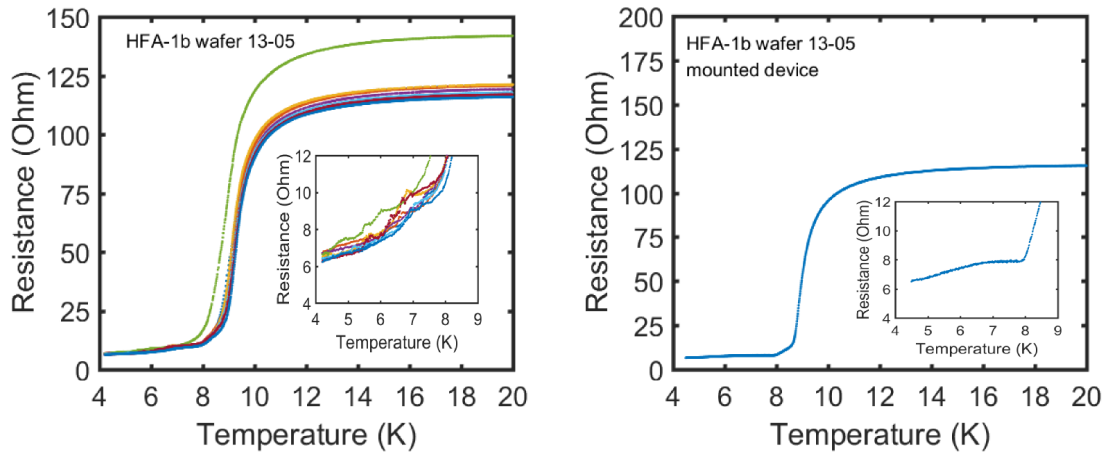


**Figure 81:** RT curve of the HFA-1b devices from the wafer 13-05 sector L. Left plot: pretested devices on the wafer. Right plot showed a tested mixer which was mounted inside the mixer block.

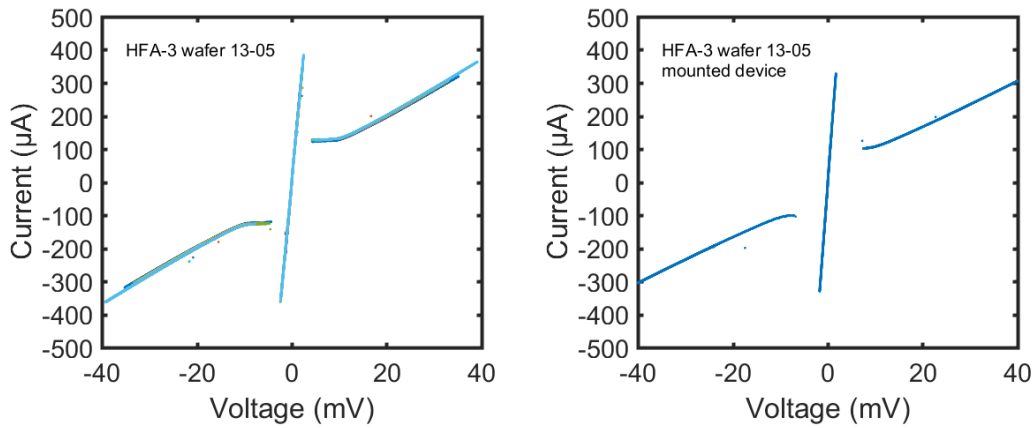


**Figure 82:** DC IV curve of the HFA-3 devices from the wafer 13-05 sector L. Left plot: pretested devices on the wafer. Right plot showed a tested mixer which was mounted inside the mixer block.

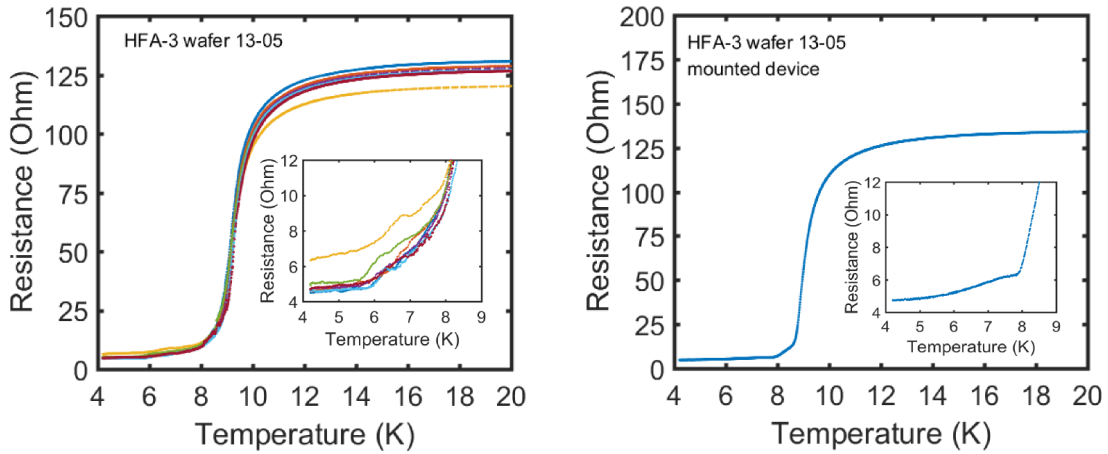


**Figure 83:** RT curve of the HFA-3 devices from the wafer 13-05 sector L. Left plot: pretested devices on the wafer. Right plot one tested mixer which was mounted inside the mixer block.

Both designs have the same device volume, but they differ with respect to the RF and IF circuit design (see Sec. 3.1.3).

#### 6.4.2 FTS Response

The RF broadband response for the two different HFA designs are shown in Fig. 84. The first design HFA-1b is based on the circuit without capacitors with a dielectric layer on top of the IF output line to avoid potential losses in the 400 nm thick SiO<sub>2</sub> dielectric of unknown RF characteristics. The disadvantage is a smaller RF bandwidth of 0.5 THz, which is not a problem for the measurement of the O line at 4.7 THz, if the measured mixer response is similar enough to the designed one. A comparison with simulated transmission from the waveguide to the NbN HEB film is shown in the left plot. The measured response is well in agreement with simulated response.

The second design HFA-3 is shown in the right plot. The main difference to the other design is the broadband RF response of about 2.5 THz. It is based on the design from LFA and required the additional dielectric material. The simulation follows well the measured response. In both cases the response at the lower frequency edge of the band is reduced, which is probably due to the cut off frequency of the real waveguide.

The RF response of the HFA-3 mixer was changed after the second cool-down. After the first measured FTS response, the studied mixer was extracted from the one test-dewar and assembled into another one of the heterodyne measurements. After the determination of the LO power consumption and the noise temperature at 4.7 THz, which were both significantly higher than expected the FTS measurement was repeated. The RF band was shifted by 0.5

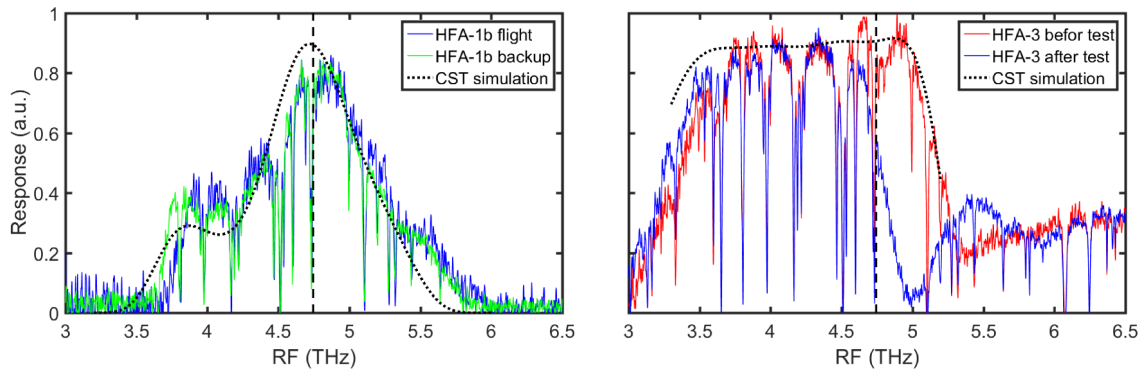


**Figure 84:** Response in arbitrary units measured as a function of RF with a FTS. Top plot results of the HFA-1b design and bottom HFA-3 design. Dotted line represents the CST simulation and the dashed line the frequency of the oxygen line. The HFA-3 response changes over time.

THz, which results in a decrease of  $1/3$  from the original value. After dismantling of the horn clamp on top of the mixer an obvious mechanical failure was found. The device was shifted by  $5 \mu\text{m}$  towards the channel (see Fig. 85), by thermal cycling or by (rough) handling the mixer (horn-mixer interface). This CST simulation of a shift in this direction, causing significant shift in the RF band.

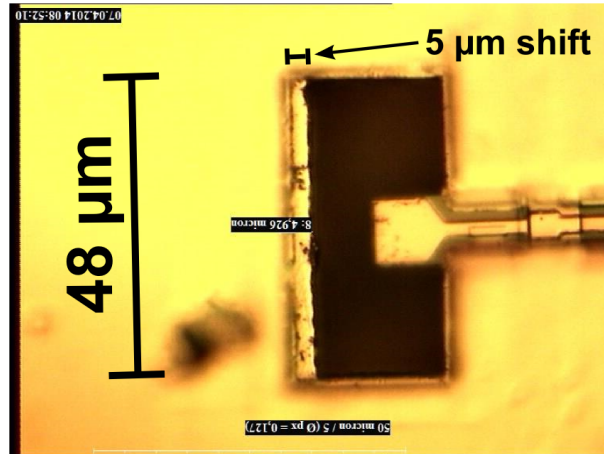


**Figure 85:** Microscope image of the  $5 \mu\text{m}$  shifted HFA-3 device mounted in the mixer block. Amplification of 1000.

### 6.4.3 Mixer Sensitivity

The heterodyne measurement for the H-channel at 4.7 THz mixers were measured in cooperation with the Max-Planck-Institut für Radioastronomie in Bonn. The LO for the 4.7 THz measurements is a quantum cascade laser (QCL) developed by the DLR-Pf [20]. At an

operation temperature of 45 K the QCL provides a total output power of about  $300 \mu\text{W}$  measured with a Golay-Zelle. The sensitivity is only measured for the HFA-1b design because the second HFA-3 design showing a failure during the measurement. The heterodyne setup for 4.7 THz is completely evacuated to reduce the high atmospheric transmission losses at 4.7 THz. The losses occur due to water vapor in the air. The beamsplitter which is used in the receiver is a  $3 \mu\text{m}$  thin Mylar foil. The calculated transmission of the foil is 0.835 at 4.745 including the absorption inside the foil. The estimated required LO power requirement with isothermal technique from Sec. 5.3 is about 400 nW. The dewar window is a Si wafer with micro-electro-mechanical machined AR grooving [87]. The measured transmission (with the FTS) of the window is 0.92 at 4.75 THz. The rest of the setup is equivalent to the setup which is used for the 1.9 THz. The IR filter is a same QMC filter type [69]. The transmission of the filter at 4.745 THz is 0.93. The IF spectrometer, which is used for these experiments is a combination of two eXtended bandwidth Fast Fourier transform spectrometers (XFFTS) with a bandwidth of 2.5 GHz each to cover instantaneous the complete band from 0 - 5 GHz [72]. The mixer sensitivity is first measured with a LOPS method (see Sec. 6.1.5). The results for the optimal bias conditions are shown in Fig. 86. The measured power curves are interpolated with a polynomial of 19th order. This interpolation is convenient to easily compare the measurement for the hot and cold load at the same pump current. On the secondary axis the uncorrected DSB  $T_{rec}$  is shown. The minimum of  $T_{rec}$  was about 980 K averaged over the IF band between 1.25 - 1.75 GHz.

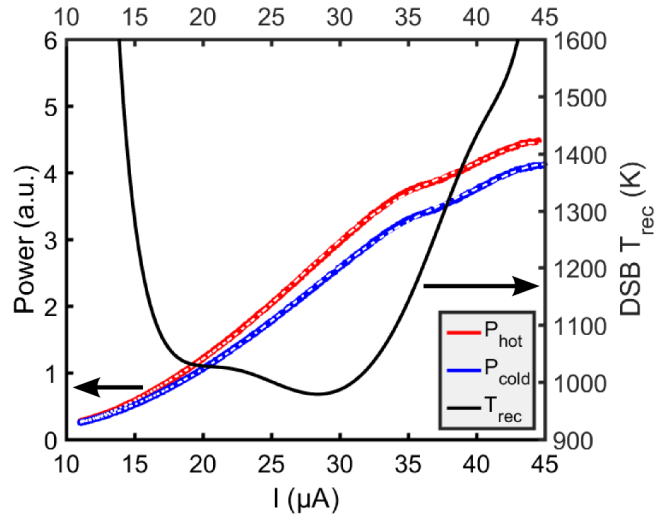


**Figure 86:** LOPS measurement at the optimal bias conditions. On the left axis the detected power from the hot and cold are plotted as a function of the bias current at a constant bias voltage of 1.25 mV. The secondary axis shows the DSB  $T_{rec}$ .

The investigation of the best bias point is done with a series of LOPS and spectrometer

measurements at different bias voltages. In addition the direct detection effect of this mixer is measured as explained in Sec. 2.4.1. In Fig. 87 the results for both the LOPS and the spectrometer measurements are shown. The repetition of the LOPS measurement of the different bias voltages presents the optimal bias voltage of 1.25 mV. A second set of measurements was made with the spectrometer [72], for the same bias voltages and then the results were averaged over the same bandpass of 1.25 - 1.75 GHz. The results are given in Fig. 87.

From Fig. 87 the direct detection can be calculated by the difference in  $T_{rec}$ . The averaged direct detection over all bias points is 10 % for this mixer. The  $T_{rec}$  values for the spectrometer measurements are overestimated by 10 %.

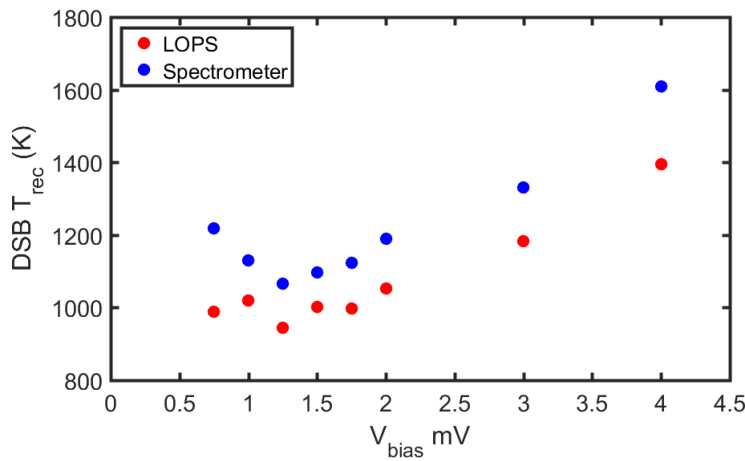


**Figure 87:** Comparison of the averaged (1 -2 GHz) DSB  $T_{rec}$  measured with LOPS and spectrometer. DSB  $T_{rec}$  is measured as a function of the bias voltage between 0.7 - 4.0 mV.

#### 6.4.4 IF Noise Bandwidth

The receiver noise bandwidth (NBW) for the 4.7 THz receiver based on the previously described mixer is calculated from the measurements of FFTS. Here we used Eq. 46 for the calculation of the NBW. The NBW of the mixer is approximately 3.7 GHz with a  $T_{rec}(0 \text{ GHz})$  of 900 K.

#### 6.4.5 4.7 THz Mixers Conclusions

The 4.7 THz HEB coupling measurement with the FTS is an excellent agreement with the design of the circuits in CST (see Fig. 84). For device type HFA-1b the frequency of the oxygen fine structure line sits in the center of the response peak. In a first test a device of

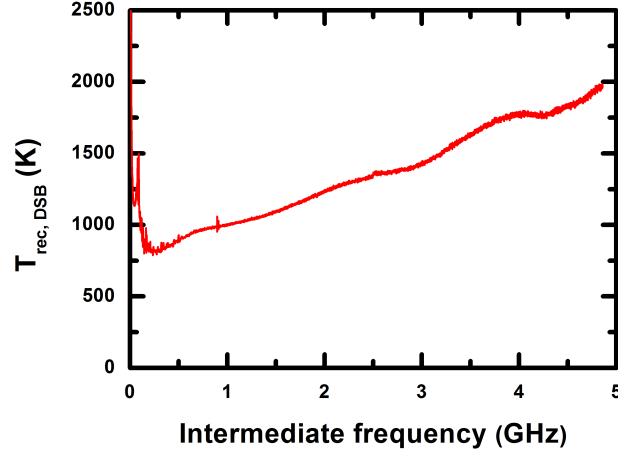


**Figure 88:** The DSB receiver noise temperature as a function of IF in GHz for mixer from the HFA-1b design.

the HFA-3 design showed a shift of the horn position after assembly in the receiver at the MPIfR (see 6.4.2). This resulted in a weak coupling and bad sensitivity at the frequency of the oxygen fine structure line. We therefore decided to concentrate on the deployment of the HFA-1b designs, because of the pressing delivery time for GREAT. The performance of the mixer from the HFA-1b design is comparable to the 1.9 THz mixers. The noise temperature is similar, which indicates a superior RF design. The 4.7 THz mixer is only 8 times the quantum limit ( $\frac{hf}{2k_B}$ ) which is comparable to the result of Kloosterman et al. [51]. The noise bandwidth of a typical low frequency mixer is about 10 % higher than this mixers, due to the different NbN film thickness of wafer 4.5 nm in comparison of 3.5 nm for LFA. The reduction of the film thickness leads to increase of the bandwidth predicted by the lumped element model.

The stability of the H-channel of GREAT, operating with a single mixer at 4.7 THz, is not limited by the mixer but mainly determined by the noise of the QCL[88]. A spectroscopic Allan time of about 80 s determined in heterodyne setup at the MPIfR [22]. The measured sensitivity at the MPIfR [22] is similar to the results at SOFIA.

## 6.5 HEB as a Characterization Tool for Local Oscillators

A HEB mixer can also be used as a tool for the characterization of a local oscillator [89]. I did these measurements together with M. Justen who built the QCL LO. Therefore, we used the receiver system in two configurations with the same components except for the LO. The first LO is a commercial AMC from VDI [68] with a multiplication of 144. It is tunable from 1.8 to 2.0 THz. The output power of the typical operating frequency of 1.89 THz is 23  $\mu\text{W}$ . Its operation temperature of the LO is room temperature. The second LO is a

quantum cascade laser (QCL) [82]. The LO is embedded into a waveguide split block with a micro-strip to rectangular waveguide transition. The horn design of the output design is same as the VDI horn. The maximum output power at an operating frequency of 1.98 THz is  $650 \mu\text{W}$  (at an operation temperature 20 K). A second operation mode at 1.88 THz with an output power of  $90 \mu\text{W}$  is also available.

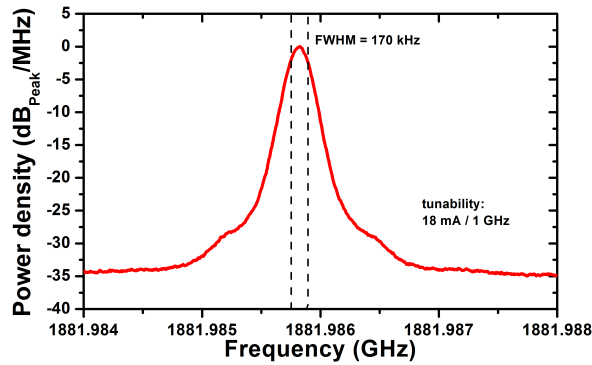


**Figure 89:** QCL power density in dB/MHz of the peak as a function of frequency.

At the first step we made a beat experiment to determine the output of the frequency of the QCL. The VDI AMC is used as the LO. The QCL signal is used as a signal in the spectrum. Therefore, its power has to be attenuated to prevent saturation of the spectrometer due to the strong QCL signal. The result is shown in Fig. 89.

### 6.5.1 Characterization of the QCL

The heterodyne performance of the mixer using both LO subsequently in the same setup is measured. The result of an IF spectrometer measurement from 0-5 GHz IF is shown in Fig. 91. Due to the different LO output power levels of both sources, different beamsplitters are used for the two measurements. To compare the two measurements, the beamsplitter coupling is corrected in the receiver noise temperatures.

The QCL LO introducing spurs at the IF band between 0-1 GHz, the most sensitive part of the receiver system. These spurs are an issue for observation of astronomical lines. The investigation of spurs is done at a frequency of 4.7 THz using a different mixer and QCL. At this operation frequency the similar spurs in the lower IF between 0 - 1 GHz. By introducing a 4.7 nF NPO capacitor between the current source and the ground the amplitude of the spurs was significant reduced (see Fig. 47).

The sensitivity of the receiver system using a QCL or a AMC LO is similar. The QCL

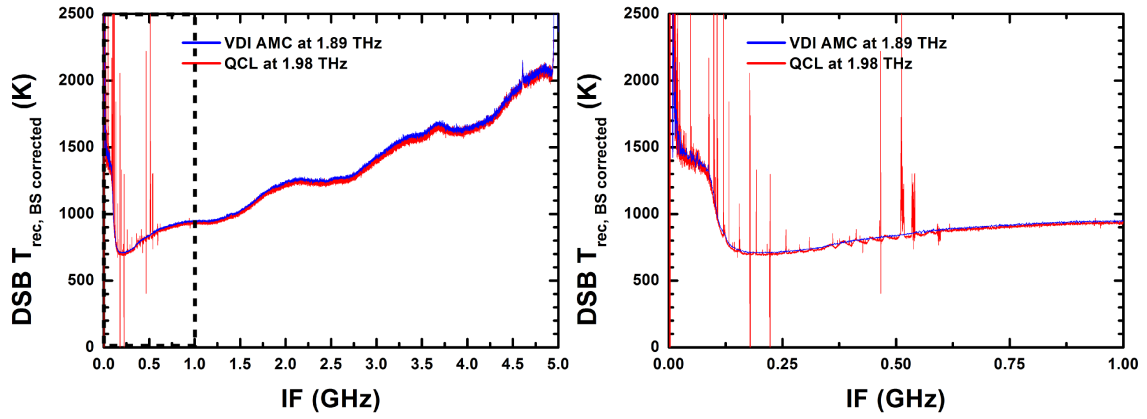


**Figure 90:** Left: Comparison of a heterodyne measurement corrected for the beamsplitter coupling for the AMC and QCL LOs. The receiver noise temperature using the different LOs is similar. Right: Zoom in on the IF between 0 - 1 GHz. The main difference are the spurs in the IF.

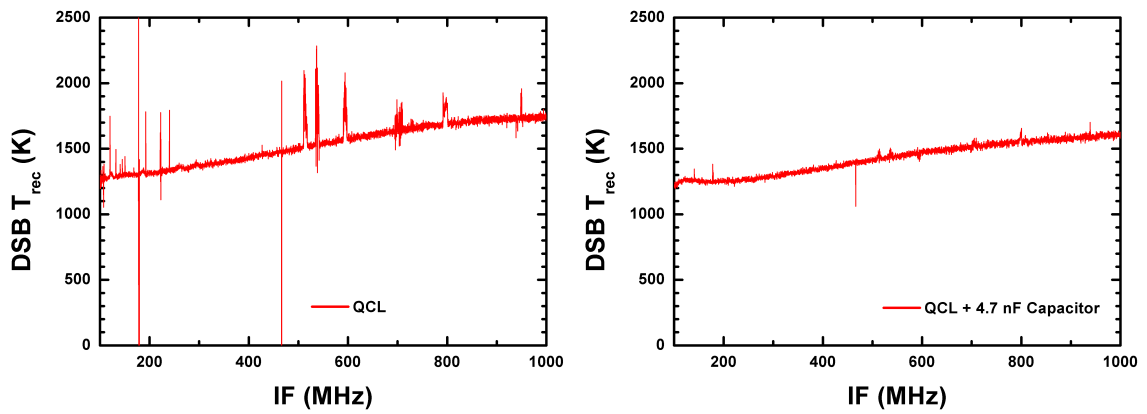


**Figure 91:** A Heterodyne spectrum with reduction of the spurs by using the QCL with or without an additional capacitor at the DC current source of the QCL.

can be used as the LO for observations. And the AMC LO does not add additional noise compared to a QCL. The only major issue of the QCL remains the tuning of the RF output frequency, which has to be solved for broadband applications.

## 7 Discussion of the 1.9 THz Measurement Results

In this section, the comparison between the theoretical models and the measured data with the main focus on the 1.9 THz mixers for the array application are presented. In addition, comparison of the performance of NbN and NbTiN based HEB mixers, followed by an interpretation of the results of the 4.7 THz measurements, are shown.

### 7.1 HEB Mixers Based on NbN

A large number of measurements (for 34 mixers) of the Low Frequency Array (LFA) mixers facilitates a statistical analysis of the results. For 19 out of the 34 measured mixers, a complete set of data is used for the analysis. During this thesis probably the largest number of HEB mixers was characterized and should provide a better insight into the correlation of measured DC selection and RF mixer performance characteristics. In addition, measurements of mixers from different wafers increase the variety of the mixer properties under study. It appears that the performance of the mixers from the same wafer is more similar than the performance of mixers from different wafers, with the same nominal properties. The focus in this comparison between the wafers is about the mixer noise, mixer gain, the instantaneous intermediate frequency bandwidth and LO power requirement.

After the integration of the mixers into the upGREAT channel, the performance was studied for the sensitivity and stability. The LFA channel of upGREAT is showing a similar sensitivity to the measured results in our heterodyne setup [24] [88]. Furthermore, the stability of the mixers, which based on the thinner NbN film with the slightly worse superconducting properties ( $T_c$  is reduced by 1 K), are enough to observe on SOFIA [24] [88].

#### 7.1.1 DC Characterization of NbN HEB Mixers

In the R-T curve of the NbN based mixers, two superconducting transitions can be observed at  $T_c$  and shortly below  $T_c$ . A plateau of approximately constant resistance is observed between these transitions. In [90] and [91] the area of the NbN close to the gold contact pads is identified as an intrinsic normal contact resistance at and below the critical temperature of the HEB. The resistance is caused by the proximity effect between the normal conducting gold and the superconducting NbN. Because the NbN is much thinner than the gold, the critical temperature of the ends of the NbN film is reduced, leading to an additional series resistance [81]. The additional step in the R-T curve arises from the proximitized part of the contact pads. The influence of the multiple  $T_c$  transitions on the mixer performance is yet unclear, but the obviously resistance contribution has a negative effect on the mixer

sensitivity [81].

The critical current measured in the DC IV-curve decreases after the separation and mounting for all (19) devices (6.1.1). The mean reduction of  $I_c$  for wafer 14-11 is  $(-100 \pm 30) \mu\text{A}$  and for wafer 14-08 is  $(-70 \pm 30) \mu\text{A}$  (see Fig. 92). The mean reduction of  $I_c$  is between 30 to 50 % (see Fig. 92). Due to the non-reproducible changes of DC characteristics on a run-to-run basis, a clear selection process of devices based on the dipstick IV characterization is not feasible.

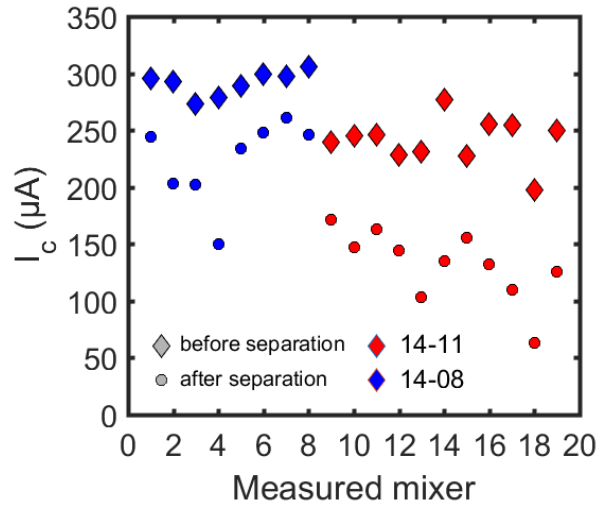


**Figure 92:**  $I_c$  of both wafers before the separation plotted as diamonds plotted against in the order of the measured mixer. The  $I_c$  after mounting is plotted as dots for both wafers (red 14-08 and blue 14-11).

The mean device resistance of the peak value (at a temperature of 25 K) and at 4.2 K after the separation and assembly of the mixers are listed in Tab. 12. In addition the measured resistance of the thin gold seed layer was measured to determined the loss of the gold layers of the circuit. We attribute the difference of the mixer resistance at 4.2 K to difference of the gold layers of circuits of both wafers.

wafer	$R_{peak}$ ( $\Omega$ )	$R_{4.2K}$ ( $\Omega$ )	$R_{test}$ ( $\Omega$ )
14-08	$133 \pm 2$	$13.7 \pm 0.1$	4.5
14-11	$155 \pm 5$	$11.9 \pm 0.6$	3.6

**Table 12:** Mean resistance of the mixers at 25 K, 4.2 K and the resistance of a test gold seed layer for wafer 14-11 and 14-08.

During the final processing steps  $T_c$  and  $I_c$  decrease compared to the values measured when the devices are still on the handle wafer (see plots in Fig. 48, 47, 49 and 50). The

average decrease in  $T_c$  and  $I_c$  is larger for batch 14-11 than for batch 14-08. More than one sector (see Sec. 3.2.1) of both wafers has been processed, so an incidental process error is not a likely explanation. Because the optimum LO power pump level of the devices of wafer 14-11 is about one-fifth (see Tab. 14) of that of devices of wafer 14-08 with the same volume. The ratio of the sheet resistance from wafer 14-11/14-08 is about  $0.91 \pm 0.03$  which can be interpreted by a thinner film (or a bad film quality).

### 7.1.2 THz Response

The measured broadband RF response of the mixers presented in Sec. 6.1.3 shows a similar THz frequency dependency for all 1.9 THz mixers. The low-frequency cut-off of the response is shifted to the lower frequency with respect to the design curve. This shift can be attributed to a larger waveguide width, of about  $+5 \mu\text{m}$ , at the end of the feed-horn where the horn contacts the mixer block. The comparison of the simulated response shown in Fig 53 with the measured results shows a discrepancy between 2 - 3 THz. For the upper-frequency range 2 - 3 GHz the RF response is reduced (Fig. 53). A similar behavior is observed with the older NbTiN/SiN designs [92] and the fundamental cause is still under investigation.

### 7.1.3 Estimate of the Optimum Local Oscillator Pump Power

An established method to estimate the required LO power is the isothermal method which is presented in Sec. 5.3. Another method of estimation of the required incident LO power is to determine the transmission from the LO output to the mixer input. This calculation is based on the assumption that the LO source has a constant output power (over time and frequency), as specified in the manual. This power will be reduced in the optical path using a rotatable wire grid, which is explained in detail in Sec. 5.3. The results of both methods of LO power estimation for all measured devices on the wafers 13-05, 14-08 and 14-11 are presented in Fig. 93. For further analysis, the wafer 13-05 was neglected because not enough data were available.

The experimental observation also shows that the LO power requirement depends on both  $I_c$  and  $T_c$ . Based on this observation the dependency of the LO power requirement on  $T_c$  and  $I_c$  is shown in Fig. 94. A clear dependency from the parameters ( $T_c$  and  $I_c$ ) can be observed.

Since  $T_c$  and  $I_c$  are both correlated with about equal uncertainty, in the following the critical current is examined as a measure for the LO power consumption. Especially for The measurement of many mixers for an array, the advantage of using  $I_c$  instead of  $T_c$  is that  $I_c$  is directly measured at 4.2 K, which is a routine measurement in the assembly procedure of

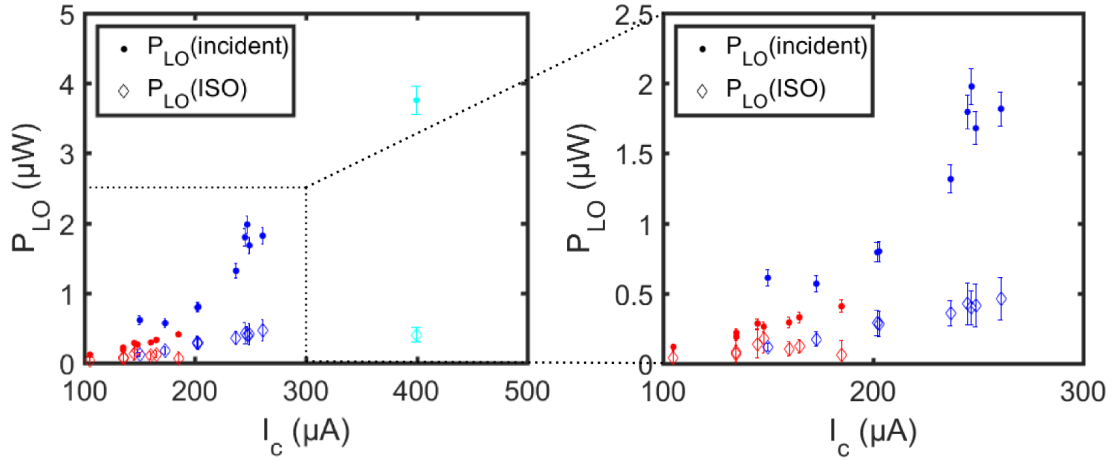


**Figure 93:** Measured required LO power as a function of the critical current ( $I_c$ ). The incident LO power measured with the attenuator grid is shown in circles and the LO power of the isothermal method is shown in diamonds. In total 20 mixers measured from three wafers: 13-05 in cyan, 14-08 in blue, 14-11 in red. The right plot is a zoom on the dotted square from left plot.

the mixer. To measure  $T_c$  instead, it is necessary to heat up the device slowly to check this device property. Once, the mixers are assembled in the array it is especially more efficient to measure the health status of the mixers via the  $I_c$ . For further analysis, the isothermal method is ignored because it is the incident LO power that is the relevant measure of the power consumption of a receiver.

### Empirical Dependency of the Optimum LO Power Consumption as Function of the Critical Current

During the investigation of the HEB device performance, a strong correlation of the critical current ( $I_c$ ) to the required  $P_{LO}$  power was observed. The data of the incident LO power versus critical current from fig. 93 with linear interpolation is shown in fig. 95.

The amount of  $P_{LO}$  which is needed for optimum operation appears to the first order to be linearly dependent on  $I_c$ . The slope of the fitted line and its ordinate seems to depend on the film properties and are varying from wafer to wafer. The results of the linear interpolation are listed in Tab. 14. The first observation is that the devices of the 14-08 wafer require more  $P_{LO}$  for the same  $I_c$  than devices of the 14-11 wafer. In addition, the  $I_c$  dependence of the LO power is steeper for 14-08 than for 14-11 (see Fig. 95).

I was able to predict empirically the required  $P_{LO}$  of a device of a certain wafer using the above linear interpolation based on a few measured mixers. For a new wafer, a measurement of two or three HEBs is sufficient for the predictions of the LO power consumption of the

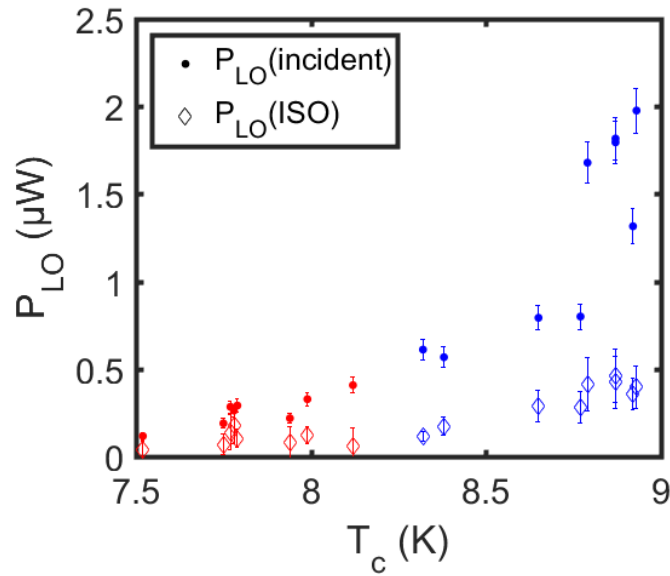


**Figure 94:** Measured required LO power as a function of the  $T_c$ . The isothermal methods is shown as diamond marker and the incident method with dots. The required LO power for wafer 14-08 in red and 14-11 in blue.

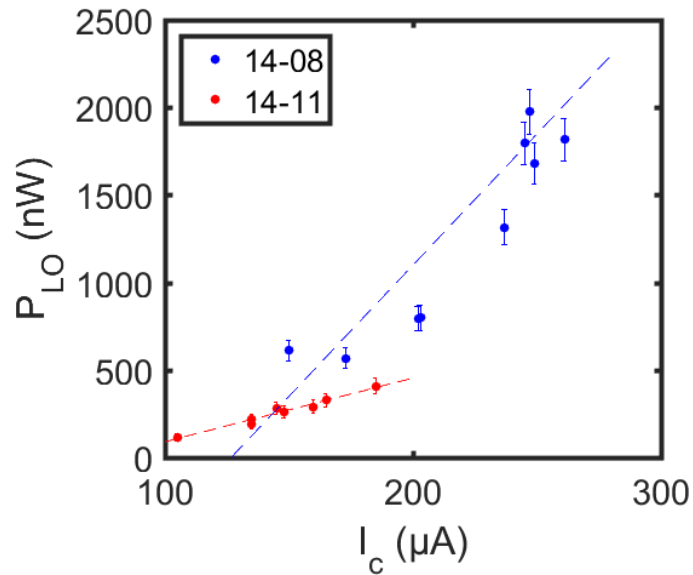


**Figure 95:** Measured required incident LO power in front of the mixer inside the dewar as a function of critical current for the wafers 14-08 (blue) and 14-11 (red). The dashed lines are linear interpolation of data points to guide the eye.

wafer	slope ( $\mu\text{W}/\mu\text{A}$ )	ordinate ( $\mu\text{W}$ )
14-08	$0.0137 \pm 0.0007$	$-1.74 \pm 0.16$
14-11	$0.0036 \pm 0.0001$	$-0.274 \pm 0.016$

**Table 13:** Linear regression of the incident LO power as a function of  $I_c$

other mixers. It would be efficient if a model based on only DC measurements could be used to predict the required  $P_{LO}$  power. Cherednichenko et al. propose that the product of the volume and the critical current density is a good measure of  $P_{LO}$  [62]. Consequently, the wafers with smaller HEB bridges should have a lower LO power requirement. The reduction of the volume from the wafer 13-05 to the wafers 14-08 and 14-11 indeed significantly reduced the required  $P_{LO}$ . On the other hand both wafers 14-08 and 14-11 were manufactured with identical fabrication processes and process parameters (e.g. sputtering time) and have a quite different LO power consumption. The average measurement results of the wafers are listed in Table 14.

wafer	thickness nm	length nm	width $\mu\text{m}$	$\overline{T_c}$ K	$\overline{I_c}$ $\mu\text{A}$	$\overline{P_{LO}}$ $\mu\text{W}$	*
13-05	$4.5 \pm 0.5$	$300 \pm 30$	$3.60 \pm 0.10$	$9.2 \pm 0.2$	$440 \pm 40$	4.5	1
14-08	$3.5 \pm 0.5$	$200 \pm 30$	$3.05 \pm 0.10$	$8.8 \pm 0.2$	$215 \pm 50$	$1.5 \pm 0.3$	8
14-11	$3.5 \pm 0.5$	$200 \pm 30$	$3.05 \pm 0.10$	$7.8 \pm 0.2$	$130 \pm 20$	$0.3 \pm 0.1$	11

**Table 14:** Wafer 13-05/14-08/14-11 mean comparison: Volume,  $T_c$ ,  $I_c$ ,  $P_{LO}$ . Bath temperature during the  $I_c$  and  $P_{LO}$  measurements: 4.5 K. The errors are calculated by the standard error of the mean. \*Number of the averaged mixer.

The measurements of the wafers 14-08 and 14-11 show that not only  $I_c$  and the volume seem to determine  $P_{LO}$ , but that each film in addition has its own characteristics. For the same NbN film (meaning of one wafer), in general a device needs more  $P_{LO}$  with increasing  $I_c$  a device. The LO power requirement can still vary dependent on the position of the wafer from sector to sector on the same wafer. In my measurements, this variation was smaller than the variation between the 2 nominal identical wafers. At the moment this inhomogeneity restricts the creation of much larger arrays. Further analysis of the difference of wafer 14-08 and 14-11 is done in the next section. The goal is to predict the LO power consumption theoretically, only based on DC measurements.

## Theoretically Estimated Local Oscillator Power Consumption

To be able to give a prediction of the required incident  $P_{LO}$ , without measuring a large set of mixers, the heat balance equation (see Eq. 8) is studied. Using the uniform heating model for the heat balance equation the required  $P_{LO}$  is given by [40]

$$P_{LO} = \frac{\gamma}{n \cdot \tau_{\Theta}} \cdot V \cdot (T_c^{n-1.6} - T^n / T_c^{n-2} - n \cdot T_c^{n-2.6} \cdot \Delta T_c), \quad (50)$$

where  $\gamma$  is Sommerfeld constant,  $V$  is the volume of the film,  $T$  is the bath temperature,  $T_c$  is the superconducting transition temperature,  $\Delta T_c$  the transition width of the superconducting transition,  $\tau_{\Theta}$  the thermal time constant and  $n$  a material constant (see Eq. 7) [40]. The ratio of  $\frac{\gamma V}{\tau_{\Theta}}$ ,  $n$ ,  $T_c$  and  $\Delta T_c$  should describe the difference between the wafers.

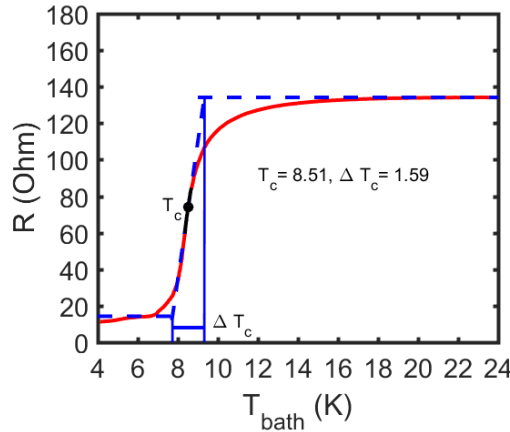


**Figure 96:** Resistance of a HEB mixer as a function of bath temperature. The dashed lines showing the definition of  $\Delta T_c$ . The two cross points of the slope at  $T_c$  with the horizontal lines of the approximately constant at the peak (at a temperature of about 25 K) and at the 4.2 K defines the width of the transition. The offset at 4.2 K, which is attributed to the gold circuit leads, is subtracted.

$\Delta T_c$  is determined from measurements of the  $T_c$  transition (see Fig. 96). In the broken line transition model [40],  $\Delta T_c$  can be determined by the slope at  $T_c$  (see Fig. 96). The results are listed in Tab. 15.

According to [93] and [52] the exponent  $n$  can be derived by measuring the normalized  $T_{rec}$  as a function of bath temperature ( $T_{bath}$ ). Under the assumption that  $P_{DC}$  is significantly smaller than  $P_{LO}$  according to the heat balance Eq. 8  $P_{LO}$  is proportional:

$$P_{LO} \propto T_c^n - T_{bath}^n \quad (51)$$

The DC power level for a typical operating point is in the order of 30 - 40 nW. In comparison to  $P_{LO}$  the DC power is at least a factor of 10 smaller, even for the probably to

wafer 14-08				wafer 14-11			
sector	number	$T_c$ (K)	$\Delta T_c$ (K)	sector	number	$T_c$ (K)	$\Delta T_c$ (K)
R	19	8.31	1.59	J	06	7.52	1.81
R	16	8.65	1.64	J	18	7.75	1.77
R	14	8.75	1.48	N	13	7.94	1.92
J	11	8.95	1.45	N	07	7.78	1.91
J	16	8.87	1.50	J	14	7.75	1.70
J	12	8.79	1.37	N	03	8.12	1.61
J	08	8.93	1.46	J	13	7.99	1.52
J	15	8.94	1.38	R	03	7.41	2.12
				N	19	7.83	1.65
				N	17	7.56	1.75
				J	17	7.79	1.52
14-08	averaged	8.77	1.48	14-11	averaged	7.80	1.77

**Table 15:**  $T_c$  and  $\Delta T_c$  for set of 19 mixers of the wafers 14-08 and 14-11.

low estimate by the intersecting line method, see e.g. Fig. 94. Therefore the DC power can be neglected and the approximation of Eq. 51 be used.

The receiver noise temperature  $T_{rec}$  is equal to the mixer noise temperature  $T_{mixer}$  plus the IF noise temperature  $T_{IF}$  divided by the mixer gain  $G_{mixer}$ . There is also a contribution to  $T_{rec}$  from the optics in front of the mixer (see Ch. 6) which is a constant contribution for all measurements. This contribution is not relevant if only the difference in  $T_{rec}$  is studied, as it is done below. Both  $T_{mixer}$  (see Eq. 19) and  $1/G_{mixer}$  (see Eq. 11) are proportional to  $1/P_{LO}$ . Since  $T_{IF}$  is almost constant for temperature below 10 K,  $T_{rec}$  is proportional to  $1/P_{LO}$ .  $T_{rec}$  can be approximated with the Eq. 51 by [93]:

$$T_{rec} \propto \frac{1}{1 - (T_{bath}/T_c)^n}, \quad (52)$$

where the exponent  $n$  is the only fitting parameter. For NbN films where the phonon cooling is dominating the parameter  $n$  is about 3.6 [93]. The parameter  $n$  does not need to be identical for each wafer, because it is used as a free material parameter. The fit of the data delivers an exponent of  $n(14-11) = 3.4$  and  $n(14-08) = 3.6$  (See Fig 97). The result corresponds well to the literature value for phonon cooled films, which is 3.6 [40]. However, the value of parameter  $n$  is very critical because it appears in the exponent of Eq. 8. Therefore a more accurate determination of  $n$  would be beneficial to the analysis. A possibility would be to extend the measurement of Fig. 97 over a larger temperature range,

especially close to  $T_c$ . In the following analysis I use  $n = 3.6$  for both wafers.

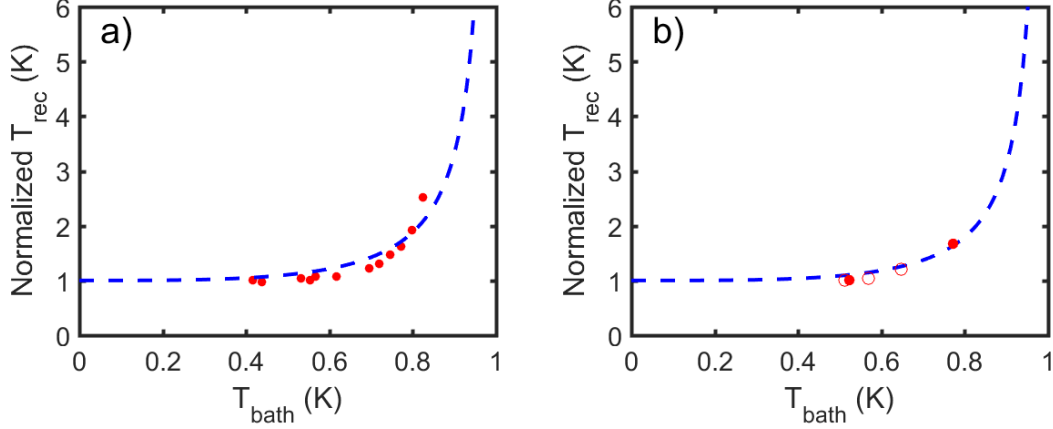


**Figure 97:** Normalized  $T_{rec}$  as a function of  $T_{bath}$ : a) wafer 14-11 (device N19) and b) wafer 14-08 (devices R02 and J13).

If the value of 3.6 is used in Eq. 50, the average tabulated data for  $T_c$  and  $\Delta T_c$  (Tab. 15) lead to a ratio of the required LO power of about 8.8 between wafer 14-08, and 14-11. This factor of 8.8 should be compared to the experimental factor of 5, as shown in Tab. 14. The power ratio is calculated under the assumption that  $V$  and  $\gamma$  and  $\tau_\Theta$  are identical for both wafers. To check this assumption first,  $\gamma$  is further investigated. The Sommerfeld constant  $\gamma$  for the measured films can be determined by [94],

$$\gamma = \frac{1}{3} \pi^2 k_B^2 DOS(E_F), \quad (53)$$

where  $k_B$  the Boltzmann constant and  $DOS(E_F)$  determined the total electronic density of states at the Fermi level [95]. The total electronic density of states,

$$DOS(E_F) = \frac{1}{e^2 \cdot \rho_N \cdot D}, \quad (54)$$

depends on the elementary charge  $e$ , the normal state resistivity  $\rho_N$  and on the diffusion constant of the quasiparticles  $D$  (in  $\text{nm}^2/\text{ps}$ ). The normal state resistivity is determined from the product of the resistance  $R_N$  above the  $T_c$  times the area of the HEB film (width of 3050 nm and thickness of 3.5 nm) divided by the length of 200 nm. The diffusion constant was not measured and had to be taken from the literature. S. Krause determined the diffusion constant by  $D = 40 \text{ cm}^2/\text{s}$  for 5.3 nm thick NbN film ( $10 \mu\text{m} \times 70 \mu\text{m}$ ) [96]. The diffusion constant is strongly dependent on the film thickness which leads for a thinner film to a lower value of the diffusion constant. For a more accurate calculation  $D$  has to be determined

separately for both measured wafers. By using the literature value of  $D$  the Sommerfeld constant ( $\gamma$ ) for our films is determined (see Tab. 16). The literature value of  $\gamma$  is about 3 times larger as the calculated value for our thinner films.

wafer	$R_N$ (Ohm)	$d$ (nm)	$\gamma$ ( $J/K^2/m^3$ )
14-11	157	3.5	73
14-08	134	3.5	86
[94]	420	6	220

**Table 16:** Sommerfeld constant determined for wafer 14-11, 14-08 and for a film by Bartolf et al. [94].

To get a theoretical expression for  $P_{LO}$  as a function of  $I_c$ , the dependence of  $T_c$  in in Eq. 50 has to be replaced by one on  $I_c$ .  $I_c$  as a function of the ratio of the bath temperature ( $T_{bath}$ ) to  $T_c$ , can be estimated from the Ginzberg Landau theory by [97]:

$$I_c = I_c(0) \left[ 1 - \left[ \frac{T}{T_c} \right]^2 \right] \cdot \left[ 1 - \left[ \frac{T}{T_c} \right]^4 \right]^{1/2} \quad (55)$$

where  $I_c(0)$  is the critical current at 0 K. The measured data of  $I_c$  as function of  $T_c$  from Tab. 6 are shown in Fig. 98. The  $I_c$  in dependency of the measured  $T_c$  calculated from Eq. 55 is also plotted. The value of  $I_c(0)$  is set arbitrarily to  $250 \mu A$  to describe the averaged  $I_c$ . Here it is obvious that the calculated values of  $I_c$  are not a good description of the measured values.

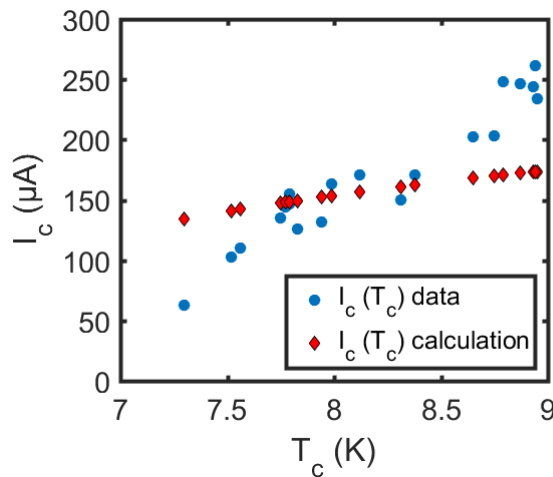


**Figure 98:**  $I_c$  as function  $T_c$  for the measured data inside the liquid helium dewar at bath temperature of 4.5 K. The measured data are plotted in circles and calculated results by Eq. 55 plotted in diamond.

Subsequently, I investigated if the arbitrary chosen  $I_c(0)$  depends on the wafer and if a better estimate for  $I_c(0)$  would be possible on the wafer. The value of  $I_c(0)$  is determined for each wafer by using a calibration measurement of  $I_c$  between 0 K and  $T_c$  (see Fig. 99). The  $I_c$  is measured for several devices (two for wafer 14-11, three for wafer 14-08) as a function of bath temperature. The fit by Eq. 55 of the data reveals that the  $I_c(0)$  is not constant for all devices on one wafer. Based on the data in Fig. 99, I assume that  $I_c(0)$  depends to first order linearly on  $T_c$ .

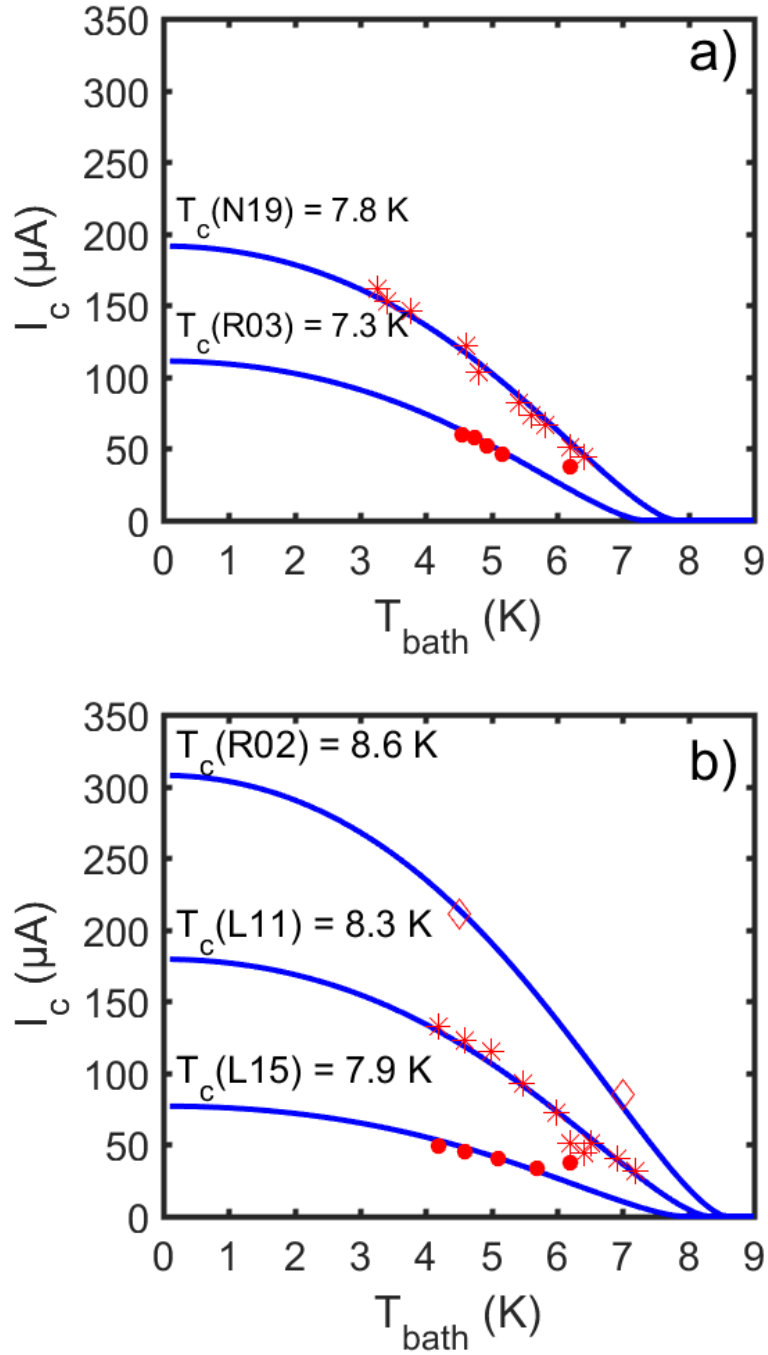
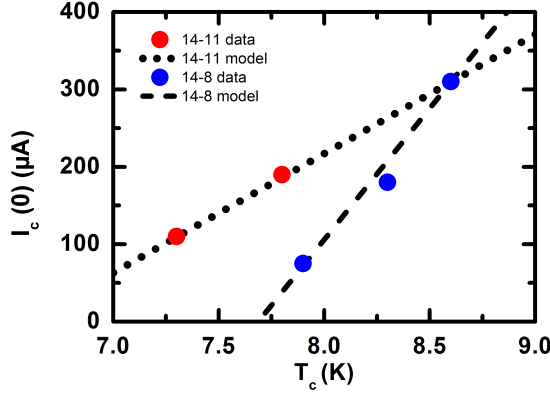


**Figure 99:**  $I_c$  as a function of bath temperature: a) wafer 14-11 (devices R03 / N19) and b) wafer 14-08 (devices R02 / L15 / L11).

The  $I_c(0)$  as a linear function of  $T_c$  for both wafers is listed in Tab. 7.1.3 where  $\alpha$  is the slope and  $\beta$  is the intercept with  $I_c(0)$  at  $T_c = 0$  K (fit to the data is shown in Fig. 100).



wafer	$\alpha$ ( $\mu\text{A}/\text{K}$ )	$\beta$ ( $\mu\text{A}$ )
14-08	339	-2606
14-11	154	-1015

**Figure 100:** Linear dependency of  $I_c$  was a function of  $T_c$ .

**Table 17:** Temperature and gas flow during growing process.

By solving, then the Eq. 55 self-consistently, replacing  $I_c(0)$  by the linear interpolation, for each device it is possible to calculate  $T_c$  as a function of  $I_c$ . I am using the result as a basis for Eq. 50 to determine the required  $P_{LO}$  as a function of  $I_c$ .

The electron temperature relaxation time  $\tau_\Theta$  remains as the last free parameter for the model of  $P_{LO}$ , and is estimated from the fitted gain bandwidth as shown in section 6.1.10. The results of the measured gain shown in Fig. 70 are about  $(1.6 +0.2/-0.1)$  GHz, which correlates to a  $\tau_\Theta$  of  $(99.5 +6.6 /- 11.1)$  ps. An optimum LO power of about 10 nW is calculated for devices from wafer 14-11 and 14-08. This value is not in correspondence with the measured values of 300 - 1500 nW (see Tab. 14).

This result shows that the theoretical model based on the lumped element heat balanced equation in this case cannot be used to reproduce the measured incident required LO power. The determination of  $\gamma$  based on the diffusion constant taken from the literature for a significant thicker film is probably not accurate enough. A measurement setup with a magnetic field of significantly stronger than 1 T [96] would be necessary to measure the diffusion constant which was not available.

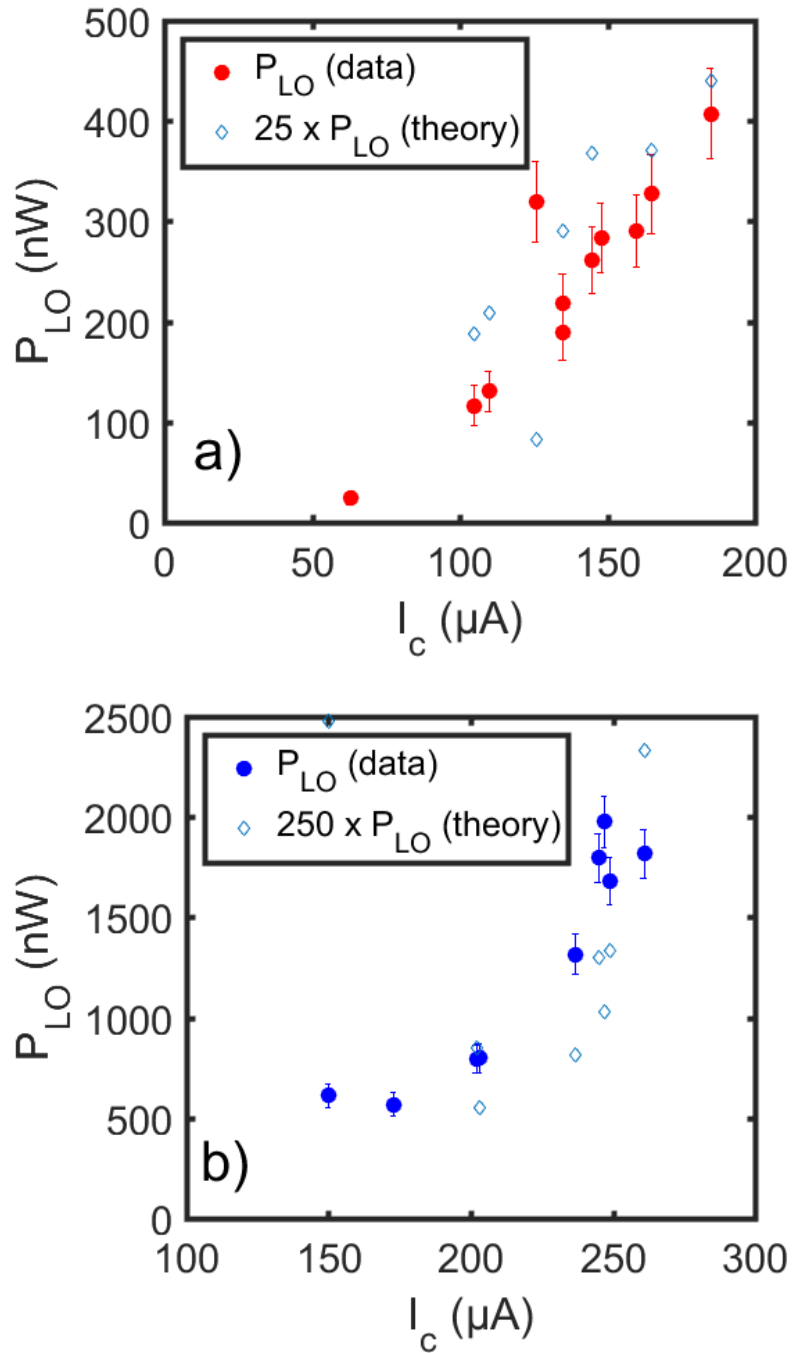


**Figure 101:** Required LO power for optimum operation as a function of critical current. The measured incident LO power ( $P_{LO}(data)$ ) is compared with the theoretical required LO power ( $P_{LO}(theory)$ ).  $P_{LO}(theory)$  is scaled for both wafers. The top figure shows wafer 14-11 in red and the bottom figure wafer 14-08 in blue.

### 7.1.4 Mixer Sensitivity

The sensitivity of the mixers is determined using the Callen-Welton expression (see Eq. 31) to determine the input power from the calibration load (see Sec. 6.1.4). For a comparison of the mixers, the unavoidable quantum noise which is about 45 K for the Double Side Band (DSB) mixers at 1.9 THz, is separated from the mixer noise for the analysis of the mixer.

The influence of the direct direction effect explained in Sec. 5.4.2 was estimated with a comparison of the averaged receiver noise temperature ( $T_{rec,c}$ ) measured with a spectrometer compared to that with the LOPS measurement. The averaged noise temperature at an IF of 1.5 GHz measured with the spectrometer was 900 K which is about 30 % higher as the result of the LOPS measurement of 700 K.

Theoretically, the mixer noise temperature and gain (see Sec. 2) have a dependence on the critical temperature ( $T_c$ ) [40]. The theoretical dependence of the mixer gain on  $T_c$  (Fig. 15) and the fluctuation noise (see Eq. 20) which is the largest contribution to the mixer noise, depends linearly on  $T_c$ . The measured results of the gain and noise temperature in dependence on  $T_c$  and  $I_c$  are shown in Fig. 102. The inaccuracies shown in the plot are calculated by systematic errors of the measurements (see Sec. 6.1.4). The gain and the noise temperature do not show a significant dependency of  $T_c$  and  $I_c$ . The larger systematic errors, allowing no further conclusions of the dependence of mixer properties on the  $T_c$  and  $I_c$ . Both wafers (14-08 / 14-11) can only slightly be distinguished by the difference of average mixer.

The measured normal state resistance ( $R_n$ ) listed in Tab. 6 for both wafers shows a significant difference to the simulated value of 120 Ohm. The dependency of the gain of the measured  $R_n$  is shown in the left plot of Fig. 103. The gain shows a dependency on the  $R_n$  indicating that the impedance mismatch has an influence on the mixer performance.

For a fair comparison, I have separated the influence of the mismatch from mixer gain. This is done by introducing the measured value of  $R_n$  into the simulation. The difference in calculated power coupling using the real value of  $R_n$  compared to that using the design value I call the gain difference. The gain difference is in the order of  $(0.18 \pm 0.13)$  dB for all devices, which should thus be added to the de-embedded mixer gain. The gain as a function of  $R_n$  corrected for the impedance mismatched is shown in the right plot in Fig. 103. This result shows that the impedance mismatch of a HEB has not a significant influence on the de-embedded mixer noise performance and will be neglected.

Furthermore, a comparison of the measured results with the theoretical broken lines transmission model was done, with the following approximation and assumptions: the bath temperature ( $T_{bath}$ ) is well below the  $T_c$  ( $T_c^n \gg T_{bath}^n$ ),  $n \sim 3.6$  (see Fig. 97), the supercon-

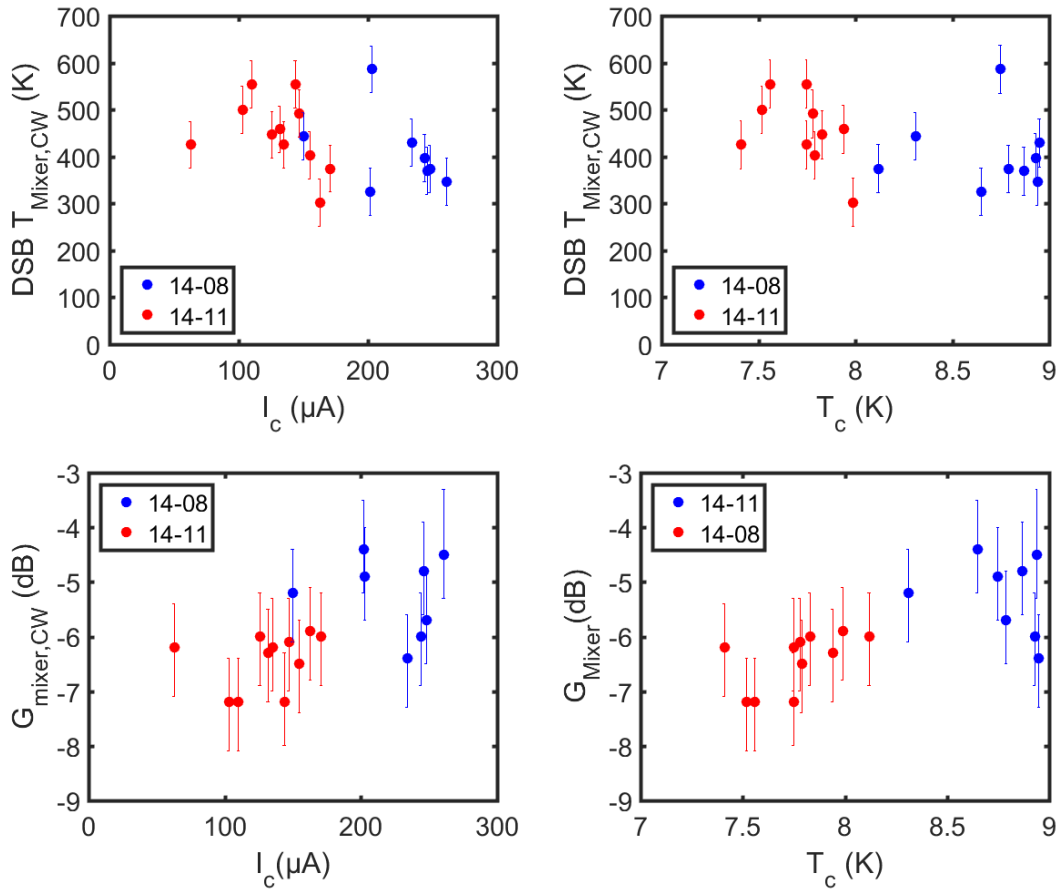


**Figure 102:** Top: Mixer noise temperature in dependency of the  $I_c$  (left) and  $T_c$  (right). Bottom: Mixer gain in dependency of the  $I_c$  (left) and  $T_c$  (right).

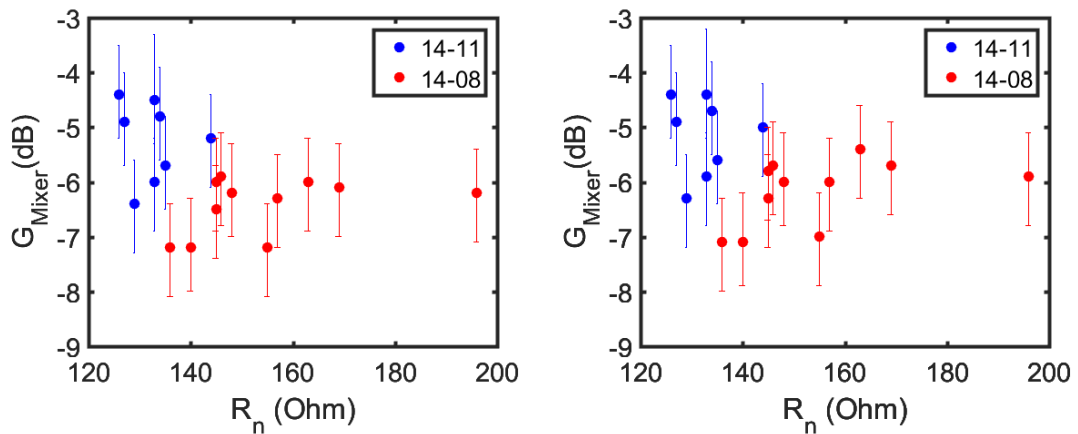


**Figure 103:** Left plot: Mixer noise temperature as a function of the  $R_n$ . Right plot: Mixer noise temperature as a function of  $R_n$  corrected for the impedance mismatch.

ducting transition width  $\Delta T_c$  is small in comparison to  $T_c$ ,  $R_0 = R_n/2$  and the self heating parameter  $C \sim 1$ . A comparison of the theoretically calculated and measured gain at an IF of 1.5 GHz is shown in Fig. 104. In addition, the theoretically calculated and measured mixer noise temperature is shown.

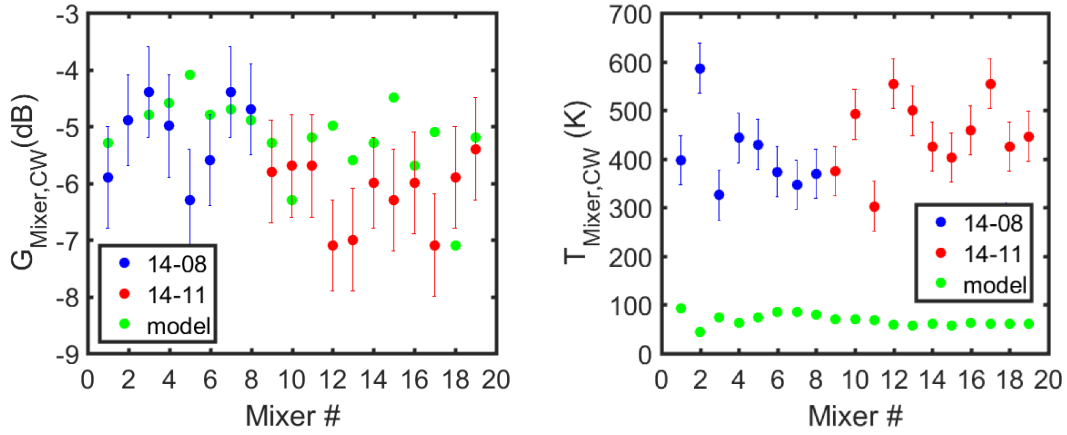


**Figure 104:** Left: Measured gain in comparison with theoretical calculated broken line transition model as a function of the mixer # in order measurement. Right: Measured gain in comparison with theoretical calculated broken line transition model as a function of the mixer # in order measurement.

Obviously, the measured gain is in a good agreement with the theoretically calculated gain based on the broken line transmission model. The gain difference to the averaged measured ( $-5.9 \pm 0.2$ ) dB is less than 2 dB. The measured gain results fit to the measurements from Miao et al. where a similar mixer gain of -6 dB is measured [83] for comparable devices.

The noise temperature is deviating significantly from the theoretical model. The model noise temperatures are a factor 4 - 8 lower as the measured results. Miao et al. measured a mixer noise temperature of about 200 K which is also a factor 3 - 4 lower than the theoretical value.

Both results indicating that the gain of the mixer is well understood. The mixer noise temperature of the HEB mixer is not completely understood. An additional noise mechanism which is not included in the model could be the reason for this discrepancy.

### 7.1.5 IF Noise and Gain Bandwidth

The IF noise bandwidth of the mixers for both wafers 14-11 and 14-08, presented in Sec. 6.1.9, is compared with the predicted noise bandwidth determined from Eq. 14 (see also Fig. 15 and 105). The model based on Eq. 16 (at  $T_c$  of 8 K) predicts a bandwidth of about 13 GHz based on the empirical Eq. 17 [34] [36] [42]. This bandwidth is a factor of about 3 to 4 larger than the measured result of 4 GHz. In the literature Miao et al. show a difference in the noise bandwidth by a factor 2 in comparison the measured values [83]. The noise bandwidth of the 4.7 THz mixer from the wafer 13-05 is about 3.5 GHz [98] which is about 0.5 GHz lower than the typical bandwidth of mixers from the wafers 14-11 and 14-08. This result is in agreement with a longer phonon escape time due to the thicker film of 4.5 nm instead of 3.5 nm which leads to change of bandwidth of about 0.6 GHz (see Sec. 2.3.5, Eq. 14).

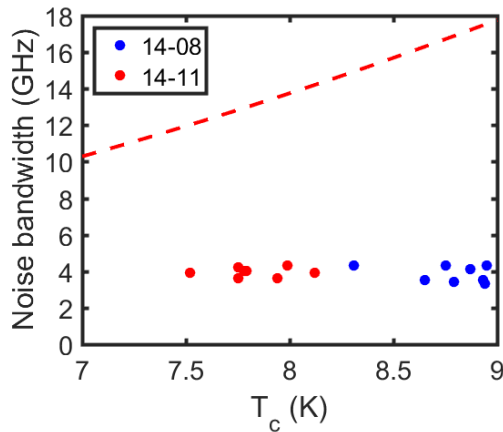


**Figure 105:** Noise bandwidth of a set of 19 mixers. 11 mixers of wafer 14-11 in red and 8 from wafer 14-08 in blue as function of  $T_c$  in comparison to a theoretical model of the broken line transition model.

A comparison of the gain and noise bandwidth from Sec. 6.1.10 and 6.1.9 is presented in Fig. 106. Both wafers, 14-08 and 14-11, show the same averaged noise bandwidth (NBW) of 4 GHz and averaged gain bandwidth (GBW) of 1.6 GHz determined by a single pole roll-off fit to the data.

Here I do not observe any dependence of the critical temperature ( $T_c$ ) although this is also predicted by the lumped element model [40]. The ratio of about 2.5 between the noise and the gain bandwidth is calculated from Eq. 3 and Eq. 16.

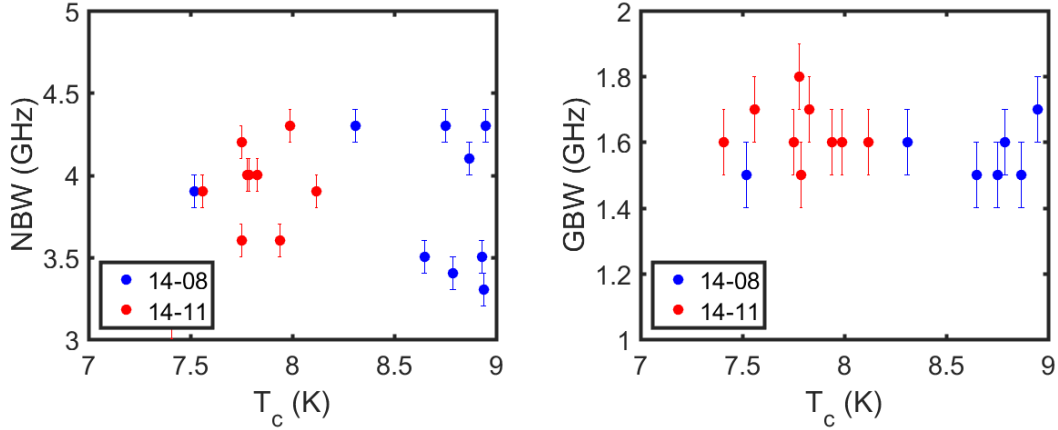


**Figure 106:** Receiver noise bandwidth and the mixer gain bandwidth for the set of 20 mixers. 11 mixers of wafer 14-11 in red and 9 from wafer 14-08 in blue as function of  $T_c$ .

### 7.1.6 Silicon Inlay Technology

The concept of the Si inlay technology is presented in Sec. 6.2. The waveguide with dimensions of  $96 \mu\text{m} \times 46 \mu\text{m}$  was etched into Silicon (Si) and then gold plated with a  $1 \mu\text{m}$  layer [54]. These inlays were assembled into a copper block containing the IF connector and a slot for the Si piece with the waveguide cavity, the substrate channel and the IF contact board, all in one piece of Silicon. Afterward, the heterodyne performance of the block is measured as usual in a vacuum liquid-cooled helium dewar, using the same set-up as for all other mixers. The FTS response is in a good agreement with the metal waveguide block. The measured noise temperature in comparison with the metal waveguide blocks is about 20 % higher. A possible reason for the reduced sensitivity could be increased losses inside the waveguide because of a bad coverage of the waveguide walls with sputtered gold, which was visible in SEM photos. Due to the urgent measurement for the LFA array, no further investigations towards this concept were done.

## 7.2 Comparison of NbN and NbTiN Based HEB Mixers

A comparison of HEB mixers based on a NbN bridge on a  $2 \mu\text{m}$  Si membrane with NbTiN HEBs on a  $2 \mu\text{m}$  SiN membrane is discussed in this section [99]. The measurements of all mixers compared here were done using the same heterodyne setup presented in Sec. 4.1.

The volume of the film was reduced by approximately a factor of 2, by reducing the lateral dimensions and the thickness of the film. The result from this reduction and a comparison of the main properties of the NbTiN mixer and the different wafers of NbN mixers

	NbTiN	NbN (LFA) wafer: 13-05	NbN (LFA) wafer: 14-08 / 14-11
HEB dimensions (nm <sup>3</sup> )	4 x 400 x 3100	4.5 x 300 x 3600	3.5 x 200 x 3050
NBW (GHz)	2.1	3.5	3.9 ± 0.2
gain <sub>mixer</sub> (dB)	-10 ± 1	-	-6 ± 1
T <sub>mixer</sub> (K)	500 ± 50	-	410 / 450
incident LO power (μW)	0.5	4	1.5 / 0.3

**Table 18:** Comparison of the NbTiN and NbN HEB mixer performance for different wafers.

are listed in Tab. 18. For the device N15 from wafer, the 13-05 no de-embedded noise temperature and gain were available since those devices were rejected for the array, because of their high LO power consumption. The focus of the measurements were the 14-08 and 14-11 wafer mixers.

One of the main differences between NbTiN HEBs and NbN HEBs is the receiver IF noise bandwidth. The bandwidth for NbTiN mixers is about 2.1 GHz in comparison to NbN mixers with a bandwidth of 4 GHz for wafer 14-08 and wafer 14-11 (see Fig. 107). The bandwidth of the mixer from the wafer 13-05 was about 3.5 GHz. The reason for this reduced bandwidth is given by the difference in the film thickness of 4.5 nm in comparison to 3.5 nm. The bandwidth scales inversely proportional to the phonon escape time, which depends linearly on the thickness of the film [36].

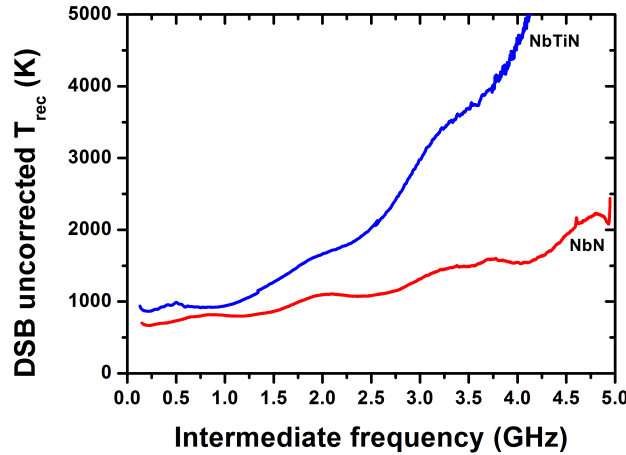


**Figure 107:** Comparison of the receiver noise temperature as a function of IF for two mixers based on a NbTiN and NbN film (14-11).

In addition the incident LO power which is required for the optimum operation varies significantly for both materials and wafers as mentioned before. For an array the incident LO power requirement is crucial due to the limited output power of the available LO sources. A

comparison of the incident LO power for the devices from the three measured NbN wafers and the NbTiN device is shown in Fig. 108. For a similar volume of the HEB, the NbN HEB needs about a factor of 10 more LO power as the NbTiN mixers. The mixers from wafer 14-08 and 14-11 required in average  $1.5 \mu\text{W}$  and  $0.3 \mu\text{W}$  for a similar NbN volume. At first the mixers from the wafer 14-08 were integrated into the instrument and measurement showed that the second LO source had not enough output power to operate those devices. So new mixers from the wafer 14-11 were required to be able to compensate the low output power of the LO source.

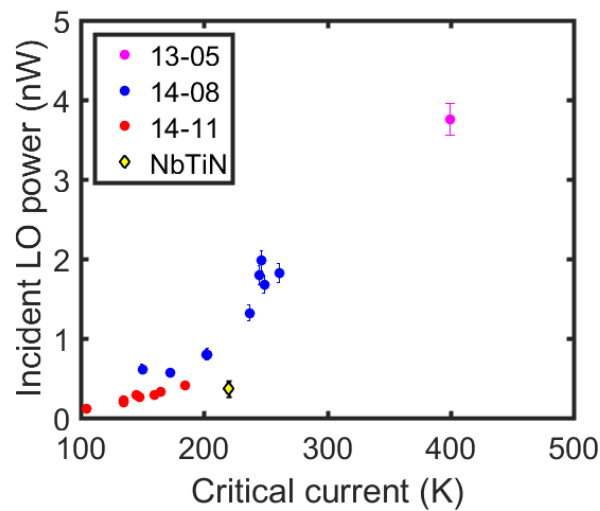


**Figure 108:** Comparison of the incident LO power as a function of critical current for mixers based on a NbTiN and NbN films (13-05/14-08/14-11).

Both mixers types have a similar sensitivity of about 400 K, averaged of a 1 - 2 GHz IF bandwidth. The measured mixer gain for the NbTiN mixers is about - 10 dB which is - 4 dB lower as the average NbN mixer gain. Both, mixer noise temperature and the gain are de-embedded from the receiver contributions. The theoretically predicted gain with the broken-line transition model from Eq. 18 can be adapted to the measured value by taking a value of about  $0.85 \pm 0.20$  for C for the NbN HEBs. The measured NbTiN gain of - 10 dB in comparison to the theoretical gain is - 3 dB lower. The theoretical gain cannot be corrected with a different C for a higher gain. The discrepancy of the theoretical gain to the measured gain is unclear and further measurements have to be done to verify this result of a single mixer. The theoretical mixer noise temperature calculated by Eq. 20 is 50 K for both types of mixers which is far below the measured noise temperature of 410 - 450 K.

The difference of the required incident LO power, for devices from the wafer 14-11 and 14-08 with a similar volume, shows that the film thickness is at the limit of the film thickness.

The required incident LO power varied more than a magnitude for the device with almost the same thickness. Furthermore, the devices showing the effects of aging which are particular issue for the device with the small LO power requirement.

## 8 Summary and Outlook

I started with the development of a waveguide HEB mixer for operation at 4.7 THz for the H channel of the GREAT receiver [18] [22]. The 4.7 THz mixer was the first waveguide mixer at this high operation frequency [22]. The mixer shows excellent performance at the H-channel receiver with a noise temperature of 900 K at an IF between 1 - 2 GHz. In this mixer we used for the first time a NbN HEB layer on a Si substrate, contrary to earlier developments where a NbTiN HEB layer was used on a SiN substrate [100]. Compared to the latter, the NbN HEB on Si shows a 2 times higher instantaneous IF bandwidth of almost 4 GHz. The LO power consumption of a NbN HEB turned out to be almost a factor of 10 higher than for NbTiN HEBs, for a devices of roughly the same dimensions and sensitivity. The waveguide blocks are made of a CuTe alloy and are fabricated in house [22].

The NbN layer was optimized for highest  $T_c$ , at a reasonable and reproducible thickness of approximately 5 nm. The Si substrate is around 2  $\mu\text{m}$  thick, fabricated using SOI technique, and contacted by beamleads [21]. After the successful development of the 4.7 THz waveguide mixer 14 waveguide mixers were fabricated, measured and integrated for the upGREAT Low Frequency Array (LFA) receiver operating at 1.9 THz, using the same device technique [19] [23] [24]. The HEB devices for these mixer all originate from the same wafer, of which the NbN layer was optimized for lower LO power consumption. The LO power consumption could be reduced in average by a factor of 4 compared to a similar mixer, at the same operating frequency, using a device from the wafer used for the 4.7 THz wafer [23]. Due to a lower than expected output power of one of the two LOs in the upGREAT receiver a replacement of an additional 7 mixers was also developed. The devices for these mixers came from another wafer, where the NbN layer was even further optimized for low LO power consumption, resulting in another average factor of 2 - 3 reduction in power consumption.

For a later wafer unfortunately the spread in HEB properties was higher and also the device layer was much more sensitive to handling steps during fabrication, assembly and test than the previous wafers. This resulted in a low yield in mixers similar enough to be part of an array. Presently this prohibits the development of focal plane array receivers with many more pixels, where one would actually want to reduce the LO power consumption per mixer even more, to be able to pump more pixels with the same LO source. From mixer development point of view, a stable process for the development of mixers with the lowest LO power consumption, involving passivation layers for NbN bridge and probably also a somewhat different mechanical design would be the next step towards array receivers with many more pixels. Another approach, to also reduce the LO power per pixel would be the

development of balanced mixers [84] [101] [102]. In these mixers there are separated ports for the LO and the signal in the mixers, so the beamsplitter (which couples only about 10% of the LO power) no longer necessary.

Both the H-channel and the LFA array were successfully commissioned for GREAT/upGREAT on SOFIA and are regularly used for observations since 2014 and 2015. The integrated mixers have state of the art performances. The mixer calibration results in the GREAT receiver are consistent with the lab measurements showing that my setup is adequate to characterize the mixer. In addition, the stability of the mixers that we could not measure in the laboratory, has shown to be sufficient for astronomic line observations, even for the mixers with the smallest HEB bridges and the lowest LO power consumption. The performance of the LFA mixers and that of the 4.7 THz mixer are surprisingly similar. Apparently our HEB devices have no significant frequency dependence from 1.9 to 4.7 THz [18] [19] [22] [23] [24].

In total I measured the performance of 34 mixers at 1.9 THz, 20 mixer devices from the wafer with a medium LO power consumption and 14 of the wafer with the very low LO power consumption. The measurements of the many mixers with devices of those two wafers gave me a large dataset for empirical investigations. The noise and gain of the mixer itself was de-embedded from the calibration measurements. The DSB mixer noise temperature averaged over all delivered mixers over an IF of 1 - 2 GHz is about  $(430 \pm 20)$  K with a noise bandwidth of  $(3.9 \pm 0.2)$  GHz. The mixer gain is about  $(-5.9 \pm 0.2)$  dB. This mixer performance is fairly similar for devices from the same wafer and even between wafers there is not a very large difference. When mixer gain and noise are regarded separately a small difference of about 1 dB in gain can be observed between the two wafers, whereas the noise is really indistinguishable.

The measured performance results of the LFA mixers are compared to the broken-line-transition model which theoretically predicts the mixer gain and noise temperature, based on the measured resistance versus temperature curve of the bridge. The correspondence between the measured results and the theoretical ones is not very good. The de-embedded mixer gain corrected for the antenna impedance mismatch is 1 - 3 dB lower than the theoretical predicted gain. The measured mixer noise is in average unfortunately a factor of 6 higher than the theoretical prediction. The accuracy of the measured results is not high enough to investigate a dependency of the mixer properties on the  $T_c$  and  $I_c$  of the HEB bridge. The accuracy of the measured results is not sufficient but much more accurate measurements would be necessary to relate this to the wafer properties. Finally also the theoretically predicted LO power consumption is more than an order of magnitude lower than the measured one. This confirms that at present no adequate model for the HEB mixer

properties is available [11]. For future array receiver development however, it would be very advantageous if the final mixer performance could be predicted as early as possible, especially for a uniform HEB LO power requirement and mixer sensitivity. Currently, a number of mixers have to be measured to conclude on an empirical level, whether it is within the specifications required for uniform array operation.

Although it is not the main focus of this thesis, it is interesting to note that the fabrication of the waveguide blocks and the assembly accuracy of the devices are in general very repeatable. The RF response bandwidth of the HEB mixers measured with the FTS shows a reproducible response for all mixers. The comparison of this measured broadband response with simulated response in CST shows a fair agreement of the response at the lower part of the frequency of the LFA mixers [56]. Around 4.7 THz, the FTS response for two different designs HFA-1b and HFA-3, is very well in agreement with the simulation of the RF circuits. The promising approach of a Si inlay technology, which would reduce the tolerances in the waveguide dimensions as well as in the assembly of the devices, was tested in a heterodyne measurement for one mixer. The FTS response is indistinguishable from that of the metal waveguide blocks, but the measured receiver noise temperature is unfortunately about 20 % higher [84]. We conclude that this mixer performance is so far not comparable to metal blocks. Additional measurements and development have to be done for which the development for the upGREAT array unfortunately left us no time. Another unknown of the Si inlay technology is the reliability of the performance after a series of thermal cycling which is important for long-term observations.

For a further increase of mixer IF noise bandwidth of NbN based HEB mixers, an improved acoustic matching between the HEB micro-bridge and the substrate, leading to a shorter phonon escape time, might be achieved by using another material combination. S. Krause et al. have used GaN as a buffer-layers to improve the escape time [103] [104]. Recently Novoselov et al. [53] published the results of heterodyne measurement of a HEB based on MgB<sub>2</sub> film on SiC substrate ( $T_c$  of 30 K). The presented noise bandwidth was about 11 GHz at a noise temperature of 1100 K measured at 1.6 THz [53]. However for optimal operation, this HEB needed at minimum 13  $\mu$ W power. For an array operation at the LFA receiver, this LO power requirement has to be reduced at least by a factor of 10. At present the development of this material combination cannot be fabricated in our micro fabrication laboratory.

Optimization on the HEB mixer IF side is also of interest. Instead of the simple IF board with a 50 Ohm impedance transmission line, a matching circuit could reduce the mismatch between HEB device and LNA [105], avoiding the standing wave between the mixer and the LNA. In order to design this matching network it is required to know the HEB mixer

output impedance for a particular mixer design. Development of a microwave reflection measurement setup would be required for this task [106].

## Bibliography

- [1] M. Röllig, R. Simon, R. Güsten, J. Stutzki, F. P. Israel, and K. Jacobs. **[CII] 158  $\mu\text{m}$  and [NII] 205  $\mu\text{m}$  emission from IC 342: Disentangling the emission from ionized and photo-dissociated regions.** *Astronomy & Astrophysics*, 591, A33, 2016.
- [2] S. Leurini, F. Wyrowski, H. Wiesemeyer, A. Gusdorf, R. Güsten, K. M. Menten, M. Gerin, F. Levrier, H. W. Hübers, K. Jacobs, O. Ricken, and H. Richter. **Spectroscopically resolved far-IR observations of the massive star-forming region G5.89–0.39.** *Astronomy & Astrophysics*, 584, A70, 2015.
- [3] S. Malhotra, M. J. Kaufman, D. Hollenbach, G. Helou, R. H. Rubin, J. Braucher, D. Dale, N. Y. Lu, S. Lord, and G. Stacey. **Far-Infrared Spectroscopy of Normal Galaxies: Physical Conditions in the Interstellar Medium.** *The Astrophysical Journal*, 561, 2, 2001.
- [4] De Looze, Ilse Cormier, Diane Lebouteiller, Vianney Madden, Suzanne Baes, Maarten Bendo, George J. Boquien, Médéric Boselli, Alessandro Clements, David L. Cortese, Luca Cooray, Asantha Galametz, Maud Galliano, Frédéric Graciá-Carpio, Javier Isaak, Kate Karczewski, Oskar Ł. Parkin, Tara J. Pellegrini, Eric W. Rémy-Ruyer, Aurélie Spinoglio, Luigi Smith, Matthew W. L. Sturm, and Eckhard. **The applicability of far-infrared fine-structure lines as star formation rate tracers over wide ranges of metallicities and galaxy types.** *Astronomy & Astrophysics*, 568, A62, 2014.
- [5] Ronan Higgins. **Privat comunication and simulated data set for amospheric transmission.**
- [6] C.M. Gillespie. **Kuiper Airborne Observatory /Space Science Platform.** *Proceedings of SPIE - The International Society for Optical Engineering*, 1981.
- [7] G. L. Pilbratt. **Herschel Space Observatory.** *Astronomy & Astrophysics*, 518, L1:1–6, Jul. 2010.
- [8] ESA. [http://www.esa.int/Our\\_Activities/Space\\_Science/ISO\\_overview/](http://www.esa.int/Our_Activities/Space_Science/ISO_overview/).
- [9] C. Walker, C. Kulesa, P. Bernasconi, H. Eaton, N. Rolander, C. Groppi, J. Kloosterman, T. Cottam, D. Lesser, C. Martin, A. Stark, D. Neufeld, C. Lisse, D. Hollenbach, J. Kawamura, P. Goldsmith, W. Langer, H. Yorke, J. Sterne, A. Skalare, I. Mehdi, S. Weinreb, J. Kooi, J. Stutzski, U. Graf, M. Brasse, C. Honingh, R. Simon,

- M. Akyilmaz, P. Puetz, and Mark Wolfire. **The Stratospheric TeraHertz Observatory (STO)**. *Proceedings of the 20th International Symposium on Space Terahertz Technology*, page 107, 2009.
- [10] K. Zhou, W. Miao, Z. Lou, J. Hu, S. Li, W. Zhang, S. Shi, R. Lefevre, Y. Delorme, and T. Vacelet. **1.4 THz Quasi-Optical NbN Superconducting HEB Mixer Developed for the DATE5 Telescopes**. *IEEE Transactions on Applied Superconductivity*, 25(3):1–5, 2015.
- [11] Teun Klapwijk. **Engineering the physics of superconducting hot-electron bolometer mixers**. *Invited talk, 28th International Symposium on Space Terahertz Technology, Cologne, Germany, 2017*.
- [12] D.E. Prober. **Superconducting terahertz mixer using a transition-edge microbolometer**. *Applied Physics Letters*, 62, 1993.
- [13] K. Shimoda, H. Takashi, and C.H. Townes. **Fluctuations in Amplification of Quanta with Application to Maser Amplifiers**. *J. Phys. Soc. Japan*, 12, 1957.
- [14] Carlton M. Caves. **Quantum limits on noise in linear amplifiers**. *Phys. Rev. D*, 26, 1982.
- [15] H. A. Haus and J. A. Mullen. **Quantum Noise in Linear Amplifiers**. *Phys. Rev. C*, 128, 1962.
- [16] H. Wiesemeyer, R. Güsten, S. Heyminck, H.W. Hübers, K.M. Menten, D.A. Neufeld, H. Richter, R. Simon, J. Stutzk, B. Winkel, and F. Wyrowski. **Far-infrared study of tracers of oxygen chemistry in diffuse clouds**. *Astronomy & Astrophysics*, 585, 2016.
- [17] A. Poglitsch, C. Waelkens, N. Geis, H. Feuchtgruber, B. Vandenbussche, L. Rodriguez, O. Krause, E. Renotte, C. van Hoof, P. Saraceno, J. Cepa, F. Kerschbaum, P. Agnèsè, B. Ali, B. Altieri, P. Andreani, J.-L. Augeres, Z. Balog, L. Barl, O. H. Bauer, N. Belbachir, M. Benedettini, N. Billot, O. Boulade, H. Bischof, J. Blommaert, E. Callut, C. Cara, R. Cerulli, D. Cesarsky, A. Contursi, Y. Creten, W. De Meester, V. Doublier, E. Doumayrou, L. Duband, K. Exter, R. Genzel, J.-M. Gillis, U. Grözinger, T. Henning, J. Herreros, R. Huygen, M. Inguscio, G. Jakob, C. Jamar, C. Jean, J. de Jong, R. Katterloher, C. Kiss, U. Klaas, D. Lemke, D. Lutz, S. Madden, B. Marquet, J. Martignac, A. Mazy, P. Merken, F. Montfort, L. Morbidelli, T. Müller, M. Nielbock, K. Okumura, R. Orfei, R. Ottensamer, S. Pezzuto,

- P. Popesso, J. Putzeys, S. Regibo, V. Reveret, P. Royer, M. Sauvage, J. Schreiber, J. Stegmaier, D. Schmitt, J. Schubert, E. Sturm, M. Thiel, G. Tofani<sup>0</sup>, R. Vavrek, M. Wetzstein, E. Wieprecht, and E. Wiezorrek. **The Photodetector Array Camera and Spectrometer (PACS) on the Herschel Space Observatory.** *Astronomy & Astrophysics*, 518, L2-2, 2010.
- [18] S. Heyminck, U.U. Graf, R. Güsten, J. Stutzki, H.W. Hübers, and P. Hartogh. **GREAT: the SOFIA high-frequency heterodyne instrument.** *Astronomy & Astrophysics*, 542, L1, 2012.
- [19] Christophe Risacher, Rolf Guesten, Juergen Stutzki, Heinz-Wilhelm Huebers, Denis Buechel, Urs U. Graf, Stefan Heyminck, Cornelia E. Honingh, Karl Jacobs, Bernd Klein, Thomas Klein, Christian Leinz, Patrick Puetz, Nicolas Reyes, Oliver Ricken, Hans-Joachim Wunsch, Paul Fusco, and Stefan Rosner. **First Supra-THz Heterodyne Array Receivers for Astronomy With the SOFIA Observatory.** *IEEE Trans. THz Sci. Technol.*, 6,2:199–211, March 2016.
- [20] Heiko Richter, Martin Wienold, Lutz Schrottke, Klaus Biermann, Holger T. Grahn, and Heinz-Wilhelm Hübers. **4.7-THz Local Oscillator for the GREAT Heterodyne Spectrometer on SOFIA.** *IEEE Transactions on Terahertz Science and Technology*, 5:539–545, 2015.
- [21] P. Puetz, C. E. Honingh, K. Jacobs, M. Justen, M. Schultz, and J. Stutzki. **Terahertz hot electron bolometer waveguide mixers for GREAT.** *Astronomy & Astrophysics*, 542, 2012.
- [22] Denis Büchel, Patrick Pütz, Karl Jacobs, Michael Schultz, Urs U. Graf, Christophe Risacher, Heiko Richter, Oliver Ricken, Heinz-Wilhelm Hübers, Rolf Güsten, Cornelia E. Honingh, and Jürgen Stutzki. **4.7 THz superconducting hot electron bolometer waveguide mixer.** *IEEE Trans. THz Sci. Technol.*, 5:207–214.
- [23] K. Jacobs M. Schultz P. Pütz, D. Büchel and C.E. Honinghk. **1.9 THz Waveguide HEB Mixers for the upGREAT Low Frequency Array.** *26th International Symposium on Space Terahertz Technology 2015, Cambridge, USA*, 2015.
- [24] C. Risacher, R. Güsten, J. Stutzki, H.-W. Hübers, A. Bell, C. Buchbender, D. Büchel, T. Csengeri, U. U. Graf, S. Heyminck, R. D. Higgins, C. E. Honingh, K. Jacobs, B. Klein and<sup>5</sup>, Y. Okada, A. Parikka, P. Pütz, N. Reyes and<sup>4</sup>, O. Ricken, D. Riquelme, R. Simon, and H. Wiesemeyer. **The upGREAT 1.9THz multi-pixel high resolution spectrometer for the SOFIA Observatory.** *Astronomy & Astrophysics*, May 2016.

- [25] P. L. Richards. **Bolometers for infrared and millimeter waves.** *Appl. Phys. Lett.*, 76, 1994.
- [26] F. Arams, C. Allen, B. Peyton, and E. Sard. **Millimeter mixing and detection in bulk InSb.** *Proceedings of the IEEE*, 54, 1966.
- [27] T. G. Phillips and K. B. Jefferts. **A Low Temperature Bolometer Heterodyne Receiver for Millimeter Wave Astronomy.** *Review of Scientific Instruments*, 44, 1973.
- [28] SEM photos courtesy by Patrick Pütz and Karl Jacobs.
- [29] E.M. Gershenzon, G.N. Gol'sman, I.G. Gogidze, Y.P. Gusev, A.I. Elant'ev, B.S. Karasik, and A.D. Semenov. **Millimeter and submillimeter range mixer based on electronic heating of superconductive films in the resistive state.** *Supercond., Phys. Chem. Technol.*, 10:1582–1597, 1990.
- [30] E.M. Gershenzon, M.E. Gershenzon, G.N. Gol'tsman, A.M. Lyul'kin, A.D. Semenov, and A.V. Sergeev. **Electron-phonon interaction in ultrathin Nb films.** *JETP*, 70:505, 1990.
- [31] R. A. Wyss, B. S. Karasik, W. R. McGrath, B. Bumble, and H. LeDuc. **Noise and bandwidth measurements of diffusion-cooled Nb hot-electron bolometer mixers at frequencies above the superconductive energy gap.** *10th ISSTT Proceedings*, pages 215–228, 1999.
- [32] A. Shurakov, Y. Lobanov, and G. Goltsman. **Superconducting hot-electron bolometer: from the discovery of hot-electron phenomena to practical applications.** *Supercond. Sci. Technol.*, 29.
- [33] Michael Tinkham. **Introduction to superconductivity.** *Dover Publications, USA*, second edition, 2004.
- [34] Yu. P. Gousev, G. N. Gol'tsman, A. D. Semenov, E. M. Gershenzon, FL S. Nebosis, M. A. Heusinger, and K. F. Renk. **Broadband ultrafast superconducting NbN detector for electromagnetic radiation.** *Journal of Applied Physics*, 75:3695, 1994.
- [35] Ren Da-Hua and Cheng Xin-Lu. **First-principles calculations on the elastic and thermodynamic properties of NbN.** *Chinese Physics B*, 21.
- [36] K. S. Il'in, M. Lindgren, M. Currie, A. D. Semenov, G. N. Gol'tsman, and R. Sobolewsk. **Picosecond hot-electron energy relaxation in NbN superconducting photodetectors.** *Appl. Phys. Lett.*, 76, 2000.

- [37] S. Cherednichenko, P. Khosropanah, E. Kollberg, M. Kroug, and H. Merkel. **Terahertz superconducting hot-electron bolometer mixers.** *Physica C: Superconductivity*, 372-376(1):407–415, 2002.
- [38] Jun Nagamatsu, Norimasa Nakagawa, Takahiro Muranaka, Yuji Zenitani, and Jun Akimitsu. **Superconductivity at 39 K in magnesium diboride.** *Nature*, 410:63–64, 2001.
- [39] N. Perrin and C. Vanneste. **Response of superconducting films to a periodic optical irradiation.** *Phys. Rev. B*, 28:5150–5159, 1983.
- [40] B.S. Karasik and A.I. Elantiev. **Noise temperature limit of a superconducting hot-electron bolometer mixer.** *Applied Physics Letters*, 68, 6:853, 1996.
- [41] Wei Miao, Yan Delorme, Alexandre Feret, Rolland Lefevre, Benoit Lecomte, Fred Dauplay, Jean-Michel Krieg, Gerard Beaudin, Wen Zhang, Yuan Ren, and Sheng-Cai Shi. **Comparison between hot spot modeling and measurement of a superconducting hot electron bolometer mixer at submillimeter wavelengths.** *Applied Physics Letters*, 106, 2009.
- [42] N. W. Ashcroft and N. D. Mermin. **Solid State Physics.** *College Edition, Harcourt College Publications*, 1976.
- [43] D. Wilms Floet, E. Miedema, T. M. Klapwijk, and J. R. Gao. **Hotspot mixing: A framework for heterodyne mixing in superconducting hot-electron bolometers**, volume 74. 1999.
- [44] H. Merkel, P. Khosropanah, P. Yagoubov, and E. Kollberg. **A hot spot mixer model for superconducting phononcooled HEB far above the quasiparticle bandgap**, volume 10th. 1999.
- [45] R. Barends, M. Hajenius, J.R. Gao, and T.M. Klapwijk. **Direct correspondence between HEB current-voltage characteristics and the current-dependent resistive transition.** *Proceedings of the 16th International Symposium on Space Terahertz Technology*, pages 416–419, 2005.
- [46] E.M. Gershenzon, G.N. Gol'tsman, A. I. Elant'ev, B. S. Karasik, and S. E. Potoskuev. *Soy. J. Low Temp. Phys.*, 14:414, 1988.

- [47] D. J. Hayton, J. R. Gao, J. W. Kooi, Y. Ren, W. Zha, and G. de Lange. **Stabilized hot electron bolometer heterodyne receiver at 2.5 THz.** *Applied Physics Letters*, 100, 2012.
- [48] H.B. Callen and T.A. Welton. **Irreversibility and generalized noise.** *Phys. Rev.*, 83:34–40, 1951.
- [49] A.R. Kerr, P.H. Siegel, and R.J. Matlack. **A Simple Quasi-Optical Mixer for 100-120 GHz.** *Microwave Symposium Digest, 1977 IEEE MTT-S International*, 1977.
- [50] J. Zmuidzinas and H.G. LeDucs. **Quasi-optical slot antenna SIS mixers.** *IEEE Transactions on Microwave Theory and Techniques*, 40:1797 – 1804, 1992.
- [51] J. L. Kloosterman et al. **Hot electron bolometer heterodyne receiver with a 4.7-THz quantum cascade laser as a local oscillator.** *Applied Physics Letters*, 102, 2013.
- [52] W. Zhang, W. Miao, J. Q. Zhong, S. C. Shi, D. J. Hayton, N. Vercruyssen, J. R. Gao, and G. N. Goltsman. **Temperature dependence of the receiver noise temperature and IF bandwidth of superconducting hot electron bolometer mixers.** *Superconductor Science and Technology*, 28, 2014.
- [53] E. Novoselov and S. Cherednichenko. **Low noise terahertz MgB<sub>2</sub> hot-electron bolometer mixers with an 11 GHz bandwidth.** *Applied Physics Letters*, 110, 2017.
- [54] P. Putz, K. Jacobs, M. Justen, F. Schomaker, M. Schultz, S. Wulff, and C. E. Honingh. **NbTiN Hot Electron Bolometer Waveguide Mixers on Si<sub>3</sub>N<sub>4</sub> Membranes at THz Frequencies.** *IEEE Transactions on Applied Superconductivity*, 21:636, 2011.
- [55] T. de Graauw et al. **The Herschel-Heterodyne Instrument for the Far-Infrared (HIFI).** *Astronomy & Astrophysics*, 518, L6:1–7, Jul. 2010.
- [56] **CST Computer simulation technology MICROWAVE STUDIO®.** <https://www.cst.com/>. Darmstadt, Germany.
- [57] L. R. Zink, K. M. Evenson, F. Matsushima, T. Nelis, and D. R. Smith. **Atomic oxygen fine-structure splittings with tunable far-infrared spectroscopy.** *Astrophysical Journal*, 371, L85, 1991.
- [58] P. Puetz, C. E. Honingh, K. Jacobs, M. Justen, M. Schultz, and J. Stutzki. **Terahertz hot electron bolometer waveguide mixers for GREAT.** *Astronomy & Astrophysics*, 542, 2012.

- [59] P. Putz, K. Jacobs, M. Justen, F. Schomaker, M. Schultz, S. Wulff, and C. E. Honingh. **NbTiN Hot Electron Bolometer Waveguide Mixers on Si<sub>3</sub>N<sub>4</sub> Membranes at THz Frequencies.** *IEEE Transactions on Applied Superconductivity*, 21:636, 2011.
- [60] P.H. Bolivar, M. Brucherseifer, J.G. Rivas, R. Gonzalo, I. Ederra, A.L. Reynolds, M. Holker, and P. de Maagt. **Measurement of the Dielectric Constant and Loss Tangent of High Dielectric-Constant Materials at Terahertz Frequencies.** *IEEE Transactions on Microwave Theory and Techniques*, 51, 2003.
- [61] D. Büchel, P. Pütz, K. Jacobs, C. E. Honingh, M. Schultz, and J. Stutzk. **HEB Waveguide Mixers up to 4.7 THz for the upGREAT FPA Receiver on SOFIA.** *Poster for the 24th International Symposium on Space Terahertz Technology 2013, Groningen Netherlands*, 2013.
- [62] S. Cherednichenko et al. **Local oscillator power requirement and saturation effects in NbN HEB mixers.** *12th ISSTT Proceedings*, pages 273–285, 2001.
- [63] **KERN Evo.** <http://www.kern-microtechnic.com/>. Eschenlohe, Germany.
- [64] C. Granet, G.L. James, R. Bolton, and G. Moorey. **A smooth-walled spline-profile horn as an alternative to the corrugated horn for wide band millimeter-wave applications.** *IEEE Trans. Antennas Propag.*, 54:848–854.
- [65] **Radiometer Physics GmbH.** <http://www.radiometer-physics.de/>. Meckenheim, Germany.
- [66] Paul F. Goldsmith. *Quasioptical Systems: Gaussian Beam Quasioptical Propagation and Applications*. 1998.
- [67] Guozhen Liang, Tao Liu, and Qi Jie Wang. **Recent Developments of Terahertz Quantum Cascade Lasers.** *IEEE Journal of Selected Topics in Quantum Electronics*, 23.
- [68] **Virginia Diodes, Inc.** <http://vadiodes.com/>. Charlottesville, VA, USA.
- [69] **QMC Instruments Ltd.** <http://www.terahertz.co.uk/>. Cardiff, UK.
- [70] S. Weinreb, T. Gaier, J.E. Fernandez, N. Erickson, and J. Wielgus. **Cryogenic low noise amplifiers.** *GaAs Applications Symp. Dig.*, pages 216–220, 2000.
- [71] **Mini-Circuits®.** [www.minicircuits.com/](http://www.minicircuits.com/). USA.

- [72] B. Klein, S. Hochgürtel, I. Krämer, A. Bell, K. Meyer, and R. Güsten. **High-resolution wide-band Fast Fourier Transform spectrometers.** *Astronomy & Astrophysics*, 542, 2012.
- [73] Michael Brandt. **Superconducting Hot Electron Bolometers on Silicon Nitride Membranes for Terahertz Waveguide Mixers.** *Dissertation*, 2004.
- [74] **Bruker Corporation.** <https://www.cst.com/>. Billerica, USA.
- [75] Yihong Yang, Alisha Shutler, and D. Grischkowsky. **Measurement of the transmission of the atmosphere from 0.2 to 2 THz.** *Optical Society of America*, 19(9):8838, 2011.
- [76] S. Svechnikov, A. Verevkin, B. Voronov, E. Menschikov, E. Gershenson, and G. Gol'tsman. **Quasioptical phonon-cooled NbN hot-electron bolometer mixer at 0.5-1.1 THz.** *Proc. 9th Int. Symp. Space THz Techn.*, pages 45–51, 1998.
- [77] P. Khosropanaha, J. R. Gao, W. M. Laauwen, and M. Hajenius. **Low noise NbN hot electron bolometer mixer at 4.3THz.** *Applied Physics Letters*, 91.
- [78] J. J. A. Baselmans, A. Baryshev, S. F. Reker, M. Hajenius, J. R. Gao, T. M. Klapwijk, Yu. Vachtomin, S. Maslennikov, S. Antipov, B. Voronov, and G. Gol'tsman. **Direct detection effect in small volume hot electron bolometer mixers.** *Applied Physics Letters*, 86:163503, 2005.
- [79] S. Svechnikov, A. Verevkin, B. Voronov, E. Menschikov, E. Gershenson, and G. Gol'tsman. **Direct detection effect in small volume hot electron bolometer mixers.** *Proceedings of the 9th International Symposium on Space THz Technology*, page 44, 1998.
- [80] B. Klein, I. Krämer, S. Hochgürtel, R. Güsten, A. Bell, K. Meyer, and V. Chetk. **Array Fast Fourier Transform Spectrometer (AFFTS).** *RadioNet Engineering Forum Workshop*.
- [81] M. Shcherbatenko, I. Tretyakov, Yu. Lobanov, S. N. Maslennikov, N. Kaurova, M. Finkel, B. Voronov, G. Goltsman, and T. M. Klapwijk. **Nonequilibrium interpretation of DC properties of NbN superconducting hot electron bolometers.** *Applied Physics Letters*, 109(13):132602, 2016.
- [82] M. Justen, T. Dana K. Otani, F. Castellano, U.U. Graf, and J. Faist. **Waveguide embedding of a double metal 1.9THz QCL into a split block with diagonal horn**

**antenna.** *Proceedings of the 26th International Symposium on Space Terahertz Technology 2015, Cambridge USA, 2015.*

- [83] W. Miao, W. Zhang, K. M. Zhou, H. Gao, K. Zhang, W. Y. Duan, Q. J. Yao, S. C. Shi, Y. Delorme, and R. Lefevre. **Investigation of the Performance of NbN Superconducting HEB Mixers of Different Critical Temperatures.** *IEEE Transactions on Applied Superconductivity*, 27(4), 2017.
- [84] F. Boussaha, J. H. Kawamura, J. Stern, and C. Jung-Kubiak. **2.7 THz Balanced Waveguide HEB Mixer.** *IEEE Trans. THz Sci. Technol.*, 4:545–551.
- [85] Ling Jiang, Shoichi Shiba, Ken Shimbo, Nami Sakai, Tetsuya Yamakura, Mika Sugimura, P. G. Ananthasubramanian, Hiroyuki Maezawa, Yoshihisa Irimajiri, and Satoshi Yamamoto. **Development of THz Waveguide NbTiN HEB Mixers.** *IEEE Trans. on applied superc.*, 19, 2009.
- [86] D. Büchel, P. Pütz, K. Jacobs, M. Schultz, C. Risacher, H. Richter, O. Ricken, H.-W. Hübers, R. Güsten, J. Stutzki, and C. E. Honingh. **Performance of a 4.7 THz Waveguide HEB Mixer for SOFIA’s upGREAT.** *25th International Symposium on Space Terahertz Technology 2014, Moscow Russia, 2014.*
- [87] A. Wagner-Gentner, U.U. Graf, D. Rabanus, and K. Jacobs. **Low loss THz window.** *Infrared Physics & Technology*, 48:249–253, 2006.
- [88] Christoph Risacher. **Privat communication.**
- [89] D. Büchel, M. Justen, K. Jacobs, P. Pütz, M. Schultz, K. Otani, U . U. Graf, C. E. Honingh, and J. Stutzk. **A HEB Waveguide Mixer Operating with a Waveguide QCL at 1.9 THz.** *27th International Symposium on Space Terahertz Technology 2016, Nanjing China, 2016.*
- [90] G.R. Boogaard, A.H. Verbruggen, W. Belzig, and T.M. Klapwijk. **Resistance of superconducting nanowires connected to normal-metal leads.** *Phys. Revi.*, B69:220503, 2004.
- [91] N. Vercruyssen, T.G.A. Verhagen, M.G. Flokstra, J.P. Pekola, and T.M. Klapwijk. **Evanescence states and nonequilibrium in driven superconducting nanowires.** *Phys. Revi.*, B85:224503, 2012.

- [92] P. Pütz, M. Brasse, J. R. Gao, K. Jacobs, M. Justen, P. Khosropanah, W. Miao, M. Schultz, S. C. Shi, W. Zhang, and C. E. Honingh. **High Sensitivity Waveguide HEB Mixers at 2.5 THz**. *22nd International Symposium on Space Terahertz Technology, Tucson*, 2011.
- [93] S. Shiba and K. Shimbo and L. Jiang and N. Sakai and M. Sugimura, P. G. Ananthasubramanian, H. Maezawa, and S. Yamamoto. **Temperature Dependence of HEB Mixer Performance**. *19th ISSTT Proceedings*, pages 59–61, 2008.
- [94] H. Bartolf, A. Engel, A. Schilling, M. Siegel K. Il'in, H.-W. Hübers, and A. Semenov. **Current-assisted thermally activated flux liberation in ultrathin nanopatterned NbN superconducting meander structures**. *Phys. Rev. B*, 81(024502), 2010.
- [95] A. Einstein. **Investigations on the theory of the brownian movement**. *Ann. d. Phys.*, 17:549, 1905.
- [96] Sascha Krause. **NbN ultra-thin films for HEB-based THz systems**. *Master Thesis*, 2013.
- [97] V.V.Smidt. *Introduction to Superconductivity*. 1982.
- [98] P. Pütz, K. Jacobs, M. Schultz, S. Fathi, M. Justen, C. E. Honingh, and J. Stutzki. **4.7 THz flight mixers for upGREAT**. *28th ISSTT Proceedings*, 2017.
- [99] D. Büchel, K. Jacobs, P. Pütz, M. Schultz, C. E. Honingh, and J. Stutzki. **Performance of NbN and NbTiN HEB waveguide mixers for GREAT and upGREAT**. *28th International Symposium on Space Terahertz Technology 2017, Cologne Germany*, 2017.
- [100] P. P. Munoz, S. Bedorf, M. Brandt, T. Tils, N. Honingh, and K. Jacobs. **THz Waveguide Mixers With NbTiN HEBs on Silicon Nitride Membranes**. *IEEE Microw. Wireless Comp. Lett.*, 16, 2006.
- [101] Marc Peter Westig, Justen Matthias, Karl Jacobs, Jürgen Stutzki, Michael Schultz, Florian Schomacker, and Netty Honingh. **A 490 GHz planar circuit balanced Nb-Al<sub>2</sub>O<sub>3</sub>-Nb quasiparticle mixer for radio astronomy: Application to quantitative local oscillator noise determination**. *Journal of Applied Physics*, 112:249–253, 2012.
- [102] S. Fathi, K. Jacobs, M. Schultz, P. Pütz, S. Selig, and C. E. Honingh. **1.9 THz balanced superconducting Hot Electron Bolometer mixer fully integrated on chip**.

*28th International Symposium on Space Terahertz Technology 2017, Cologne Germany, 2017.*

- [103] S. Krause, V. Mityashkin, S. Antipov, G. Gol'tsman, D. Meledin, V. Desmaris, V. Belitsky, and M. Rudzinsk. **Reduction of phonon escape time for NbN hot electron bolometers by using GaN buffer-layers.** *IEEE Transactions on Microwave Theory and Techniques*, SPECIAL ISSUE, 2016.
- [104] S. Antipov, A. Trifonov, S. Krause, D. Meledin, V. Desmaris, V. Belitsky, M. Rudzinski, and G. Gol'tsman. **IF bandwidth of NbN HEB mixers on GaN buffer layer at 2 THz local oscillator frequency.** *28th International Symposium on Space Terahertz Technology 2017, Cologne Germany, 2017.*
- [105] Ronan D. Higgins and Jacob W. Kooi. **Electrical standing waves in the HIFI HEB mixer amplifier chain.** *Proc. of SPIE Vol. 7215*, 2010.
- [106] J. W. Kooi, J. J. A. Baselmans, J.R. Gao, T. M. Klapwijk, M. Hajenius, P. Dieleman, A. Baryshev, and G. de Lange. **Superconducting hot-electron bolometer: from the discovery of hot-electron phenomena to practical applications.** *Journal of Applied Physics*, 101, 2007.



## Danksagung

Als erstes möchte ich Herrn Prof. Dr. Jürgen Stutzki danken, der es mir ermöglicht hat meine Dissertation am I. Physikalischen Institut durchzuführen. Ich hatte dadurch die besondere Gelegenheit an den spannenden Projekten GREAT und upGREAT für SOFIA teilzunehmen.

Weiterhin danke ich Herrn Prof. Dr. Andreas Zilges für die Übernahme des Zweitgutachtens und Herrn Prof. Dr. Sebastian Diehl für die Übernahme des Prüfungsvorsitzes.

Ein besonderer Dank gilt auch Dr. Netty Honingh, die mich während meiner Dissertation betreut hat. Sie hat mir tägliche mit Ihrem umfangreichen Wissen bei experimentellen und theoretischen Problemen geholfen.

Danke auch an Dr. Karl Jacobs, der mich als zweiter Betreuer unterstützt hat. Er hat es durch seine Erfahrung im Mircostrukturlabor ermöglicht die Mischer zu fertigen.

Ich danke Dr. Patrick Pütz, der ebenfalls ein signifikanten Anteil am der Fertigung der Mischer im Mircostrukturlabor hatte.

Ich danke Sina Fathi für seine Hilfe im Labor und konstruktive Gespräche.

Ich danke Florian Blauth, der mir unter anderem bei der Softwareentwicklung für meinen Messaufbau und bei Problem am Messaufbau geholfen hat.

Ich danke Sina Widdig für ihre Gespräche über das Leben abseits der Universität.

Ich danke Michael Schulz für seine Geduld beim Montieren der Mischer und für die Hilfe bei der Anfertigung von Konstruktionszeichnungen für verschieden Bauteile des Messaufbaus. Sein besonderer Sinn für Übersicht und Ordnung hat mir immer wieder geholfen.

Ich danke Stefan Wulf, der mir beim Arbeiten im Mircostrukturlabor geholfen hat.

Ich danke Mathias Justen für die gemeinsame Arbeit und die Bereitstellung der QCL LOs.

Ich danke auch allen weiteren Kollegen aus der Superconducting Detector Gruppe mit denen ich im Laufe der Zeit zusammen gearbeitet habe.

Außerdem möchte ich der Feinmechaniker Werkstatt danken, die es durch ihre hohe präzise Arbeit unter andrem ermöglicht hat, alle Mischer Blöcke inclusive der Hornklammer für alle Mischer nahezu gleichwertig herzustellen.

Mein Dank gilt auch der Elektronikwerkstatt, welche mit bei Bau der IF-box geholfen hat.

Ich danke dem ganzen upGREAT Team, besonders Christopf Risacher für die gute zusammen Arbeit und Rolf Güsten, der uns den 1.9 THz GREAT backup LO zu Verfügung gestellt hat. Nur mit Hilfe dieses LO war es möglich die meisten LFA Mischer zu vermessen.

Einen Besondern Dank gilt meiner Familie, die mich während meines Studiums unter-

stützt, aufgemunterte und abgelenkt hat.

Im letzten Abschnitt möchte ich Anna danken, die mir vor allem gegen Ende meiner Arbeit immer wieder gezeigt hat was im Leben wichtig ist. Ich liebe dich.

## **Financial Support**

This work was supported within the Collaborative Research Council 956 (SFB 956), sub-projects D3, funded by the Deutsche Forschungsgemeinschaft (DFG).

In Addition this work was supported by the Federal Ministry of Economics and Technology via the German Space Agency (DLR), grant 50 OK 1103.



## Teilpublikationen

- *Denis Büchel, Patrick Pütz, Karl Jacobs, Michael Schultz, Urs U. Graf, Christophe Risacher, Heiko Richter, Oliver Ricken, Heinz-Wilhelm Hübers, Rolf Güsten, Cornelia E. Honingh, Jürgen Stutzki, "4.7 THz superconducting hot-electron bolometer waveguide mixer"*, IEEE Transactions on Terahertz Science and Technology, volume. 5, no. 2, pp. 207-214, 2015
- *C. Risacher, R. Guesten, J. Stutzki, H.-W. Huebers, A. Bell, C. Buchbender, D. Buechel, T. Csengeri, U. U. Graf, S. Heyminck, R. D. Higgins, C. E. Honingh, K. Jacobs, B. Klein, Y. Okada, A. Parikka, P. Puetz, N. Reyes, O. Ricken, D. Riquelme, R. Simon, H. Wiesemeyer, "The upGREAT 1.9 THz multi-pixel high resolution spectrometer for the SOFIA Observatory"*, Astronomy & Astrophysics, volume 595, A34, 2016
- *Christophe Risacher; Rolf Güsten; Jürgen Stutzki; Heinz-Wilhelm Hübers; Denis Büchel; Urs U. Graf; Stefan Heyminck; Cornelia E. Honingh; Karl Jacobs; Bernd Klein; Thomas Klein; Christian Leinz; Patrick Pütz; Nicolas Reyes; Oliver Ricken; Hans-Joachim Wunsch; Paul Fusco; Stefan Rosner, "First Supra-THz Heterodyne Array Receivers for Astronomy With the SOFIA Observatory"*, IEEE Transactions on Terahertz Science and Technology, volume: 6, issue: 2, 2016

## Konferenz Beiträge

- *D. Büchel, P. Pütz, C.E. Honingh, K. Jacobs, M. Schultz, and J. Stutzki, "Development of superconducting hot electron bolometer mixers for (up)GREAT on SOFIA"*, Kryoelektronische Bauelemente 2012, Karlsruhe, Germany, 2012
- *D. Büchel, P. Pütz, M. Schultz, J. Stutzki, K. Jacobs and C. E. Honingh, "HEB Waveguide Mixers up to 4.7 THz for the upGREAT FPA Receiver on SOFIA"*, Proceedings of the 26th International Symposium on Space Terahertz Technology 2013, Groningen, Netherlands, 2013
- *P. Pütz, K. Jacobs, D. Büchel, M. Schultz, C. Risacher, H. Richter, O. Ricken, H.-W. Hübers, R. Güsten, J. Stutzki, and C. E. Honingh, "Performance of a 4.7 THz Waveguide HEB Mixer for SOFIA's upGREAT"*, Proceedings of the 25th International Symposium on Space Terahertz Technology 2014, Moskow, Russia, 2014
- *P. Pütz, D. Büchel, K. Jacobs, M. Schultz and C.E. Honingh, "1.9 THz Waveguide HEB Mixers for the upGREAT Low Frequency Array"*, Proceedings of the 26th

International Symposium on Space Terahertz Technology 2015, Cambridge, Massachusetts, U.S.A., 2015

- *D. Büchel, M. Justen, K. Jacobs, P. Pütz, M. Schulz, J. Stutzki, and C.E. Honingh, **Study of a Waveguide HEB Mixer Operated with a Waveguide QCL at 1.9 THz***", Proceedings of the 27th International Symposium on Space Terahertz Technology 2016, Nanjing, China, 2016
- *D. Büchel, K. Jacobs, P. Pütz, M. Schultz, C. E. Honingh, and J. Stutzki, **"Performance of NbN and NbTiN HEB waveguide mixers for GREAT and upGREAT"***, Proceedings of the 28th International Symposium on Space Terahertz Technology 2017, Köln, Germany, 2017

## **Eidesamtlich Erklärung**

Ich versichere, dass ich die von mir vorgelegte Dissertation selbständig angefertigt, die benutzten Quellen und Hilfsmittel vollständig angegeben und die Stellen der Arbeit einschließlich Tabellen, Karten und Abbildungen, die anderen Werken im Wortlaut oder dem Sinn nach entnommen sind, in jedem Einzelfall als Entlehnung kenntlich gemacht habe; dass diese Dissertation noch keiner anderen Fakultät oder Universität zur Prüfung vorgelegen hat; dass sie abgesehen von unten angegebenen Teilpublikationen noch nicht veröffentlicht worden ist, sowie, dass ich eine solche Veröffentlichung vor Abschluss des Promotionsverfahrens nicht vornehmen werde. Die Bestimmungen der Promotionsordnung sind mir bekannt. Die von mir vorgelegte Dissertation ist von Prof. Dr. Jürgen Stutzki betreut worden.

Köln, den 28.07.2017



# Lebenslauf

Denis Büchel  
Berrenrather Str. 409  
50937 Köln

Geburtstag: 27.11.1985  
Geburtsort: Köln  
Staatsangehörigkeit: Deutsch  
Familienstand: ledig

## Schulbildung:

---

1992 bis 1996	Gemeinschaftsgrundschule Manderscheider Platz Köln
1996 bis 2005 Juni 2005	Europaschule Köln Gesamtschule Zollstock Abitur

## Freiwilliges Soziales Jahr:

---

Juni 2005 bis Juni 2006	Hausnotrufzentrale beim Arbeiter Samariter Bund Köln
-------------------------	---

## Studium:

---

2006 bis 2009	Bachelor in Physik an der Universität zu Köln
Aug. 2009	Bachelorarbeit zum Thema: Bau einer Kalibrationseinheit für das NANTEN 2 Teleskop am I. Physikalischen Institut der Universität zu Köln
2009 bis 2012 Jan. 2012	Master in Physik an der Universität zu Köln Masterarbeit zum Thema: Analysis of absorption lines along the line-of-sight towards Sagittarius B2(M) am I. Physikalischen Institut der Universität zu Köln

## Promotion:

---

April 2012	Beginn des Promotionsstudiums in Experimental Physik am I. Physikalischen Institut der Universität zu Köln
------------	--

Anstellungsverhältnis:

Juli 2006 bis Nov. 2010	Aushilfskraft Mitarbeiter Zentrale beim Arbeiter Samariter Bund Köln
Feb. 2010 bis Apr. 2010	Studentische Hilfskarft am I. Physikalischen Institut der Universität zu Köln
Sep. 2010 bis Okt. 2011	Studentische Hilfskarftam I. Physikalischen Institut der Universität zu Köln
Apr. 2012 bis Jul. 2017	Wissenschaftlicher Mitarbeiter am I. Physikalischen Institut der Universität zu Köln